ADVANCES IN ELECTROMETALLURGY

No. 1 Volume 12 2014

Modelling the structural and stress–train state of a dissimilar steel ingot in electroslag melting

V.I. Makhnenko, A.S. Milenin, S.S. Kozlitina and L.I. Dzyubak

E.O. Paton Electric Welding Institute, Kiev

It is shown that the application of dissimilar structures, components of machines and mechanisms in various branches (power complex, pipeline transport, aerospace industry) allows producing the unique complex of service properties which are difficult to provide when using similar materials. In this case the natural difficulties are encountered in producing the dissimilar parts and billets with a guaranteed quality of metal. To manufacture the dissimilar components, there are different technological procedures, one of which is electroslag melting in a current-carrying mould with a molten filler metal, in particular for producing of large-diameter steel ingots dissimilar in the direction of height, used for turbine rotor shafts. One of the problems of optimizing the technological parameters of this process is the minimizing of the tendency of dissimilar ingot metal to the initiation of cold cracks. A set of mathematical models and programming means for the numerical analysis of the kinetics of thermal, physical-chemical and mechanical processes was developed, owing to which some peculiarities of the formation of transition zone of the dissimilar ingots were revealed. An approach was suggested for selection of the optimum chemical composition of filler metal and, thus, the feasibility of minimizing the ingot metal susceptibility to the formation of cold cracks in transition zone was demonstrated. The significant influence of material with the chemical composition, different from the optimum one, on the susceptibility of ingot metal to cracking was also shown and methods of effective optimizing the process of electroslag melting of ingots of different height, were described for reducing the risk of initiation of these types of defects. Ref. 13., Table 1, Figures 2.

The application of dissimilar elements in structures and mechanisms is one of the efficient methods of obtaining the unique set of their service characteristics (higher strength, resistance to the effect of corrosive media and high temperatures, resistance to different types of loading, etc [1–3]). In this case, it is necessary to produce permanent joints in elements from different materials and this requires the optimisation of the metal of the dissimilar transition zone from the viewpoint of the specific level of the service properties of the structure as a whole [4]. An example of the structural components are the turbine axis dissimilar along the length and used in the power engineering. They are produced by electroslag welding of cylindrical components with a large diameter produced from different steels. This is a difficult and energy consuming process. An alternative is the process of electroslag melting (ESM) of blanks with the change of the composition of remelted metal during melting of the ingot.

The E.O. Paton Electric Welding Institute has developed the technology of electroslag melting in a current-conducting solidification mould with liquid filler metal [5] for producing large diameter ingots, including the ingot with the variable chemical composition along the height (Fig. 1). One of the tasks of the optimisation of this process is the reduction of the susceptibility of the metal of the transition zone to the formation of discontinuities such as cold cracks (CC).
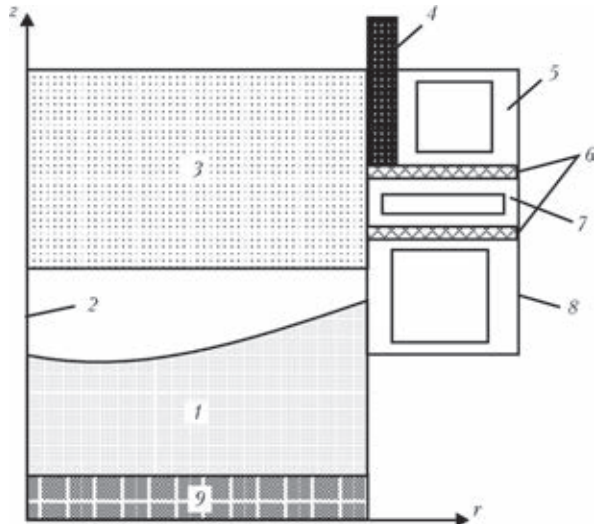
V.I. Makhnenko, A.S. Milenin, S.S. Kozlitina and L.I. Dzyubak

Fig. 1. Diagram of the electroslag melting of an ingot with a large diameter dissimilar in the direction of height: *1*) the ingot; *2*) the liquid metal pool; *3*) the slag; *4*) the graphite lining; *5*) the current-conducting solidification mould; *6*) insulator; *7*) the solidification mould shunting the slag pool; *8*) the solidification mould; *9*) the baseplate.

The necessary condition for the formation of the CC is the simultaneous presence in a specific region of the metal of tensile stresses, quenched structures and diffusible hydrogen [6, 7].

One of the methods of ensuring the high quality of the ingots melted by electroslag melting (together with a reduction of the volume fraction of hydrogen in the remelted metal) is the optimisation of the production processes in terms of minimising the amount of martensite phases in the region of high tensile stresses. It is rational to evaluate the susceptibility of the metal of the ingot to the formation of these defects in different melting conditions using advanced methods of mathematical and computer modelling of the kinetics of temperature, phase and stress-strain state of the metal of the ingot.

In this work, numerical analysis of the kinetics of the structural and stress–strain state of a dissimilar steel ingot depending on its chemical composition, and evaluation of the susceptibility of the metal to go to cracking in electroslag remelting, was carried out to develop mathematical models and means of computer modelling.

As shown in [8], the optimum regime for minimising the transition region between the dissimilar parts of the ingot and also for producing a shallow liquid metal pool homogeneous in the radial direction of the cylindrical ingot is the regime consisting of the following consecutive stages: melting the first part of the ingot with the composition X_I; reduction of the dimensions of the liquid pool with interaction of the withdrawal of the ingot (displacement rate of the baseplate $v = 0$) and variation of the supplied power w_0; formation of the transition zone as a result of adding the metal with the composition X_{III}; melting of the second part of the ingot with the composition X_{II}.

The kinetics of the phase composition of the metal of the ingot in the process of electroslag melting up to complete cooling is predicted taking into account the results of numerical analysis of the temperature cycles in specific melting conditions, the chemical composition of the steels of the ingot and also the diagram of continuous cooling transformation of austenite. Taking into account the holding time above the appropriate temperatures, these diagrams were constructed for many steels [9, 10]. The continuous cooling transformation diagrams can be used for evaluating the mass part V_n of a specific *n*-th structural component (n = A, F, P, B, M – respectively austenitic, ferritic, pearlitic, bainitic, martensitic) in the regions of both pure and mixed phases: austenitic (A), austenitic–ferritic (A + Ca), pearlitic (A + F + Ca) where Ca are the carbides, bainitic (A + F + Ca) adjacent to the zone restricted by the temperature of the start of martensitic transformation and above by the temperatures lower than 600 °C. The points of intersection of the curves of the temperature cycles $T(t)$ are characterised by the mean cooling rate in the zone 800...500 °C $W_{8/5}$, determine the temperatures of the start and end of the corresponding structural transformations of austenite to the *n*-th phase. The simplest methods of using the austenite continuous cooling transformation diagram for a specific cooling cycle with the value

$[W_{8/5}]$ is the interpolation of the data of the diagram of the appropriate steel to the specific range, i.e., the required value A_K at $[W_{8/5}]$ ($W^+_{8/5} > [W_{8/5}] > W^-_{8/5}$) is determined from the following relationship:

$$A_K = \frac{A^+_K - A^-_K}{W^+_{8/5} - W^-_{8/5}}(W^+_{8/5} - [W_{8/5}]) + A^-_K$$

where A^+_K corresponds to $W^+_{8/5}$; $A^-_K - W^-_{8/5}$.

Thus, for any cooling curve $\frac{\partial T}{\partial t} < 0$ in the metal of the investigated ingot the appropriate continuous cooling transformation diagram is used to determine the required data for the temperatures of the start and end of the n-th phase of transformation of austenite, the duration of transformation to the phase n = F, B, B, M, the mass fractions of the start and end of the n-th transformation V^{st}_n, V^e_n.

Correspondingly, at the temperature $T(t)$ at the moment of time t at $T^{st}_n > T(t) > T^e_n$ the relative mass fraction of the n-th microstructure $V_n(t, T)$ is determined as follows:

$$V_n(t, T) = \frac{V^e_n}{2}\left[\frac{T^{st}_n - T(t)}{T^{st}_n - T^e_n} + \frac{t^{st}_n - t}{t^{st}_n - t^e_n}\right] + V^{st}_n$$

In the case in which $\frac{\partial T}{\partial t} > 0$ we accept the condition

$$\frac{\partial V_n}{\partial t} = 0 \text{ at } T < 800 \text{ °C};$$

$$V_{n \neq A} \equiv 0, V_A = 1.0 \text{ at } T \geq 800 \text{ °C}.$$

If the diagram of the continuous cooling transformation of the austenite of the specific steel does not contain detailed data on the microstructural state for the required cooling cycle, they can be restored using the appropriate theoretical hypotheses. In particular, a relatively popular hypothesis is the Avrami hypothesis [11] used the welding literature according to which the rate of formation of new phases $\left.\frac{\partial V}{\partial t}\right|_{n \neq A}$ at the given temperature $T(t)$ is proportional to the retained austenite content $V_A(t)$, i.e.

$$\frac{\partial V_{n \neq A}}{\partial t} = -\frac{\partial V_A(t)}{\partial t} = k(T)V_A(t) \qquad (1)$$

where $k(T)$ is the function of temperature.

Equation (1) shows that in the temperature range $\Delta T = T_2 - T_1$

$$\Delta V(t) = C_0 \exp[-k(T)(t - t_0)]$$

where the integration constant C_0 is determined at temperature T_1 and time $t = t_0$: $C_0 = V_A(t_0)$.

Analysis of the stress–strain state of the ingot in the process of electroslag remelting in this study was carried out on the basis of the numerical solution of the problem of non-stationary thermoplasticity by determining the elastic plastic strains from the moment of the start of melting up to the complete cooling of the ingot [12]. The relationship between the increments of the components of the stress tensors $\Delta\sigma_{ij}$ and strains $\Delta\varepsilon_{ij}$ was determined by the Hooke's law and by the approximated law of plastic yielding on the basis of the following relationships [13]

$$\Delta\varepsilon_{ij} = \psi(\sigma_{ij} - \delta_{ij}/\sigma_m) + \delta_{ij}(K\sigma_m + \Delta\varepsilon_m)$$

$$-\frac{1}{2G}(\sigma_{ij} - \delta_{ij}\sigma_m)* + (K\sigma_m)*$$

where $K = \frac{1 - 2v}{E}$; $G = \frac{E}{2(1 + v)}$; E is the Young modulus; v is the Poisson coefficient; σ_m are the membrane stresses; δ_{ij} is the Kronecker symbol; ψ is the function of the state of the material, determined by the plastic yielding conditions according to the von Mises criterion.

$$\psi = \frac{1}{2G}, \text{ If } \sigma_i < \sigma_T$$

$$\psi > \frac{1}{2G}, \text{ if } \sigma_i = \sigma_T$$

where σ_i is the stress intensity; σ_T is the yield limit.

To take into account the influence of the volume effects of the phase transformations, it is necessary to determine the relative linear changes of the elementary volume in the pres-

V.I. Makhnenko, A.S. Milenin, S.S. Kozlitina and L.I. Dzyubak

ence of the appropriate diagram of continuous cooling transformation of austenite and the handbook data for the volume change of the appropriate microstructure $\gamma_n(T)$ according to the following dependences, cm^3/g:

$\gamma_A(T) = 0.12282 + 8.76 \cdot 10^{-6} (T + 273) + 2.13 \cdot 10^{-6} C$;

$\gamma_M(T = 0.12708 + 4.448 \cdot 10^{-6} (T + 273) + 2.79 \cdot 10^{-3} C$;

$\gamma_F(T) = \gamma_P(T) = \gamma_B(T) = 0.12708 + 5.528 \cdot 10^{-6} (T + 273)$,

where C is the carbon content, %.

Is assumed that the temperature and properties in each relatively small volume of the ingot are constant and also the mass is preserved. Consequently, the relative change of the linear dimensions of the elementary volume $\Delta\varphi$, associated with the variation of the temperature and microstructures in the time period $\Delta t = t_k - t_{k-1}$, at the known values of $\gamma_n(T)$ and $V_n(T, t)$ can be written in the following form

$$\Delta\varphi = \frac{\sum_{n=A,\ldots,M} V_n(T, t_k)\gamma_n(t_k) - \sum_{n=A,\ldots,M} V_n(T, t_{k-1})\gamma_n(T_{k-1})}{3\sum_{n=A,\ldots,M} V_n(T_0, 0)\gamma_n(T_0)}$$

where T_0 is the initial temperature of the formation of the material of the solid ingot (for example, the solidus temperature).

In most cases, the yield limit of the metal in relation to V_n is calculated using the dependence

$$\sigma_T(T) = \sum_{n=A,\ldots,M} \sigma_T^{(n)}(T) V_n(T)$$

where $\sigma_T^{(n)}$ is the yield limit of the n-th structural component in relation to temperature.

In this case, for many steels $\sigma_T^{(n)}(T)$ can be written in the form

$$\sigma_T^{(n)}(T) = \sigma_T^{(n)}(20\,°C) f(T)\ldots,$$

where $f(T)$ is independent of n.

The given models of the kinetics of the structural state and of the stress–strain state of the metal, dissimilar along the length of the ingot, are combined with the proposed models of the variation of tempera-ture fields in chemical composition in the framework of the generalised finite-difference and finite-element schemes. As an example of the numerical analysis of the metal dis-similar along the length of a large diameter ingot to the formation of cold cracks, we examine the process of electroslag melting of a cylindrical ingot with a diameter of 1200 mm produced from steels of different grades: steel SAE2330 (composition XI), wt.%: 0.3 C – 51 Mn – 0.32 Si – 0.007 – S – 0.011 P – 3.03 Ni – 0.07 Cr – 0.032 Al – 0.001; Ti; steel 28NiCrMo74 (composition XII), wt.%: 0.3 C – 0.46 Mn – 0.24 Si – 0.025 S – 0.03 P – 2.06 Ni – 1.44 Cr – 0.37 Mo – 0.2 Cu – 0.001 V.

The melting rate in the investigated case was equal to 6 mm/min, the temperature of cast metal 1550°C. Correspondingly, in the first 2.75 h (1000 mm of ingot along the height) the solidification mould is supplied by the melt with the composition X_I, the second half of the ingot should have the composition X_{II}. A 'smoother' dissimilar transition along the height can be obtained by diluting the previous composition of the liquid metal pool with the composition X_{III}. To calculate the optimum chemical composition of the addition X_{opt} we can use the formula:

$$X_{opt} = X_{II} + \frac{4G_F}{\pi D^2 \upsilon \tau}(X_{II} - X_I) \quad (2)$$

where G_f is the volume of the liquid metal pool of the end of melting the part of the ingot with the composition X_I.

In a general case if we know the chemical composition $X(t)$ of the liquid metal pool with the volume $G(t)$ at the moment of time t and the volume rate of introduction of the liquid metal $\pi\dfrac{D^2}{4}\upsilon(t)$ with the chemical composition X_{III}, the chemical composition of the liquid metal pool $X(t + \Delta t)$ in the time period Δt is determined by the relationship

$$X(t+\Delta t) = \frac{X(t)[2G(t) - G(t+\Delta t)] + X_{III}\dfrac{\pi D^2}{4}\upsilon(t)\Delta t}{2G(t) - G(t+\Delta t)] + \dfrac{\pi D^2}{4}\upsilon(t)\Delta t}$$
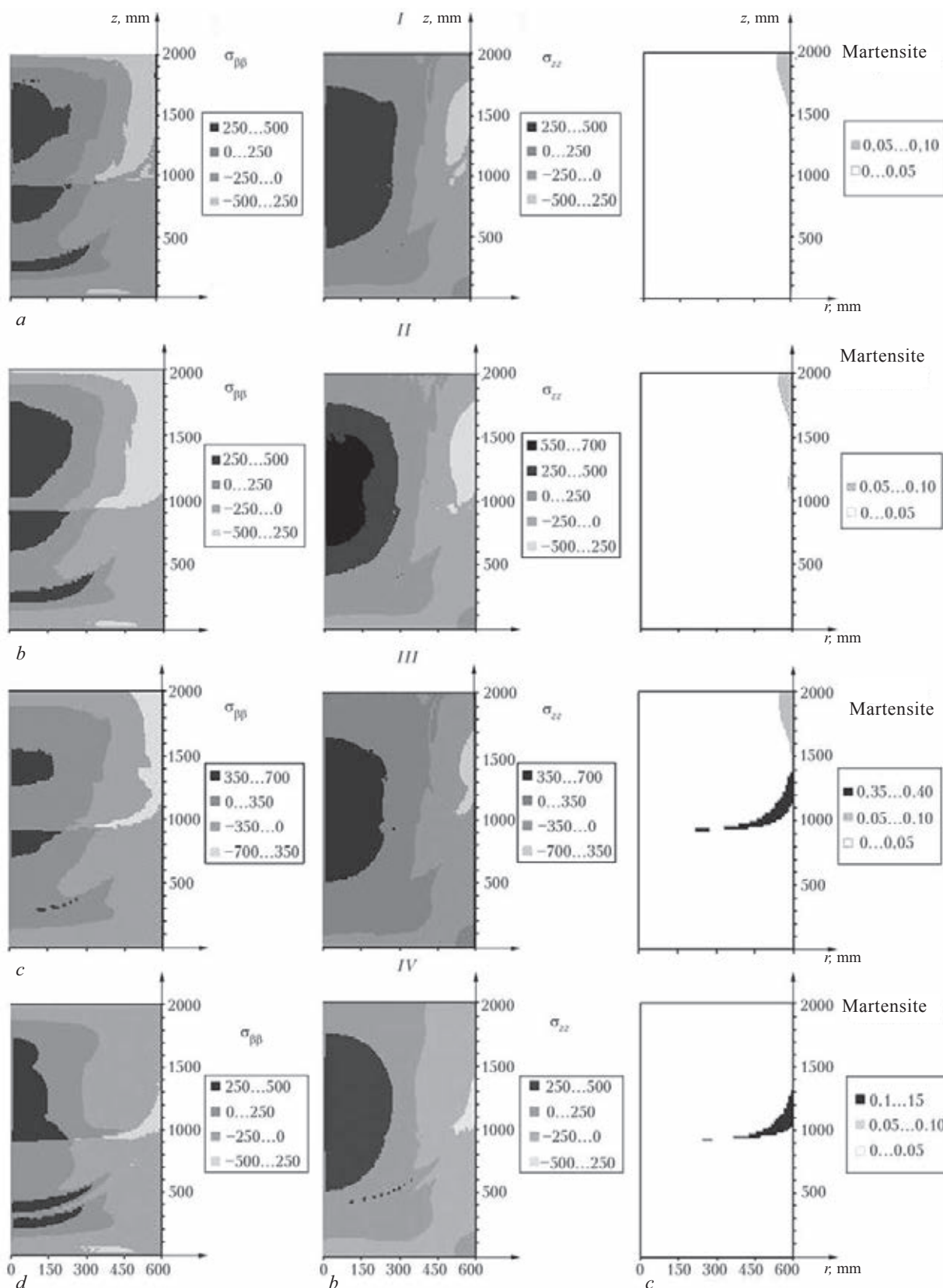
Fig. 2. Distribution of the tangential (*a*), axial (*b*) stresses and martensite (*c*) in the cross-section of a dissimilar cylindrical ingot of steels SAE2330 and 28NiCrMo74 with the filler metal of the optimum composition 30CAD6-12 (*I*); without it (*II*); with the filler metal 14NiCr1.4 (*III*); with the filler metal 30NCD12 after melting by electroslag melting (*IV*).

where $G(t)$ is the volume of the liquid metal pool; $v(t)$ is the melting rate; D is the ingot diameter.

It should be mentioned that in the optimisation of the investigated technological process it is important to select the intermediate metal. Since the selection of the chemical composition according to equation (2) for each specific pair of metals of the dissimilar ingot is time-consuming and the melting process is complicated, and it is convenient to add the existing steel grades whose composition is closest to the calculator composition. Table 1 gives the results of calculation of the composition of the liquid pool where the addition is are represented by the steel 30CAD6-12, wt.% (0.28% C – 0.49% Mn – 0.32% Si – 0.050% S – 0.012% P – 0.13% Ni – 1.65% Cr – 0.22% Mo – 1.050% Al).

In this case, in the transition zone there are no prerequisites regarding the susceptibility of the metal to cold cracking (Fig. 2, *I*). The processes of heat and mass transfer result in a smooth transition of the structural components from one composition of the ingot to another, with the highest probability of formation of defects recorded in the central part of the ingot. This is associated with the special features of removal of heat and shrinkage processes, whereas the formation of the dissimilar transition zone takes place in the conditions close to optimum.

It should be mentioned that the application of the multistage process of electroslag melt-

ing of the ingot dissimilar along the height with the optimum chemical composition of the addition reduces the susceptibility of the metal to the formation of defects in comparison with the technology in which the intermediate layer is not used [8]. The application in melting of only two main steels results in the formation of higher tensile stresses in the ingot caused by the steep gradients of the mechanical properties of the metal of the transition zone with the identical distribution of the quenched structures (Fig. 2, *II*).

The deviation of the chemical composition of the filler metal from the optimum composition, determined by equation (2) in dependence on the structural state of the main ingot can change the susceptibility to formation of cold cracks in the transition region. Figure 2, *III* shows the results of simulation of melting of ingots from the steels of the same composition, but the intermediate metal was the steel 30NCD12, wt.% (0.3 C – 0.4 Mn – 0.3 Si – 0.016 S – 0.015 P – 3.2 Ni – 0.86 Cr – 0.4 Mo – 0.17 Cu).

The transition region is characterised by the formation of areas with a higher martensite content and the simultaneous presence of the tensile axial stresses. This indicates the rapid growth of the susceptibility of the metal of the transition zone to the appearance of cold cracks as a result of the incorrect selection of the additional material. At the same time, if the additions are represented by the steel 14NiCr1.4, wt.% (0.13 C – 0.46 Mn – 0.26

Table 1. Results of calculation of the composition of the liquid pool $X(t_n + \tau)$ for the metals with the composition X_I, X_{II} and the addition with the composition X_{III}

Chemical element	X_I	X_{II}	X_{III}	$\tau = 17$ min		$\tau = 34$ min	
	%			X_{opt}	$X(t_h + \tau)$	X_{opt}	$X(t_h + \tau)$
C	0.3	0.3	0.28	0.3	0.29	0.3	0.29
Mn	0.51	0.46	0.49	0.46	0.50	0.44	0.50
Si	0.32	0.24	0.32	0.24	0.32	0.21	0.32
S	0.007	0.025	0.05	0.03	0.03	0.03	0.04
P	0.0011	0.03	0.012	0.03	0.01	0.04	0.01
Ni	3.03	2.06	0.13	2.05	1.22	1.75	0.87
Cr	0.07	1.44	1.65	1.46	1.05	1.87	1.25
Mo	0	0.37	0.22	0.37	0.14	0.49	0.16

Si – 0.012 S – 0.013 P – 3.69 Ni – 0.78 Cr – 0.04 Mo – 0.16 Cu – 0.012 Al), the amount of the quenched structures in the transition zone is very small (Fig. 2, *IV*) and the presence of the dissimilar transition does not change the susceptibility of the ingot to the formation of these defects, regardless of the large difference in comparison with the optimum composition of the addition.

Conclusions

1. To carry out the numerical analysis of the cold cracking susceptibility of the metal of the steel ingot dissimilar along the height in the electroslag melting, we developed a complex mathematical model of the kinetics of temperature, structural and stress–strain state of the metal of cylindrical ingots. Approaches have been proposed to the determination of the chemical composition of the filler metal to produce the optimum transition zone from the position of the final quality of the ingot.

2. It has been shown that in the rational selection of the filler metal the presence of the transition zone does not influence the general susceptibility of the metal of the ingot to the formation of cold cracks because the amount of the quenched structures in the areas with a tensile stresses does not exceed their volume fraction in other parts of the ingot.

3. We analysed the possibility of using, as the additional material, the steels with the chemical composition different from the optimum composition (in terms of the cold cracking susceptibility of the metal of the ingot). It has been shown that this factor may have the strong effect on the susceptibility of the metal of the transition zone to the formation of such defects because it may cause an increase of the amount of martensite in the areas with the tensile axial stresses.

References

1. Characterization and properties of dissimilar metal combinations of Fe/Al and Ti/Al-sheet materials, F. Wagner, et al., Proc. ICALEO (Orlando, Florida, USA, Sept., 2001), Orlando: LIA Congress Proc., 2001, 365–374.
2. Kahraman N., Gulenc B., Findik F. Corrosion and mechanical-microstructural aspects of dissimilar joints of Ti–6Al–4V and Al plates, Intern. J. of Impact Engineering, 2007, No. 34, 1423–1432.
3. Darwish S.M., Analysis of weld-bonded dissimilar materials, Intern. J. of Adhesion & Adhesives, 2004, No. 24, 347–354.
4. Ryabov V.R., et al., Welding of dissimilar metals and alloys, Mashinostroenie, Moscow, 1984.
5. Kuskov Yu.M., et al., Problemy Spets. Elektrometalurgii, 1995, No. 3, 24–28.
6. Prokhorov N.N., Physical processes and metals in welding, volume 2, Metallurgiya, Moscow, 1976.
7. Makhnenko V.I., et al., Zb. Nauk. Prats' NUK, 2009, No. 4, 5–12.
8. Makhnenko V.I., et al., Sovremen. Elektrometallurgiya, 2012, No. 2, 3–7.
9. Atlas of time-temperatures diagrams for irons and steels, Ed. by G. Vander Voort, Ohio: ASM Publication, 1991.
10. Atkins M. Atlas of continuous cooling transformation diagrams for engineering steels, Ohio: ASM Publication, 1980. – 260 p.
11. Christian G., Theory of transformations in metals and alloys, Mir, Moscow, 1970s.
12. Makhenko V.I., Safe service of welded joints in sections of advanced structures, Naukova Dumka, Kiev, 2010.
13. Makhnenko V.I., Calculation methods of investigating the kinetics of welding stresses and strains, Naukova Dumka, Kiev, 1976.

Behaviour of non-metallic inclusions in the structure of cast electroslag AISI 316 stainless steel

A.A. Polishko, V. Ya. Saenko, S.N. Stepanyuk, A. Yu. Tunik and I.N., Klochkov

E.O. Paton Electric Welding Institute, Kiev

The results of investigations are presented concerning the behavior of non-metallic inclusions in cast metal of stainless steel AISI of the type 316 produced using the method of electroslag remelting of consumable electrodes (ESR) and electroslag surfacing with applying liquid metal (ESS LM). The complex analysis of non-metallic inclusions at all the stages of manufacture of ESR and ESS LM ingots was carried out – from the processing of the initial metal up to the formation of ready ingots; metallographic investigations; evaluation of the dispersion of the dendritic structure. The physical and mechanical properties of cast metal of ESR and ESS LM ingots of cast metal were evaluated. Fractographic investigations and analysis of non-metallic inclusions at the fracture surfaces and fractures of specimens after their tests on static tension and impact bending were performed. Ref. 9, Tables 2, Figures 13.

The metallurgical quality of metal depends on the technology of melting steels and alloys, the technology of production of semi-finished products, heat treatment, technology of producing structural members (welding, brazing, physical-mechanical effect).

Important quality criteria, influencing the structure and properties of the cast and deformed metal, are the degree of contamination of the structural steels and alloys with non-metallic inclusions, their chemical composition and size [1, 2]. The non-metallic inclusions in the conditions of high loading in the service of components for important applications may act as stress concentrators and areas of crack nucleation and this is unacceptable. The problem becomes more serious in the case of large components, such as the casings of energy reactors.

As a result of the development at the E.O. Paton Electric Welding Institute of a new method of producing large ingots by electroslag surfacing with liquid metal ESS LM) [3, 4] it was necessary to evaluate the behaviour (transformation) of the non-metallic inclusions in the process of production of ingots by ESS LM and electroslag remelting (ESR) made of AISI 316 stainless steel and also the effect of the non-metallic inclusions on the metallurgical quality of cast metal.

For this purpose, it was necessary to carry out a detailed analysis of the non-metallic inclusions in all stages of production of the ingots by ESR and ESS LM; metallurgical investigation; evaluation of the dispersion of the dendritic structure by measuring the distance between the secondary arms of the dendrites; evaluation of the level of the physi-

cal–mechanical properties of the cast metal of the ingots produced by ESR and ESS LM; fractographic studies of the fracture surfaces of the specimens after mechanical tests.

The consumable material for ESR and ESS LM was the AISI 316 stainless steel. According to the international standard ASTM A240/A240M [5] and ASTM A480/A480M [6] the nominal composition of the steel is as follows, wt.%: <0.08 C; 2.00 Mn; <0.045 P; <0.03 S; <1.00 Si; 16.0…18.0 Cr; 10.0…14.0 Ni; 2.00…3.00 Mo. The ingots produced by ESR and ESS LM were melted by drawing using the current conducting watercooled solidification mould (CWSM) with the diameter of 350 and 180 mm, respectively, and also using a slag of the same chemical composition, wt.%: 34…40 CaF_2; 17…21 Al_2O_3; 11… 22 CaO; 14…20 SiO_2; 7…11 MgO; <2 MnO. The principal diagram of producing the ingots by ESR and ESS LM is shown in Fig. 1.

The consumable electrode for ESR was a packet consisting of six bars produced from standard rolled stock (square 80 mm).

To produce the liquid metal in ESS LM the consumable electrode was also remelted in the crucible-ladle for ESR in the form of a packet of bars (six bars) produced from standard rolled stock, square 80 mm, using the slag of the grade AN-295 (GOST 307 56-2001) of the following chemical compo-

sition, wt.%: 11…17 CaF_2, 49…56 Al_2O_3, 26…31 CaO; 2.5 SiO_2; <6 MgO. The liquid metal from the crucible-ladle for ESR in the current-conducting solidification watercooled moulds was poured in portions using metallic cold ladles with a diameter of 75 mm by periodic supply of liquid metal coated with a slag layer, with the supply from the top into the slag pool into the solidification mould in such a manner as to prevent the contents of liquid metal with the atmosphere. After pouring out each portion of liquid metal from the small ladle a thin layer of the metallic skull remains on the internal surface of the ladle which already forms in the crucible-ladle in ESR at the initial moment of contact of the cold metallic ladle with the liquid metal coated with a thick slag layer. The metallic 'cup' (skull) formed on the internal surface of the small metallic ladle can be easily separated as a result of thermal shrinkage from the small label and to use as the technological test piece for the evaluation of the degree of contamination of the metal with non-metallic inclusions in the stage of production of liquid steel in the crucible-ladle for ESR.

The non-metallic inclusions were investigated in all stages of production of completed ingots by ESR and ESS LM (Fig. 2).
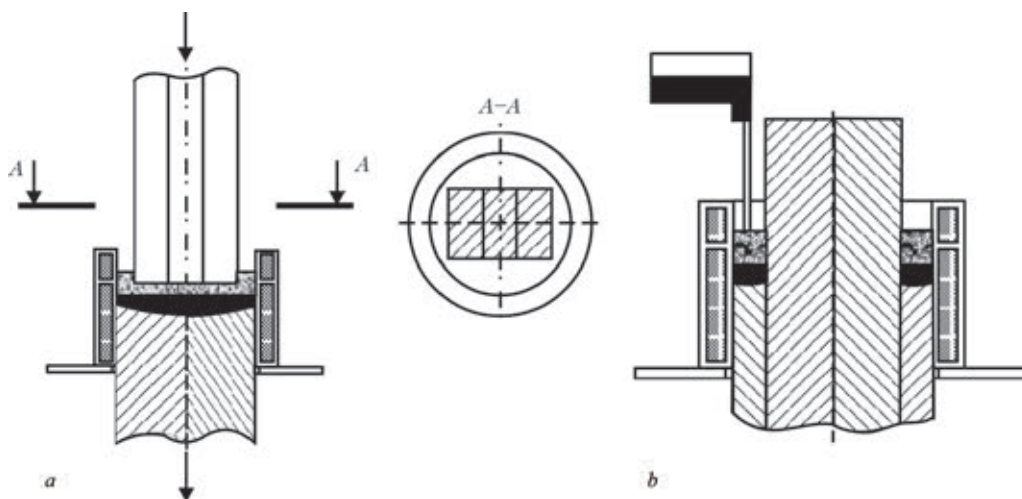
The external appearance of the consum-

Fig. 1. Diagram of the production of ESR (*a*) and ESS LM (*b*) ingots.

A.A. Polishko, V. Ya. Saenko, S.N. Stepanyuk, A. Yu. Tunik and I.N., Klochkov
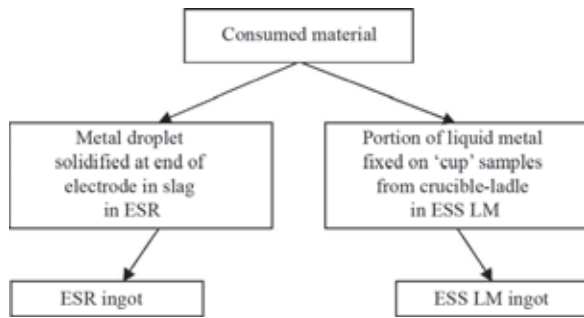
Fig. 2. Objects of investigations of non-metallic inclusions in ESR and ESS LM.

able electrode, the liquid metal in the end of the electrons solidified in the slag and the samples of liquid metal of the 'cup' type are shown in Fig. 3.

Investigations of the longitudinal macro templates, taken from the ESR and ESS LM ingots with a diameter of 350 and 180 mm made of the AISI 316 stainless steel (Fig. 4) showed the high density and homogeneity of the cast electroslag metal and absence of any defects.

Investigations of the non-metallic inclusions were carried out by electron microscopy which can be used, according to the images of the polished unetched surface, to carry out automatic separation of non-metallic inclusions on the basis of their morphology and type.

The analysis procedure may be described as follows. The nonmetallic inclusions are identified on the basis of the brightness characteristics in the BEI mode (image in the inverse electrons) or SEI (image in the secondary electrons) using the analytical

complex consisting of a JSM-35CF scanning electron microscope (JEOL, Japan) and an x-ray spectrometer with energy dispersing of x-ray quanta (INCA Energy-350, Oxford Instruments, Great Britain).

The typical special feature of this x-ray spectrum microanalysis is the localisation of analysis. The maximum region of excitation is 2 μm. The experiments were carried out at an accelerating voltage of 20 kV, magnifications from 200 to 1000, and the elemental analysis was carried out in the range from B to U. The morphological features and chemical composition on the basis of energy-dispersing spectral analysis were used for the automatic separation of the inclusions into types (elemental composition) and the dimensions of the nonmetallic inclusions were determined. The results of analysis of non-metallic inclusions were processed using a special program for the quantitative distribution of the phases and inclusions (Feature). All the results are presented in wt.%.

The non-metallic inclusions were investigated in the metal of the initial consumable electrode, the liquid metal droplet at the end of the electrode, solidified in the slack, the liquid metal sample of the type 'cup', the liquid metal of the ESR ingot and the ESS LM ingot made of AISI 316 stainless steel.

The results of evaluation of the metal of the initial consumable deformed electrode shoulders elongated band inclusions of manganese sulphide MnS up to 20 μm long. The typical sulphide inclusion for the electrode is shown in Fig. 5a. The pre-

Fig. 3. External appearance of the consumable electrode (*a* packet of welded glass) with the melted end (*a*) and also sample of liquid metal of the 'cup' type in ESS LM (*b*).
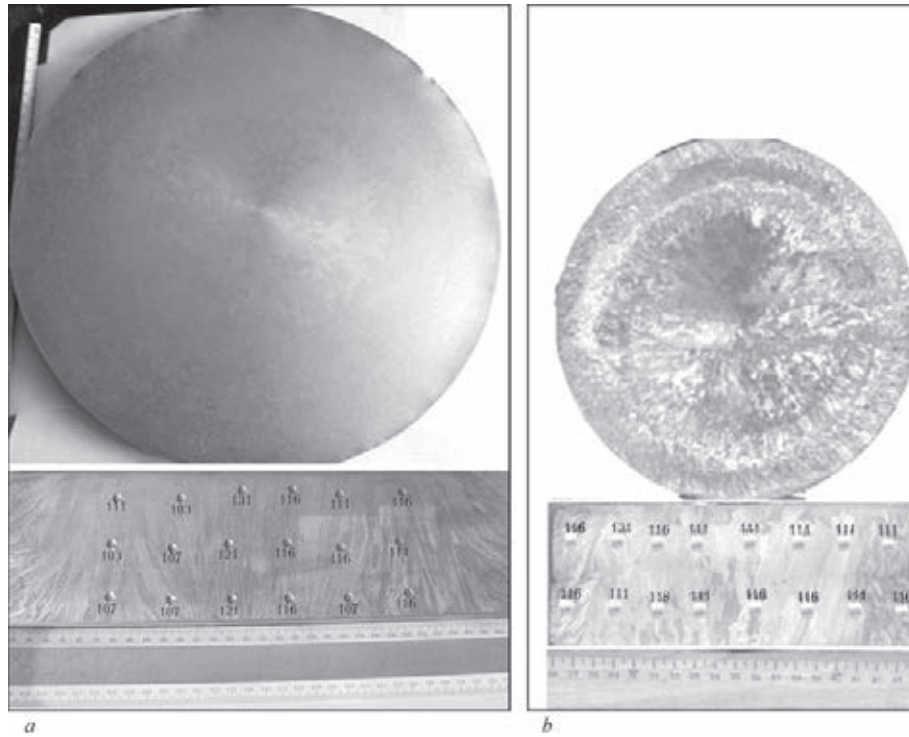
Fig. 4. Macrostructure and the distribution of hardness HB in the longitudinal templates of the ESR ingots with the diameter of 350 (*a*) and in ESS LM with a diameter of 180 mm (*b*).
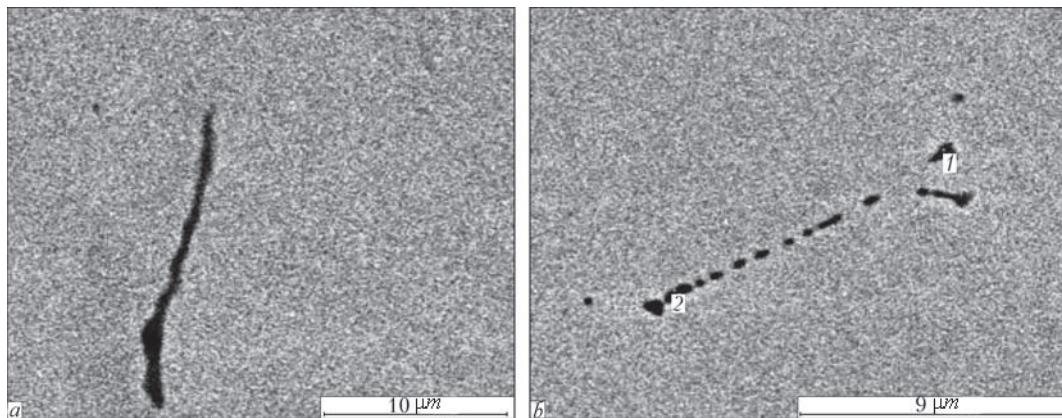
Fig. 5. Typical inclusions of the manganese sulphide in the metal of the consumable electrode (*a*) and in the pre-melting zone (*b*), BEI mode, ×4000.

Spectrum	Si	S	Cr	Mn	Ni
1	0.37	7.23	16.61	14.08	10.76
2	0.19	8.39	16.23	17.45	9.76

melting zone at a distance of approximately 2 mm from the end of the electrode surface shows both division and spheroidisationj of the inclusions in the formation of chains of globules with a size of 13 μm (Fig. 5*b*). The size of the inclusions in the chains was

0.24 – 7.0 μm.

The end of the consumable electrode in the metal of the solidified droplet after arresting the ESR process showed inclusions of the manganese sulphide MnS of the regular globular shape with a size of 0.5–1.5 μm. Examina-

A.A. Polishko, V. Ya. Saenko, S.N. Stepanyuk, A. Yu. Tunik and I.N., Klochkov

tion showed two-phase AlO–MnS inclusions with the size of up to 1 μm, not detected in the metal of the consumable electrode. This indicates the interaction of the metal with the slack already on the level of melting the electrode (Fig. 6*a*).

The metal of the 'cup' type sample is also contained mostly the inclusions of manganese sulphide of the regular globular form with the size of up to 1.5 μm, together with the inclusions of the aluminium oxide AlO with the size of up to 2 μm. Single two-phase AlO–MnS inclusions with the size of up to 2.3 μm were found (Fig. 6*b*).

The high dispersion of the inclusions in the metal of the solidified droplet and the 'cup' type specimens enabled the automatic identification of the inclusions on the basis of the chemical composition in the form of the diagram of the relative content of the AlO–MnS inclusions and the histograms of the quantitative distribution of the size in the droplet metal (Fig. 7, *I*) and in the 'cup' type samples (Fig. 7, *II*).

The cast metal of the ESR ingot contained inclusions of the manganese sulphide with the size of up to 5.4 μm, aluminium oxide up to

5.2 μm, and the two-phase AlO– MnS inclusions with the size of up to 2.9 μm (Fig. 8*b*).

The morphology of the characteristic two-phase AlO –MnS inclusion in both the ESR ingot and in the ESS LM ingot is shown in Fig. 9.

The experimental results show that the mean linear size of the inclusions in the electrode metal is 9.4 μm, in the solidified droplets, as a result of division, almost an order of magnitude smaller, 1.2 μm, and in the ESR ingot it is approximately 4 times greater, 4.7 μm, in comparison with the droplet.

In the metal of the ESS LM ingot the inclusions are larger than in the metal of the 'cup' sample (2.8 μm), but also half the size of the inclusions in the ESR ingot. Possibly, this is associated with the small volume of metal which simultaneously solidifies in ESS LM in comparison with ESR, i.e., it is likely that the dimension of the inclusions can be controlled by reducing the volume of the liquid metal pool.

Metallographic studies were carried out on the specimens of the metal of the initial consumable electrode, the liquid metal droplet at the end of the electrons solidified in the slag, the liquid metal samples of the 'cup'
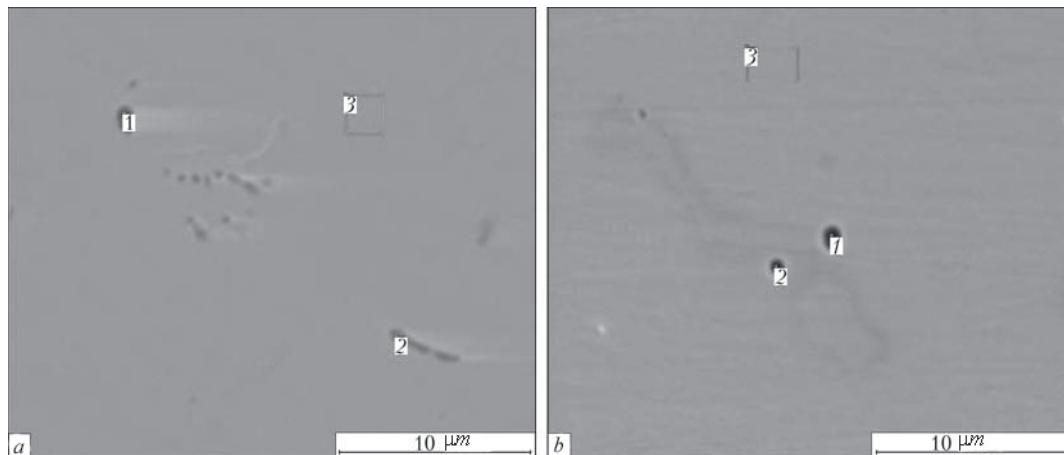
Spectrum	O	Al	Si	S	Cr	Mn	Ni
1	15.47	14.48	0.14	8.58	10.93	13,33	5.92
2	0.00	0.00	0.45	7.13	16.37	11.57	12.22
3	0.55	0.10	0.34	0.37	16.15	1.37	12.68

Spectrum	O	Si	S	Cr	Mn	Ni
1	9.43	1.99	5.96	18.73	17.56	6.72
2	5.11	1.11	2.79	19.54	9.41	9.09
3	0.00	0.00	0.00	15.89	1.25	12.42

Fig. 6. Inclusions in the metal droplet (*a*) and in the 'cup' specimen (*b*), BEI mode, ×4000.
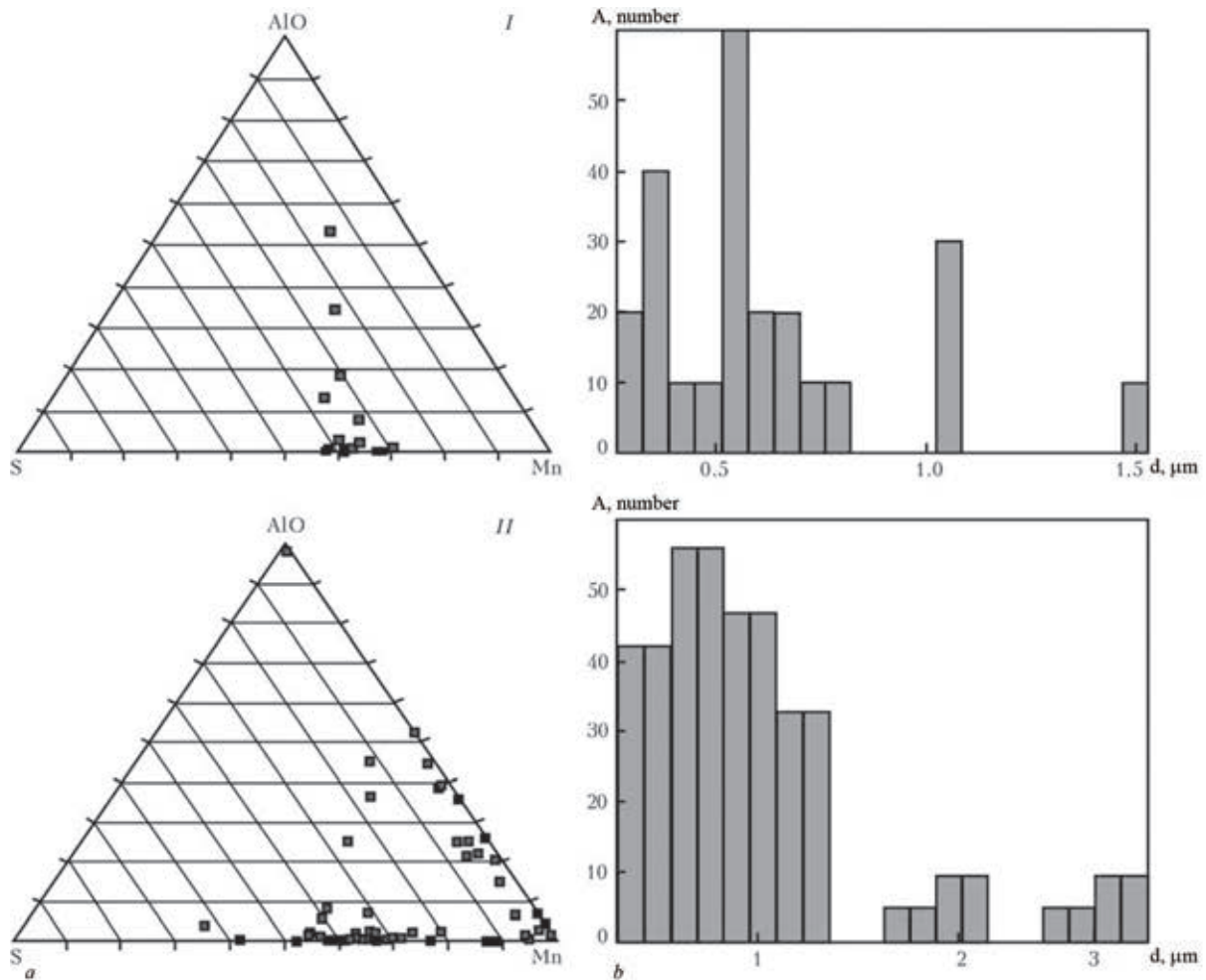
Figure 7. Diagrams of the relative content of the AlO-MnS inclusions (*a*) and the histograms of the quantitative distribution *A* of the inclusions with respect to the size *d* in the droplet metal (*I*) in the 'cup' type sample (*II*).

type, the cast metal of the ESR and ESS LM ingots of the AISI 316 stainless steel. The structure was investigated on the etched sections (electrolytic etching in a solution of chromic acid H_2CrO_4) using a Neophot-32 metallographic microscope, fitted with an attachment for digital photographic.

Traditionally, the quantitative description of the dendritic structure is carried out using the parameter in the form of the distance between the dendrites which depends on the cooling rate. An important criterion of the quality of cast metal is the dispersion of the dendritic structure represented by the distance between the secondary arms of the dendrites [7]. The distance between the arms of the dendrites of liquid metal

of the ingots, the solidified droplet and the 'cup' type samples was evaluated as a result of metallographic studies using the Tescan computer program.

The metal of the initial consumable electrode showed the banded structure typical of the deformed metal which in the pre-melting zone in the droplet of liquid metal solidified and the electrode and changes to a distinctive dendritic structure (Fig. 10). The experimental results also show that the distance between the secondary arms of the dendrites in the solidified metal droplet is 8…25 μm.

The metal of the wall of the solidified test piece of the metal of the 'cup' type in ESS LM shows clearly the bright axis of the dendrites and the dark space between the

Spectrum	O	Al	Cr	Mo
1	47.29	39.29	2.75	2.17
2	50.73	47.11	0.86	0.00

Spectrum	O	Al	Si	S	Cr	Mn	Ni
1	5.58	1.93	0.00	31.18	3.76	47.10	0.38
2	41.14	35.62	0.00	0.12	3.49	0.22	1.44
3	0.00	0.00	0.65	1.08	17.74	1.39	10.26
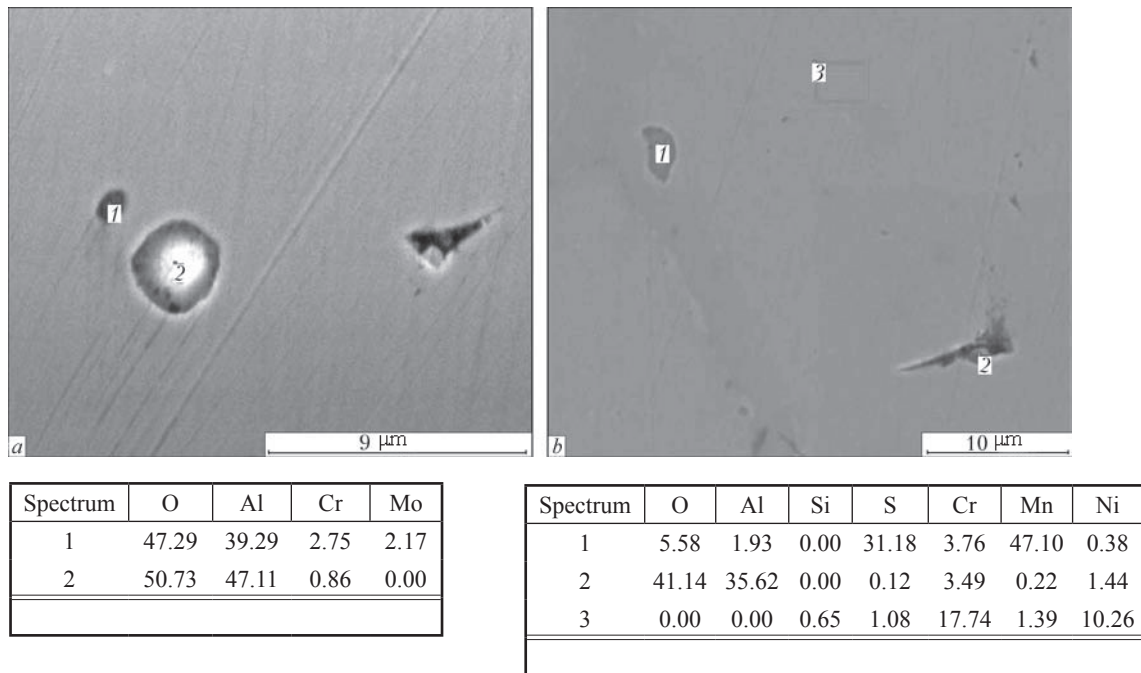
Fig. 8. Inclusions of aluminium oxide and manganese sulphide in the ESR metal (*a*) and ESS LM metal (*b*); SEI mode, ×4000.
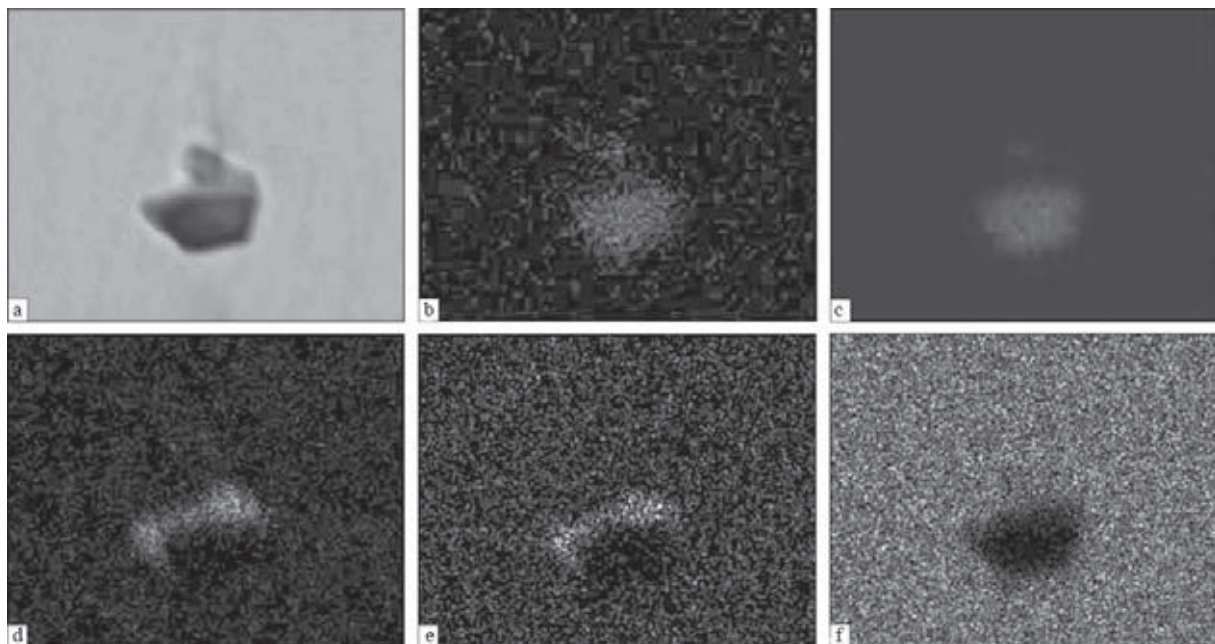
Fig. 9. Morphology of the AlO–MnS two-phase inclusion (concentration charts of the distribution of elements): *a*) electron microscope image; *b*) oxygen; *c*) aluminium; *d*) sulphur; *e*) aluminium; *f*) manganese; iron; ×1000.

dendrites. A disoriented dendritic structure was found (Fig. 11). The distances between the secondary arms of the dendrites in the metal of the 'cup' specimens was 9...35 μm.

The microstructure of the characteristic areas of the specimens of the metal of the ESR and ESS LM ingots is shown in Fig. 12. The experimental results show that the
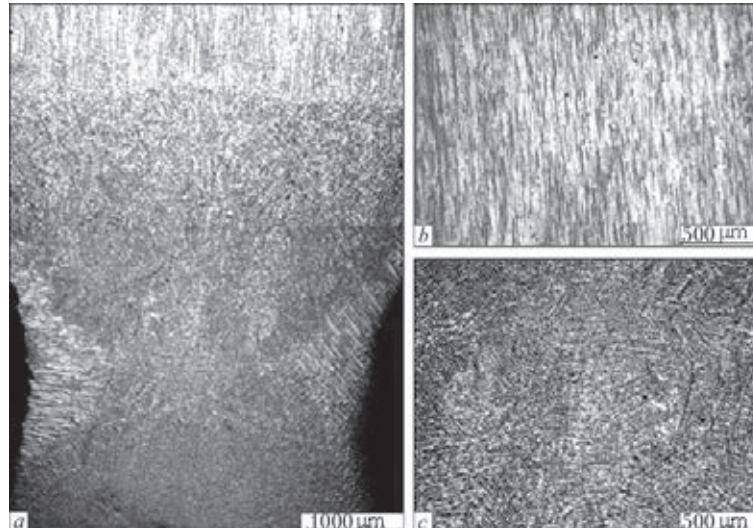
Fig. 10. Structure of the pre-melting zone and of the solidified metal droplet of the electrode tip (*a*); the microstructure of the initial (deformed) consumable ESR electrode (*b*) and of the solidified (*c*).
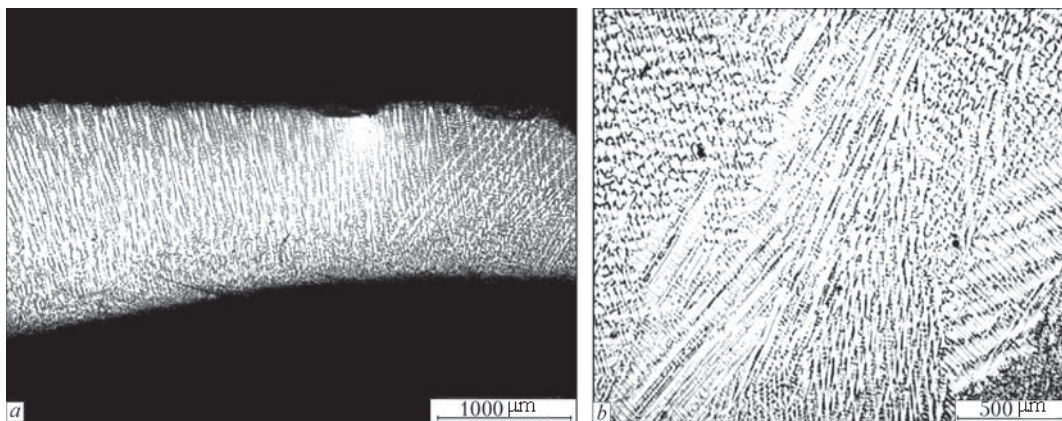
Fig. 11. Structure of the metal of the "cup" type sample in ESS LM (*a*) and its microstructure (*b*).

distance between the secondary arms of the dendrites in the ESR ingot is 96…152 μm, and in the ESS LM ingot 67…95 μm.

The following results were obtained in the experiments (Table 1).

The mechanical tests of the cast metal of the ESR and ESS LM ingots were carried out in accordance with the requirements of GOST 1497–84 in the MTS 318.25 servo-hydraulic test machine (USA) with the maximum force of 250 kN in short-term tensile loading. The results were processed using the TestWorks4 software of the MTS company. The error of the results was ±0.5%, according to the

GOST 1497–84 the permissible error is up to 1%. The impact bend test was carried out in accordance with the requirements of GOST 9454–78 on the specimens with a stress concentrator (sharp notch) in the middle with a single impact of a pendulum tester in a 2130-KM-03 pendulum pneumatic tester with the nominal potential energy of 300 J at a temperature of 20°C. The test results are presented in Table 2.

According to all parameters, the properties of the cast metal produced by ESR and ESS LM correspond to the requirements on the deformable metal according to the Metals
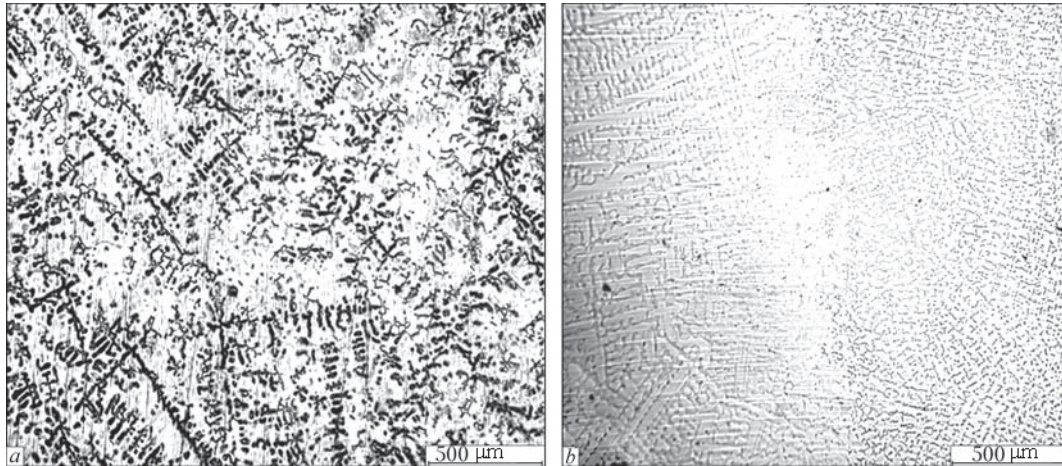
Fig. 12. Microstructure of the cast metal of the ESR (*a*) and ESS LM (*b*) ingots.

Table 1. Relationship of the dimensions of the non-metallic inclusions and the dispersion of the dendritic structure

Item studied	Distance betwen secondary dendrite arms, μm	Size of non-metallic inclusions, μm
Initial (deformed) consumable electrode	–	2.2...20.0 / 16.0
Premelting zone of consumable electrode	–	0.2...13 / 4
Metal droplet solidified at electrode tip in slag	7...25 / 17	0.3...1.3 / 1.2
Portion of liquid metal fixed in 'cup' samples from the crucible-ladle in ESS LM	9...35 / 22	0.4...2.5 / 1.8
ESR ingot	33...152 / 126	1.9...8.5 / 5.0
ESS LM ingot	28...95 / 84	1.5...5.6 / 3

The numerator gives the scatter of the values, the denominator the mean values of the results of approximately 100 measurements.

Table 2. Mechanical properties of the cast metal of ESR and ESS LM (mean values are given)

Item studied	σ_B	σ_T	δ	ψ	KCV[+20], J/cm^2
	MPa		%		
ESR ingot	433	194	43	56	197
ESS LM ingot	474	191	49	52	268

Handbook 9th addition (American Society for Metals) [8].

The results of macro- and microfractographic investigations (Fig. 13) of the fracture surfaces of the specimens of the cast metal of the ESR and ESS LM ingots after the static tensile and impact bend test show that they are fibrous, with the traces of lateral stretching. The fracture surfaces contained small facets, dimples and areas of removed metal, and bevelled areas with a silky surface formed on the sides. On the whole, the fractographic analysis results showed the ductile nature of failure [9].

Spectrum	S	Cr	Mn	Fe	Ni
1	35.01	9.09	45.00	9.68	1.23
2	23.25	11.97	43.61	18.88	2.30

Spectrum	S	Cr	Mn	Fe	Ni
1	36.51	6.56	48.63	7.30	1.01
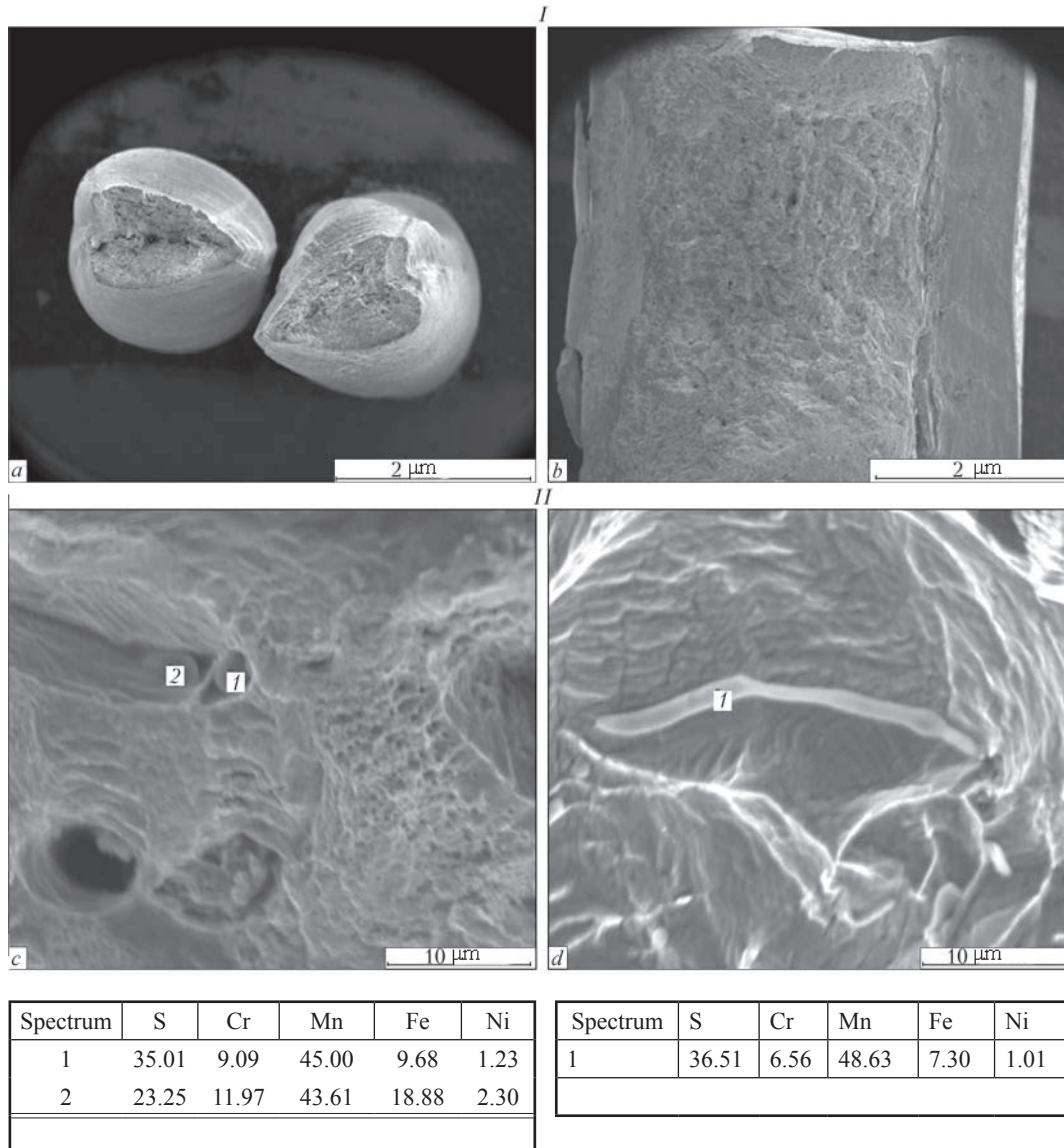
Fig. 13. Macrofractographs (*I*) and fractographs (*II*) of the fracture surfaces of the specimens after the static tensile test (*a*, *c*) and the impact bend test (*b*, *d*).

Conclusions

1. The experimental results show that the size of the non-metallic inclusions in the metal of the ESR and ESS LM ingots is respectively 1.9…8.9 and 1.9…5.6 µm (the mean value 5 and 3 µm), and as regards the chemical composition they are identical and the represented mainly by the aluminium oxides and manganese sulphide. Two-phase inclusions – aluminium oxide – manganese sulphide, were also detected.

2. The mean size of the non-metallic inclusions (mostly manganese sulphide) in the initial deformed metal is equal to 16 µm, with the maximum size of the sulphide bands reaching 20 µm.

3. In ESR the metal of the consumable electrode in the direction to the melting slag results shows disintegration and dissolution of the sulphide bands, in the pre-melting zone the mean size of these inclusions equals 4.0 µm, and in the metal droplets solidified on the molten end of the ESR electrode they

transform the mean size of 1.3 µm. The mean size of the non-metallic inclusions in the metal of the solidified 'cup close' specimen, taken from the metallic melt of the ESR crucible-ladle is 1.8 µm. The metal of both the droplet and of the 'cup' sample showed two-phase aluminium oxide-manganese sulphide nonmetallic inclusions.

4. The relationship was determined between the dimensions of the non-metallic inclusions in the cast metal of the AISI 316 stainless steel and the dispersion of the dendrite structure, determined by the distances between the secondary arms of the dendrites.

5. The experimental results show that the cast metal of the ESR and ESS LM ingots with the diameters of 350 and 180 mm has similar strength characteristics and satisfy the requirements on the deformed metal in the Metals Handbook Ninth addition (American Society for Metals). It was also shown that the impact toughness KCV^{+20} of the ESS LM cast metal is 268 J/cm^2, and that of the ESR ingot 197 J/cm^2. The higher values of the impact toughness are evidently associated with the high dispersion of the dendritic structure of the ESS LM metal.

6. Fractographic studies of the fracture surfaces of the specimens after the tests indicate the ductile failure of the cast metal of the ESR and ESS LM ingots of the AISI 316 stainless steel.

References

1. Paton B.E., et al., Problemy Spets. Elektrometalurgii, 1989, No. 2, 3–8.
2. Medovar B.I., Rafin. Pereplavy, Naukova dumka, Kiev, 1974, 3–5.
3. Paton B.E., et al., Sovremen. Elektrometallurgiya, 2007, No. 1, 3–7.
4. Medovar L.B., et al., Parent 94333, Ukraine, MPK V 22 D 19/16; S 22 V 9/18, A method of production of heavy metal ingots, 26.4.2011, Bull. No. 8.
5. ASTM A240/A240M. Specification for heat-resisting chromium and chromium-nickel stainless steel plate, sheet, and strip for pressure vessels, New-York: American Society for Testing and Materials, 2003.
6. *ASTM* A480/A480M. General requirements for flat-rolled stainless and heat-resisting steel plate, sheet, and strip. – New-York: American Society for Testing and Materials, 2003.
7. Fleming M., Solidification processes, translated from the English, Moscow, Mir, 1977.
8. *Metals* Handbook 9th Edition. V. 3. Properties and selectionstainless steels, tool materials, and special purpose metals. – New-York: American Society for Metals, 1980.
9. Fellows G., Fractography and atlas of fractographs, a Handbook, translated from the English, Metallurgiya, Moscow, 1982.

Conditions for production of defect free quasi-crystalline Al–Cu–Fe coatings by electron beam vacuum deposition

S.S. Polishchuk[1], A.I. Ustinov[2], V.A. Telichko[2], G. Mozdzen[3], A. Mestallinger[3] and T.V. Mel'nichenko[2]

[1]*G.V. Kurdyumov Institute of Metal Physics, National Academy of Sciences of Ukraine, Akad. Vernadskoho 36, 03680 Kiev*
[2] *E.O. Paton Electric Welding Institute, Kiev*
[3]*Aerospace and Advanced Composites GmbH, Viktor Kaplan-Strasse 2, 2700 Wiender Neustadt, Austria*

It is shown that the coatings with a quasi-crystalline structure of the Al–Cu–Fe system were produced by the method of electron beam deposition in vacuum at a substrate temperature of 570...870 K. Through cracks are sometimes revealed in coatings deposited by this method. It was found by X-ray diffraction method that the residual stresses in defect-free Al–Cu–Fe coatings are growing with increase in temperature of their deposition that is due to the growth of thermal stresses, caused by the difference in the linear coefficients of thermal expansion (LCTE) of the substrate and the coating. In cases, when elastic stresses reach some critical value in the process of substrate cooling to room temperature, they lead to the formation of through cracks. LCTE ($\alpha_c = (17.1\pm1.3)\cdot10^{-6}/K^{-1}$) of coating material was determined from the analysis of dependence of level of residual stresses in coating on deposition temperature. Fracture toughness of coating was evaluated as $G = 15.7\pm1.1$. J·m^{-2}. The obtained characteristics of Al–Cu–Fe coating were used for calculation of its critical thickness at which the defect-free structure of surface is retained depending on substrate material and deposition temperature. Experimental studies of structure of surface of coatings, deposited on substrates of steels K600, K890 and K110 at different temperatures, showed that the through cracking of coatings was not observed in those cases when their thickness was less than calculated critical one. Ref.19, Tables 5, Figures 10.

Key words: quasi-crystal; coating; electron bean deposition in vacuum; cracks; deposition temperature; thermal stresses in coatings; critical thickness of coating

Aluminium alloys with the quasi-crystalline structure are characterised by the unique combination of the properties such as the high values of hardness (7…10 GPa) and elasticity modulus (120… 200 GPa), the relatively low friction coefficient (on diamond 0.07…0.10; on steel 0.19…0.22), low heat conductivity (0.8…2.0 W/(m·K)), low surface energy (28…30 mJ/m^2), high corrosion resistance, and others [1]. These properties and also the relatively low price of the metals, present in these alloys, make them a promising for

application is the base for a new class of functional coatings (wear resistant, thermal barrier, antifriction, anti-burning, etc) [2].

It has been shown that the method of electron beam deposition (EBD) of coatings results in the formation of the quasi-crystalline structure directly in the process of condensation of the vapour phase on the substrate at a temperature of 570…870 K [3–5]. If the linear coefficient of thermal expansion (LCTE) of the material of the substrate is lower than in the quasi-crystalline Al-Cu-Fe

S.S. Polishchuk1, A.I. Ustinov, V.A. Telichko, G. Mozdzen, A. Mestallinger and T.V. Mel'nichenko

Table 1. Chemical composition of the ingots of Al–Cu–Fe alloy, wt.%

Ingot No.	Al	Cu	Fe
1	66.54	20.18	13.28
2	66.11	16.45	17.44
3	59.74	26.69	13.57
4	62.64	24.35	13.01

alloy, in the cooling of the substrate–coating system from the deposition temperature to room temperature tensile stresses may appear in the coating.

The formation of residual tensile stresses in the quasi-crystalline coatings may cause cracking [6] and separation of the coatings from the substrate [7] which, in the final analysis, influences the wear resistance and fatigue strength of these coatings. At the same time, from the practical viewpoint it is important to ensure that the coating withstands residual stresses without formation of cracks or disruption of its adhesion with the substrate.

Thus, the aim of the present work is the determination of the conditions required for the formation of defect-free quasi-crystalline coatings with good adhesion to the substrates of different. To solve the problem, the x-ray diffraction method was used to investigate the level of residual stresses in the deposited Al–Cu–Fe coatings. The dependence of the thermal stresses in the coatings on the deposition temperature of the coatings was used to determine the linear coefficient of thermal expansion of the material of the coating and its fracture toughness. Consequently, it was possible to determine, for the given material of the substrate and the deposition temperature of the coatings, the critical thickness values below which no cracks appear in the coating. The calculated values of the critical

thickness are in satisfactory agreement with the experimental studies of the structure of the surface of the coatings deposited on the substrate from different materials.

Production and investigation of the coatings. The ingots of the Al–Cu–Fe alloy of different chemical composition (Table 1) with a diameter of 50 mm and 250 mm long were produced by plasma arc melting in argon. The ingots were produced using aluminium grade A0, copper M1U and commercial purity iron (Armco iron).

The coatings were produced by the single-crucible electron beam stationary evaporation method in which an ingot is supplied at a constant rate into the liquid pool at the end surface. In this method, the ingots were placed in a copper water-cooled crucible.

The composition of the coating in the stationary evaporation conditions is similar to the composition of the initial ingot. Using ingots of different chemical composition it was possible to vary the composition of the deposited coatings. The coatings with the thickness of 10–70 μm were produced on the substrate of different steels produced by Bohler company (Table 2) at a temperature of 570–870 K at a deposition rate of 50 nm/s. To ensure good adhesion of the coating on the substrate, a thin layer of nickel (thickness 1–2 μm) was deposited in advance on the surface of the substrate.

The chemical composition of the coatings was determined by x-ray fluorescence analysis in equipment X' Unique II. The distribution of the chemical elements in the thickness of the coating was determined using Energy-200 microanalyser installed on a CamScan4 scanning electron microscope. The structure was investigated using DRON-4 x-ray diffractometer in Cu-K_α radiation.

Table 2. Materials of the substrates (mean values), wt.%

Steel grade	C	Si	Mn	Cr	Mo	Ni	V	W	Co	Russian analogue
BOHLER K600	0.45	0.25	0.40	1.30	0.25	4.00	–	–	–	38KhN3MA
BOHLER K110	1.55	0.25	0.35	11.80	0.80	–	0.95	–	–	Kh12MF, Kh12F1
BOHLER K890	0.85	0.55	–	4.35	2.8	–	2.1	2.55	4.5	–

As shown in [8], the macrostresses in the quasi-crystalline materials can be measured using the x-ray diffraction method $\sin^2 \psi$ [9]. Assuming the presence of the biaxial residual stresses in the coating ($\sigma_{11} = \sigma_{22} = \sigma_{\parallel}$ and $\sigma_{13} = \sigma_{23} = \sigma_{12} = 0$), the deformation in the given direction is determined by the equation presented in [10]:

$$\varepsilon(HKL, \o) = \left[\frac{1}{2}s_2(HKL)\sin^2 \o + 2s_1(HKL)\right]\sigma_{\parallel};$$
$$s_1(hkl) = -\frac{v(HKL)}{E(HKL)}; \quad \frac{s_2(hkl)}{2} = \frac{1+v(HKL)}{E(HKL)} \tag{1}$$

where ε is the strain; σ is the stress; s_1 and $\frac{1}{2}s_2$ are the diffraction elastic constants; (HKL) and $E(HKL)$ are respectively the Poisson coefficient and the Young modulus for the crystallographic direction [HKL]; ψ is the angle of inclination of the specimen around the axis $A-A$ (Fig. 1). In the case of the isotropic material (HKL)) $= v$ and $E(HKL) = E$. The stress was determined from the angle of inclination of the linear interpolation of the dependence of ε (HKL, ψ) on $\sin^2 \psi$.

In the quasi-crystalline material, the stress ε (HKL, ψ) along the direction [HKL], was calculated from the experimentally determined values of the lattice parameter of the quasi crystal a_{6D} in accordance with the expression:

$$\varepsilon(HKL, \psi) = (a_{6D}(HKL, \psi) - a_{6D0}(HKL))/a_{6D0}(HKL),$$

where, according to the definition presented in [10]: $H = h + h'\tau$; $K = k + k'\tau$; $L = l + l'\tau$, where h, h', k, k', l and l' are integers;
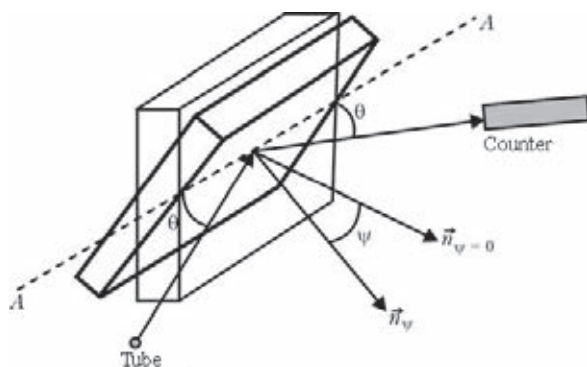
Fig. 1. Diagram of recording using the method $\sin^2 \psi$; n is the normal to the surface of the specimen; is the angle of inclination of the specimen around the axis $A-A$.

$\tau = (1 + \sqrt{5})/2$; a_{6D} and a_{6D0} are the lattice parameters of the quasi-crystal in the presence and absence of the stresses, respectively. The parameters a_{6D} were determined using the equation $a_{6D} = \frac{\lambda}{2\sin\theta}\frac{\sqrt{N + M_\tau}}{2(2+\tau)}$, where λ is the wavelength; θ is the Bragg angle for (N, M) of the reflection of the icosaherdal structure in accordance with the indexation system proposed by G. Khan [10] on the basis of the position of the reflection (52, 84), which corresponds to the direction along the axis of symmetry of the second-order of the quasi-crystalline icosahedral structure.

It should be mentioned that in the case of the two-phase coating (quasi-crystalline *ico*- and cubic β-phases) the mean values of the stress for each of the phases $\langle\sigma_{\parallel}\rangle_{ico}$ and $\langle\sigma_{\parallel}\rangle_\beta$ be determined as follows [11]:

$$\langle\sigma_{\parallel}\rangle_{ico} = \sigma_{\parallel}^m + \langle\sigma_{\parallel}^{pm}\rangle_{ico}; \quad \langle\sigma_{\parallel}\rangle_\beta = \sigma_{\parallel}^m + \langle\sigma_{\parallel}^{pm}\rangle_\beta;$$
$$(1-f)\langle\sigma_{\parallel}^{pm}\rangle_{ico} + f\langle\sigma_{\parallel}^{pm}\rangle_\beta = 0 \tag{2}$$

where $\sigma_{\parallel}^m$ is the macrostress (the same in both phases), $\langle\sigma_{\parallel}^{pm}\rangle_{ico}$ and $\langle\sigma_{\parallel}^{pm}\rangle_\beta$ are the pseudo-macrostresses in respectively the ico- and β-phases; f is the volume fraction of the cubic β-phase in the two-phase coating. The pseudo-macrostresses [12] form as a result of the macroscopic heterogeneity of the grains in the polycrystal and also the difference of the thermal expansion coefficients, the yield limit, the elastic modulus of the grains of the two phases. Measurements of the mean stresses for both quasi-crystalline and cubic phases make it possible to determine the values of the macrostresses (formed as a result of the difference in the linear coefficients of thermal expansion of the substrate and the coating) and also the pseudo-macrostresses (because of the different values of the linear coefficient of thermal expansion and elastic properties of the grains of the two phases).

Characteristics of the structure of the coatings. The typical macrostructure of the cross-section of the Al–Cu–Fe the coating on the substrate made of a stainless steel is shown
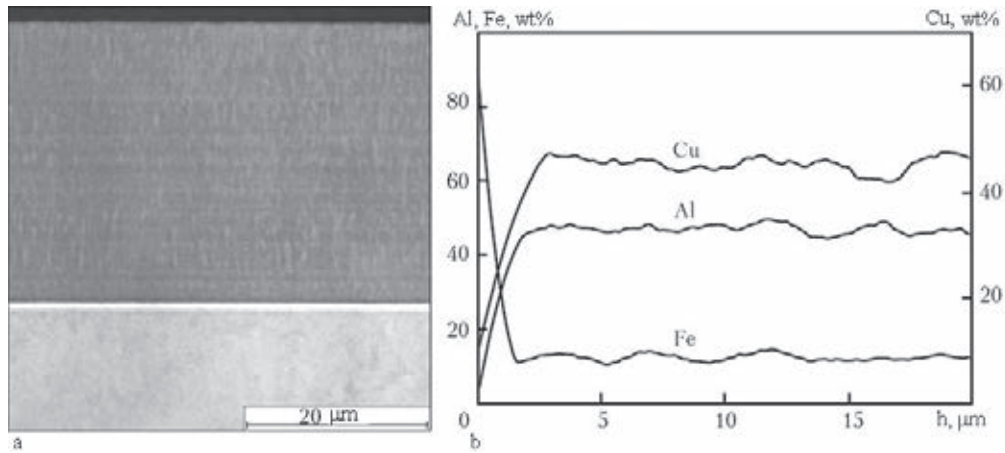
S.S. Polishchuk1, A.I. Ustinov, V.A. Telichko, G. Mozdzen, A. Mestallinger and T.V. Mel'nichenko

Fig. 2. Microstructure of the cross-section of the coating based on the Al-Cu-Fe alloy (*a*) and the distribution of aluminium, copper and iron in the thickness *h* of the coating (*b*).
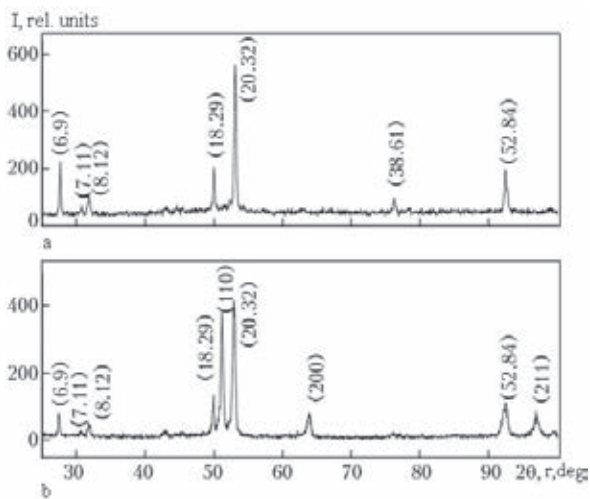

Fig. 3. X-ray diagrams of the single-phase quasi crystalline Al–Cu–Fe (*a*) and two-phase (*ico* + β) (*b*) coatings seven, *I* is the intensity.

in Fig. 2*a*. In may be seen that the coating is free from macropores, and at the interface between the substrate in the coating there are no defects are determined by the separation of the coating from the substrate.

The distribution of the concentration of the elements along the cross-section of the coatings indicates that the coating is homogeneous in the thickness (Fig. 2*b*).

The chemical composition of the coatings, determined by the method of energy-dispersing x-ray spectroscopy is shown in Table 3. X-ray studies of the structure of the produced

Al–Cu–Fe coatings showed that depending on the chemical composition and they may have a single-phase quasi-crystalline *ico-* or heterogeneous structure, containing the *ico*-phase and the cubic β-phase (Fig. 3). The estimate of the volume fraction of the quasi-crystalline phase and the cubic β-phase in the Al–Cu–Cu coatings using the x-ray diffraction data is presented in Table 3.

The investigation of the microstructure of the surface of the coatings of different thickness, deposited on the substrate of different materials (steel grades) shows that in some cases the coatings did not contain any cracks (Fig. 4*a*), whereas in other cases examination showed the formation of a network of cracks (Fig. 4 *b*). Figure 4*b* shows that the cracks are uniformly distributed over the entire surface of the coating. Detailed analysis of the mutual distribution of the cracks and other defects (solidified droplets, roughness, etc) on the surface of the coating indicates that there is no correlation between them.

Analysis of the microstructure of the cross-section of the coatings in which the cracks were detected shows that they are usually oriented normal to the interface between the substrate in the coating and propagate across the coating (Fig. 5). In addition to this, the crack orientation does not correlate with microstructural characteristics such as the boundaries of the columnar grains, cavities,

Table 3. Properties of the coatings

Specimen No.	Substrate	Substrate temperature T_s, K	LTEC of substrate material, $1 \cdot 10^6$/K	Chemical composition	Phase composition, vol%	Макронапряжение, МПа
1	K110	570	11.0	$Al_{64.0}Cu_{25.1}Fe_{10.9}$	100*ico*	360
2	K110	850	12.0	$Al_{64.0}Cu_{25.1}Fe_{10.9}$	100*ico*	600
3	K110	720	11.7	$Al_{60.1}Cu_{25.6}Fe_{14.2}$	50*ico* + 50β	555
4	K890	690	11.9	$Al_{57.9}Cu_{28.2}Fe_{13.9}$	60*ico* + 40β	390
5	K890	770	12.1	$Al_{56}Cu_{31.2}Fe_{12.8}$	60*ico* + 40β	440
6	K890	810	12.2	$Al_{58.1}Cu_{29.2}Fe_{12.7}$	60*ico* + 40β	500
7	K600	890	14.5	$Al_{56.0}Cu_{23.4}Fe_{20.6}$	50*ico* + 50β	370
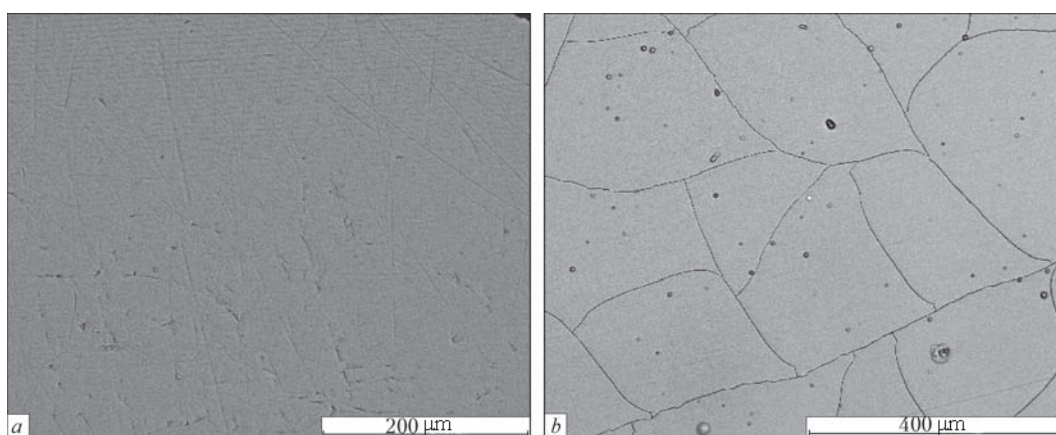
Fig. 4. Characteristic microstructure of the coatings without (*a*) and with cracks (*b*).
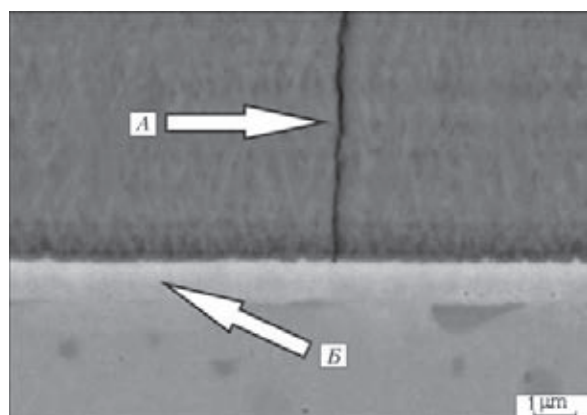
Fig. 5. Microstructure of the cross-section of the Al–Cu–Fe coating, deposited on the K890 steel substrate; the arrows indicate the crack propagating along the interface *A* and nickel interlayer Б with a thickness of 1 µm.

etc. Consequently, it may be assumed that the formation of cracks is the consequence of the relaxation of stresses which can form in the Al–Cu–Fe coatings both as a result of condensation of the vapour and as a result of the differences in the coefficients of linear thermal expansion of the substrate and the coating. Since the cracks propagate only in the quasi-crystalline layer of the coating and is not penetrate into the intermediate layer based on nickel, it may be concluded that the intermediate layer is not only ensure satisfactory adhesion between the substrate and the coating but also prevents the penetration of cracks from the coating into the substrate. The resistance of the intermediate layer to the penetration of cracks may be associated with the realisation in the layer of different mechanisms of stress relaxation whereas the materials with the quasi-crystalline structure at temperatures lower than 870 K are not capable of stress relaxation as a result of plastic deformation.

The conditions of formation of the cracks as a result of the relaxation of elastic stresses

S.S. Polishchuk1, A.I. Ustinov, V.A. Telichko, G. Mozdzen, A. Mestallinger and T.V. Mel'nichenko

in the coating based on the brittle material will be analysed.

Conditions of formation of cracks in the Al–Cu–Fe coatings. The currently available models of the fracture mechanics of brittle materials in the form of coatings are based on simple analysis proposed back in the 1920s of the previous century by Griffith for calculating the cracking of brittle materials. In this approach, it is assumed that the existence of cracks and other defects in the materials play the controlling role in the determination of the strength. The condition of mechanical stability of the material with a crack according to Griffith assumes that is fracture toughness Γ should be higher than the rate of release of energy G during propagation of the crack through the material, i.e., $\Gamma > G$ [6].

The rate of release of energy G, associated with continuous cracking (the energy required for the cracking process), is determined as follows

$$G = \frac{\pi\sigma^2 h}{2E_1}g(\alpha,\beta); \quad \overline{E}_j = \frac{E_j}{1-v_j^2}(j=1.2);$$

$$\alpha = \frac{\overline{E}_1 - \overline{E}_2}{\overline{E}_1 + \overline{E}_2}; \quad \beta = \frac{\mu_1(k_2-1)-\mu_2(k_1-1)}{\mu_1(k_2+1)-\mu_2(k_1+1)} \tag{3}$$

where σ is the stress in the coating; h is the thickness of the coating; E_1, v_1 and E_2 v_2 are respectively the Young modulus and the Poisson coefficient for the materials of the coating on the substrate; $g(\alpha, \beta)$ is the dimensionless parameter which depends on the parameters α and β [13]; μ_j ($j = 1,2$) is the shear modulus; $k_j = 3 - 4_j$ ($j = 1,2$). Cracking takes place when $G > \Gamma$, where Γ is the fracture toughness or critical rate of energy release, required for the propagation of the crack in the coating. It should be mentioned that Γ is associated with the critical stress intensity factor of the first mode of deformation of the coating material K_{IC} by the relationship $\Gamma = (K_{IC})^2/D_1$.

The minimum thickness of the coating (will be referred to as the critical thickness h_c) in which the crack can form can be estimated from the relationship $\Gamma \approx G$. Subsequently, using the equation (3), the critical thickness

of the coating can be estimated from the equation

$$h_c = \frac{2\Gamma\overline{E}_1}{\pi\sigma^2 g(\alpha,\beta)} \tag{4}$$

Thus, determining the values included in the equation (4), we can calculate the critical thickness below which the cracks are not form in the coating. For this purpose, it is necessary to determine by experiments the level of stresses, formed in the coating on the fracture toughness of the coating material.

Evaluation of residual stresses in coatings. For the experimental evaluation of the residual macrostresses in the coatings, experiments were carried out with coatings with a thickness of 10…30 μm in which cracking was not detected. The following values of the elasticity modulus for the quasi-crystalline and cubic phases of the Al–Cu–Fe coatings, previously determined by nanoindentation were used: E_{ico} = 171±2 GPa; E_β = 162±4 GPa [14]. It should be mentioned that the value of the elasticity modulus for the quasi-crystalline coatings is almost identical with the value for the sick quasi-crystalline material, determined by the resonance method E = 168 GPa [15]. We also use the Poisson were efficient for the quasi-crystalline phase, determined in [15]: v_{ico} = 0.232. For the cubic phase it was assumed that v_β = 0.3.

In the case of heterophase coatings the macrostresses were determined from the position of the peaks (52, 84) and (211) are respectively for the quasi-crystalline and cubic phases. Figure 6 shows the dependences $(a_{6D} - a_{6D0})/a_{6D0}$ and $(d - d_0)/d_0$ on $\sin^2\psi$ for the quasi-crystalline *ico*-phase in the cubic β-phase, respectively, in the Al–Cu–Fe coating. The quasi-crystalline and cubic phases in this coating and to approximately the same volume fraction, 50% (specimen 3, Table 3). In may be seen that those dependences can be interpolated by the linear function with a good correlation factor. The mean values of the stresses for both phases, calculated using equation (1), are shown in Fig. 6. The values of the mean stresses for the quasi-crystalline σ_{ico} and cubic σβ
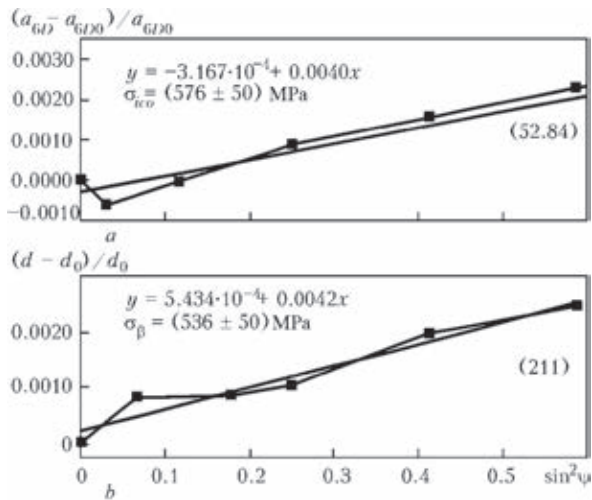
Fig. 6. Dependences $(a_{6D} - a_{6D0})/a_{6D0}$ and $(d - d_0)/d_0$ sin^2 ψ respectively for the quasi-crystalline ico-phase and the cubic β-phase in the Al–Cu–Fe coating.

phases are similar – respectively (576±50) and (536±50) MPa. This may be caused by the fact that the quasi-crystalline and cubic phases are characterised by similar values of the coefficient of linear thermal expansion. The microstresses (pseudo-macrostresses) formed in both phases are associated with the microscopic heterogeneity of the grains, the differences in the yield limit of the grains of the quasi-crystalline and cubic phases, and have relatively low values (±20 MPa). The level of the macrostresses in the two-phase coatings were calculated using the system of equations (2). In cases in which the sharp

texture of the cubic β-phase at some positions of the angle ψ causes the peak (211) to have insufficient intensity, the macrostresses $\sigma_{\parallel}^m$ were evaluated assuming $\sigma_{\parallel}^m \cong \sigma_{\parallel}^{ico}$.

Figure 7 shows the dependences $(a_{6D} - a_{6D0})/a_{6D0}$ on sin^2 ψ for the single-phase quasi-crystalline coating, deposited on the steel substrate of K110 steel, heated to different temperatures. It may be seen that the level of the macrostresses in the coating depends on the temperature of the substrate.

Table 3 shows the results of measurement of the residual stresses in the Al–Cu–Fe coatings, deposited on different substrates (steels K110, K890, K600). The level of the macrostresses in the coating depends both on the temperature and on the coefficient of linear thermal expansion of the substrate material.

Determination of the coefficient of linear thermal expansion of the coating. The general stresses in the vacuum coatings consisted of thermal and internal stresses. The thermal stresses caused by the difference in the values of the coefficients of linear thermal expansion of the materials of the coating on the substrate. Internal stresses form as a result of the accumulation effect of the crystallographic defects which penetrate into the coating during deposition. Thus, the general stress in the coating can be determined using the following equation

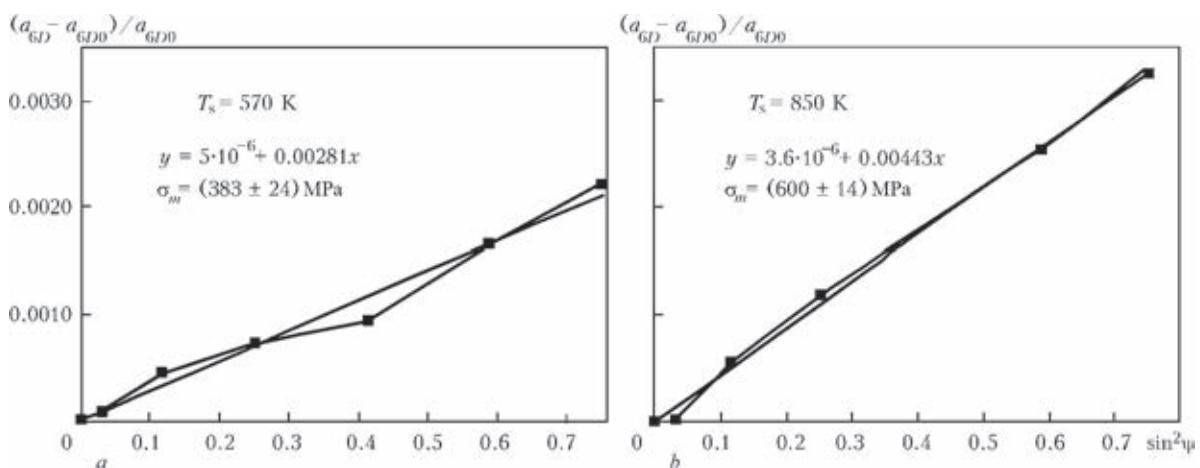

Fig. 7. The dependence $(a_{6D} - a_{6D0})/a_{6D0}$ on sin^2 ψ constructed on the basis of the positions of the reflection (52, 84) of the quasi crystalline phase of the Al–Cu–Fe coating, deposited on the steel (steel K110) substrate.

$$\sigma = \sigma_i + \sigma_{th} = \sigma_i + (\alpha_c - \alpha_s)\Delta T \frac{E_c}{1 - v_c} \qquad (5)$$

where σ_i is the internal stress in the coating; σ_{th} is the thermal stress; α_c, E_c, v_c is respectively the coefficient of linear thermal expansion, the Young modulus and the Poisson coefficient for the coating material; α_s is the coefficient of linear thermal expansion of the substrate material; ΔT is the difference between the deposition temperature and room temperature.

The internal stresses σ_i depend strongly on the deposition conditions and, in particular, on the parameter T/T_m (T is the substrate temperature; T_m is the melting point of the coating material). In this case, we analysed the coatings, deposited at the substrate temperatures of 570–870 K, which corresponds to the range of the ratio T/T_m from 0.50 to 0.77 (the melting point of the icosahedral phase in the Al–Cu–Fe system, $T_m \approx 1140$ K [16]). It is assumed that at the substrate temperatures corresponding to $T/T_m > 0.2$, the internal stresses, formed during growth of the coating, and relaxes a result of the recovery phenomena and recrystallisation [17]. Thus, we can ignore the value of the internal stresses σ_i in equation (5) is a result of the processes of recovery and recrystallisation in the coatings.

Figure 8 shows the dependence of the value $\left(\sigma + \alpha_s \frac{E_c}{1 - v_c}\Delta T\right)$ on the difference of the deposition temperature in the room temperature ΔT. The linear approximation of this dependence gives the following values of the coefficient of linear thermal expansion: $\alpha_c = (17.1 \pm 1.3) \cdot 10^{-6}$ K^{-1}.

Evaluation of the fracture toughness of coatings. To evaluate the fracture toughness of the quasi-crystalline coatings, we use the relationship $\Gamma \approx G$ which is satisfied at $h \approx h_c$. In the case of the quasi-crystalline coating on the steel substrate, the substitution $E_1 = 168$ GPa, $v_1 = 0.232$, $\mu_1 = 68$ GPa [14] and $E_2 = 210$ GPa, $v2 = 0.29$, $\mu_1 = 79.3$ GPa into equation (3) gives $\alpha - 0.1$ and $\beta \approx -0.06$ which corresponds to the value of the dimensionless parameter $g(\alpha, \beta) = 1.184$ [13].
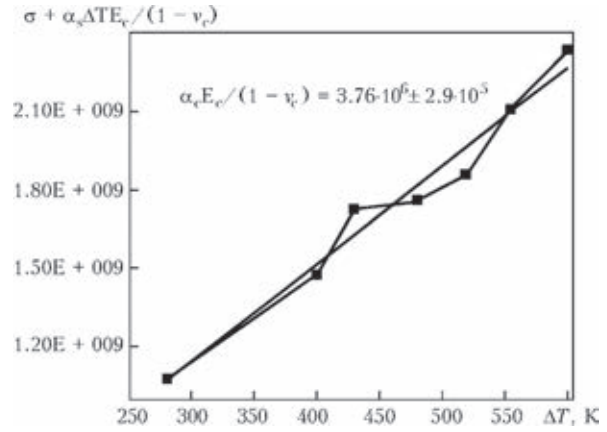

Fig. 8. Dependence of $\left(\sigma + \alpha_s \frac{E_c}{1 - v_c}\Delta T\right)$ on the difference of the deposition temperature and the room temperature ΔT, the linear interpolation of the dependence can be used to determine the coefficient of linear thermal expansion $\alpha_c = (17.1 \pm 1.3) \cdot 10^{-6}$ K^{-1}.

Consequently, the fracture toughness of the coating at the given critical thickness taking into account equation (4) is determined by the relationship

$$\Gamma = 1.859((\alpha_c - \alpha_s)\Delta T)^2 E_c h_c \frac{1 + v_c}{1 - v_c} \qquad (6)$$

To determine the critical thickness of the coating, the substrate of the K110 steel with the temperature gradient from 570 to 870 K was deposited with a coating 10 μm thick. Figure 9 shows the surfaces of the Al–Cu–Fe coatings, deposited at different substrate temperatures. In may be seen that the cracks in the coating appear during deposition on the substrate at a temperature T_s between 600 and 620 K, which corresponds to thermal stresses in the range from 375 to 400 MPa.

Figure 9 shows that the increase of the deposition temperature results in a reduction of the distance between the cracks (Fig. 8c, d) which, as shown in [6, 18] is also associated with the increase of the level of stresses in these coatings. At the

Using the relationship (6), the fracture toughness of the Al–Cu–Fe coating can be estimated at 14.7…16.8 J·M^{-2} or in terms of the critical stress intensity factor of the first deformation mode K_{1c} as 1.57…1.68 MPa·m$^{1/2}$. The results of identical experiments with the
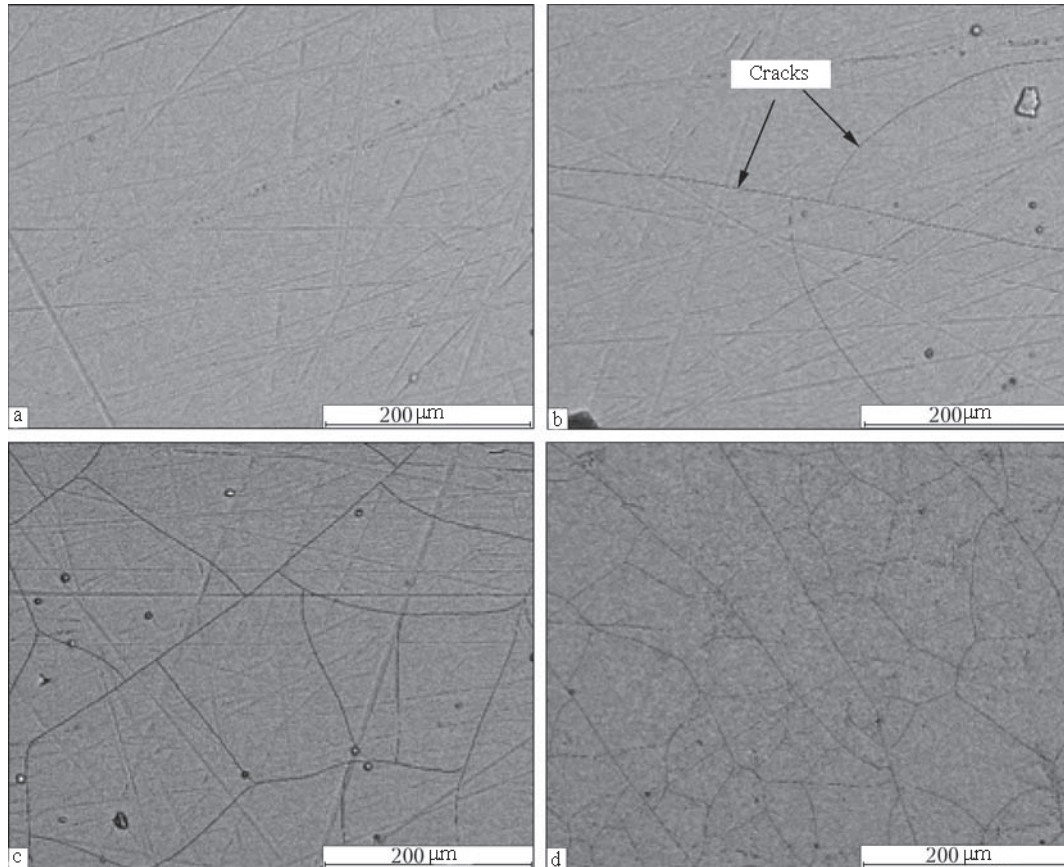
Fig. 9. Surface of the Al–Cu–Fe coating, deposited on the steel substrate (steel K110) at a temperature of 600 (*a*); 620 (*b*); 720 (*c*) and 870 K (*d*).

Table 4. Evaluation of the fracture toughness in Al–Cu–Fe coatings of different thickness

Thickness, μm	Substrate temperature T_{sc}, K	Thermal stresses σ, MPa	Fracture toughness K_{1c}, MPa m
10.0	600...620	375...400	1.57...1.68
8.5	620...650	430...465	1.67...1.79

Here T_{sc} is th temp rature at wh ch cracks ap ared in the coating during cooling; σ are the thermal stresses corresponding to T_{sc}

Al–Cu–Fe coating with a thickness of 8.5 μm are presented in Table 4. It should be mentioned that the resultant value K_{1c} is similar to the fracture toughness of thick specimens of $Al_{63}Cu_{25}Fe_{12}$ with the quasi crystalline structure ($K_{1c} = 1.64$ MPa $\sqrt{M}$) [19].

Determination of the conditions for producing defect free quasi crystalline coatings. Taking into account the resultant values of the fracture toughness of the quasi crystal-

line coatings, its coefficient of linear thermal expansion and the elasticity modulus, calculations were carried out to determine the critical values of the thickness of the coatings, deposited at temperatures from 520 to 920 K on the substrate of steels with different values of the coefficient of linear thermal expansion (Fig. 10). As indicated by the graph, the critical thickness of the coating monotonically decreases with increasing deposition temperature. Since the values of the coefficient of linear thermal expansion of the steels vary in the range from $11 \cdot 10^{-6}$ (steel K110) to $15 \cdot 10^{-6}$ (steel 30), the range of variation of the critical thickness of the coating may vary, for example, at a deposition temperature of 770 K, from 20 to 5 μm.

For the experimental verification of the method of determination of the conditions of formation of the defect free quasi-crystalline coating, analysis was made of the microstruc-
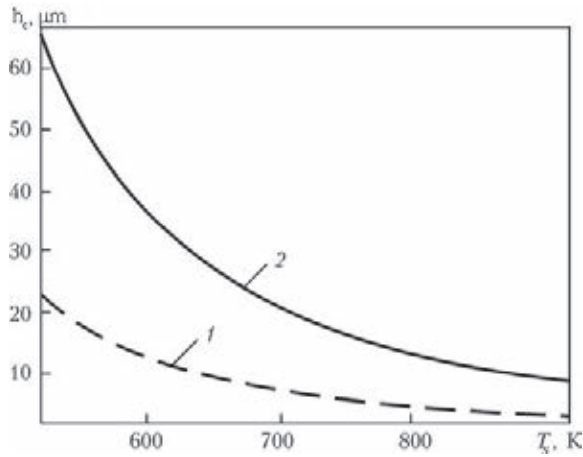
Fig. 10. Dependence of the critical thickness of the coating on the deposition temperature, calculated for the substrate with the coefficient of linear thermal expansion: 1) $\alpha_c = (12.1\pm1.3)\cdot10^{-6}$ K^{-1}, steel K110; 2) $\alpha_c = (15\pm1.3)\cdot10^{-6}$ K^{-1}, steel St30.

value, cracking did not take place.

Conclusions

1. The experimental results show that the thermal stresses provide the main contribution to the general residual macrostresses in the Al–Cu–Fe coatings, containing the quasicrystalline phase.

2. The temperature dependence of the residual stresses in the relatively thin Al–Cu–Fe coatings, where the stress relaxation as a result of Micro cracking is not extensive, shows that the coefficient of linear thermal expansion of the material of the coating can be estimated as $\alpha_c = (17.1\pm1.3)\cdot10^{-6}$ K^{-1}.

3. It was also shown that the continuous

Table 5. Comparison of the calculated value of the critical thickness of the coatings with the results of investigation of the surface

Coating	Substrate	Sublayer, μm	T_s, K	Thickness, μm	Critical thickness	Phase composition	Presence of cracks
EWI008	K600	None	910	52	19	100% *ico*	Cracks
EWI009	K600	»	890	53	20	50/50 *ico*/β	»
EWI010	K600	»	890	43	20	20/80 *ico*/β	»
EWI007	K600	»	870	9	21	20/80 *ico*/β	A very small number of cracks
EWI01 1	K600	»	870	10	21	30/70 *ico*/β	»
EWI014	K890	1.5 Ni	900	50	6	60/40 *ico*/β	Cracks
EWI020	K890	None	830	6.5	8	60/40 *ico*/β	A small number of cracks
EWI027	K110	2 Ni	790	25	8	60/40 *ico*/β	Cracks
EWI030	K110	1.5 Ni 2.5 Cu	750	31	9	60/40 *ico*/β	»
EWI031	K110	2 Cu	720	36	10	70/30 *ico*/β	»
EWI032	K110	2 Ni	720	38	10	70/30 *ico*/β	»

ture of the surfaces of the Al–Cu–Fe coatings, deposited at different temperatures on the substrate of different steels. Table 5 shows the data for the conditions of deposition of coatings, calculated values of the critical thickness, and the results of analysis of the cracks on the surface of the coatings. In all specimens at the thickness of the coating, greater than the critical value, examination showed extensive cracking on the surface, and in the thickness of the coating was smaller than the critical

cracking is the main mechanism of stress relaxation in the Al–Cu–Fe coatings. Evaluation of the critical stress concentration factor K_{1c} of the coating material showed that it's value is approximately (1.6 ± 0.1) MPa·m$^{1/2}$.

4. The experimentally determined values of the coefficient of linear thermal expansion and the critical stress intensity factor in the Al–Cu–Fe quasi crystalline coatings were used to determine the values of the critical thickness in dependence on the coefficient

of linear thermal expansion of the substrate and the deposition temperature above which continuous cracking becomes likely.

5. Analysis of the surfaces of the quasi-crystalline coatings, deposited at different temperatures on the substrate of different materials (alloy K10, steel K600, K890 and K110) shows that extensive cracking of the coating was recorded in the case in which the thickness of the coating was greater than the appropriate critical thickness.

References

1. Sordelet D. J., Dubois J. M. Quasicrystals: perspectives and potential applications, MRS Bulletin, 1997, 22, P. 34–37.
2. Sordelet D. J., Kim J.S., Besser M.F. Dry sliding of polygrained quasicrystalline and crystalline Al–Cu–Fe alloys, MRS Proceedings, 1999, 553, P. 459–470.
3. Ustinov A. I., Movchan B. A., Polishchuk S. S. Formation of nanoquasicrystalline Al–Cu–Fe coatings at electron beam physical vapour deposition, Scripta Materialia, 2004, 50, No. 4, P. 533–537.
4. Ustinov A. I., Polishchuk S. S. Peculiarities of the structure and properties of quasicrystalline Al–Cu–Fe coatings produced by Eb PVD process, Phil. Mag, 2006, 86, P. 971–977.
5. Effect of grain size on the damping capacity of quasicrystalline Al–Cu–Fe materials, A. I. Ustinov, S. S. Polishchuk, V. S. Skorodzievskii, V. V. Bliznuk, Surface and Coat. Tech, 2008, 202, P. 5812–5816.
6. Hutchinson J. W., Suo Z. Mixed mode cracking in layered materials, Advances in Applied Mechanics, 1992, 29, P. 63–191.
7. Ye T., Suo Z., Evans A. G. Thin film cracking and the roles of substrate and interface, Inter. J. Solids Structures, 1992, 29, No. 21, P. 2639–2678.
8. Residual stress in as-deposited Al–Cu–Fe–B quasicrystalline thin films / S. Polishchuk, P. Boulet, A. Mezin et al., J. Mater. Res, 2012, 27, No. 5, P. 837–844.
9. Birkholz M., Genzel C., Fewster P. Thin film analysis by X-ray scattering, Weinheim: Wiley-VCH, 2006, 356 p.
10. Cahn J. W., Shechtman D., Gratias D. Indexing of icosahedral quasiperiodic crystals, J. Mater. Res, 1986, 1, No. 1, P. 13–26.
11. Noyan C., Cohen J. B. An X-ray diffraction study of the residual stress-strain distributions in shot-peened two-phase brass, Mater. Sci. Eng, 1985, 75, P. 179–193.
12. Balasingh C., Singh A. K. Residual stresses and their measurements by X-ray diffraction methods, Metals Materials and Processes, 2000, 12, No. 2, 3, P. 269–280.
13. Beuth J. L. Cracking of thin bonded films in residual tension, Intern. J. Solids structures, 1992, 29, No. 13, P. 1657–1675.
14. Mechanical properties of quasicrystalline Al–Cu–Fe coatings with submicron-sized grains. Yu. V. Milman, D. V. Lotsko, S. Dub et al., Surface and Coating. Technology, 2007, 201, No. 12, P. 5937–5943.
15. Tanaka K., Mitarai Y., Koiwa M. Elastic constants of Albased icosahedral quasicrystals, Phil. Mag. A, 1996, 73, No. 6, P. 1715–1723.
16. Tsai A. P., Inoue A., Masumoto T. A stable quasicrystal in Al–Cu–Fe system, Jpn. J. Appl. Phys, 1987, 26, P. 1505–1507.
17. Thornton J. A., Hoffman D. W. Stress-related effects in thin films, Thin Solid Films, 1989, 171, No. 1, P. 5–31.
18. Thouless M. D., Olsson E., Gupta A. Cracking of brittle films on an elastic substrate, Acta Metallurgica et Materialia, 1992, 40, P. 1287–1292.
19. Mechanical properties of quasicrystalline and crystalline phases in Al–Cu–Fe alloys, U. Koster, W. Liu, H. Liebertz et al., J. Non-Cryst Solids, 1993, 153–154, P. 446–452.

Investigation of the functional possibilities of condensed gradient thermal barrier coatings

K.Yu. Yakovchuk[1], Yu.E. Rudoi[2], L.M. Nedorenko[1], A.V. Mikitchuk[1] and V.A. Akrymov[3]

[1]*State Enterprise 'International Centre for Electron Beam Technologies', E.O. Paton Electric Welding Institute, Kiev*
[2]*E.O. Paton Electric Welding Institute, Kiev*
[3]*State Enterprise, Scientific and Production Gas Turbine company Zarya-Mashproekt, 54018 Nikolaev*

The structure and properties of condensation thermal barrier coatings produced using the electron beam method by tradition multi-stage technology and also gradient coatings deposited according to the single-stage technology are analysed. It is shown that the thermal cyclic life in the air at 400 ↔ 1100°C of gradient thermal barrier coatings SDP-3A/AlCr/ZrO_2–8% Y_2O_3 and SDP-6/AlCr/ZrO_2–8% Y_2O_3 on the heat-resistant alloy Ch88U-VI amounts to 900...1100 one hour cycles, which 1.5...2.0 times exceeds the mean value of the life of standard two-layer coatings SDP-3A AlCr/ZrO_2–8% Y_2O_3. It is established that the thickness of the layer of scale on the basis of Al_2O_3 after 500 h of isothermal annealing in the air at 1100°C in gradient thermal barrier coatings SDP-3A/AlCr/ZrO_2–8% Y_2O_3 and SDP-6/AlCr/ZrO_2–8% Y_2O_3 is homogeneous and amounts to about 5 μm, while in standard coatings it is characterized by heterogeneity at the thickness of about 10 μm. The width of the zone depleted in aluminium in the bond layer does not exceed 5 μm. In the standard coatings the scale layer is characterized by heterogeneity at the thickness of 10 μm; the width of the depleted zone is about 15...20 μm. Ref. 13, Tables 2, Figures 8.

The currently available thermal barrier coatings, used for the protection of blades of gas turbine engines, are multilayer systems consisting of a metallic creep-resisting binding layer, deposited on the substrate (the creep resisting alloy – the blade material), and a low heat conductivity outer ceramic layer based on zirconia, partially stabilised with yttrium oxide (YPSZ). Between these layers there is a thin film of the thermally grown oxide α-Al_2O_3 (TGO), ensuring adhesion of the outer ceramic layer with the surface of the metallic-resisting binding layer.

Depending on the service conditions of the turbine (the gas flow temperature, saturation of air with dust particles or salts of seawater), the blades contain metallic creep- and/or corrosion-resisting binding layer of different composition [1–5]. In the service conditions, the chemical and phase composition is of the metallic layer and the goal extensive changes as a result of diffusion interaction with the material of the protected alloy [6].

The single-stage electron beam technology of deposition of thermal barrier gradient coatings (GC) [7] makes it possible to produce on the surface of the metallic creep-resisting binding layer additional transition zones, whose composition can differ, for example, intermetallics (NiAl, CoAl), aluminium, aluminium + chromium, etc [8, 9].

The process of production of the coating and its finishing heat treatment is accompa-

nied by the formation of the transition zone with a gradient of chemical composition at the NiCoCrAlY/YPSZ contact as a result of diffusion flows. Modification of the chemical composition of this transition zone should improve the thermomechanical compatibility of the metallic and ceramic layers, reduce the kinetics of growth of the film based on α-Al_2O_3, restriction of the diffusion of refractory elements, included in the composition of the protected creep-resisting alloy. The formation of oxides of this elements increases the thickness and disrupts the integrity of the Al_2O_3 film resulting in failure of the coating [1, 2].

In the present work, the creep resisting binding layer was represented by the following cobalt-based alloys, wt.%: SDP-6 (22…24 Cr, 11…13 Al, 8…10 Ni, 0.4… 0.6 Y), and SDP-3A (22…24 Cr, 11…13 Al, ≤2 Ni, 0.4…0.6 Y).

The aim of the present work is the comparative analysis of the possibilities of thermal barrier standard coatings (SC) with a CoCrAlY metallic binding layer and the outer ceramic YPSZ, and also the gradient coatings, produced by the single-stage technology and consisting of the metallic binding layer, the outer ceramic coating and the transition zone between them; selection of the optimum composition of the transition zone and the boundary of the creep resisting metallic binding layer CoNiCrAlY with the outer ceramic coating, ensuring the maximum durability of the thermal barrier gradient coatings as a result of the analysis of the microstructural special features of the coatings in the condition after deposition, heat treatment and subsequent thermocyclic and isothermal tests.

The additional transition layer in the gradient coating was an intermediate layer containing aluminium and aluminium with chromium.

For comparison, the single-stage process was used to produce the two-layer coating (TC) consisting of the binding layer SDP-3A or SDP-6 and the outer ceramic layer.

The gradient and two-layer coatings were deposited in electron beam equipment in a single technological cycle using the technol-ogy based on the application of a composite ingot and a carousel-type evaporator [7–9].

The thermal barrier gradient coatings were deposited on flat specimens in the form of disks of Ch88U-VI creep resisting alloy with a diameter of 24–35 mm, thickness 3...4 mm.

A metallic ingot of a creep resisting alloy based on cobalt SDP-6 or SDP-3A with a refractory pool – intermediary, formed on the surface of the ingot, was placed in a copper watercooled crucible [9], and a composite ingot based on $ZrO_2(8Y_2O_3)$ was placed in the carousel-type evaporator [8].

After preheating the specimens and the formation of the liquid pool using the electron beam the metallic creep resisting binding layer Co(Ni)CrAlY was deposited.

Subsequently, the equipment with the specimens was moved and positioned above the carousel evaporator. The second phase of the single-stage process consisted of the deposition of the gradient transition zone and the outer ceramic layer.

After depositing the gradient coatings, all the specimens were annealed in vacuum at a temperature of 1100°C, a pressure of $1\cdot10^{-3}$ Pa for 60 min.

The thermal barrier standard coatings (without the gradient transition zone) were produced by the traditional electron beam technology by consecutive operations, including the deposition of the metallic creep-resisting layer on the specimens, their vacuum heater treatment, hardening shot blasting treatment of the surface of the specimens with microspheres, repeated heat treatment, surface treatment of the metallic layer with blowing of corundum [10], and the deposition of the outer ceramic layer followed by heat treatment [6]. The standard coatings were produced at the Zarya-Mashproekt company.

The chemical composition of the investigated coatings, produced by the transitional multistage technology, and also of the gradient and two-layer coatings (single-stage process) is as follows overleaf.

The thickness of the individual layers of the coating was determined using a PolivarMet optical microscope. The microstructure was

Coating variant	Composition of the coating
SC	
SC-1	ChS-88/SDP-3A/8YSZ
SC-2	ChS-88/SDP-3A/8YSZ
SC-3	ChS-88/SDP-3A/8YSZ
SC-4	ChS-88/SDP-3A/8YSZ
SC-5	ChS-88/SDP-3A/8YSZ
TC	
TC-1	ChS-88/SDP-6/8YSZ
TC-2	ChS-88/SDP-3A/8YSZ
GC	
GC-2	ChS-88/SDP-6/100 Al/8YSZ
GC-3	ChS-88/SDP-6/50Al 50Cr/8YSZ
GC-4	ChS-88/SDP-6/60Al 40Cr/8YSZ
GC-6	ChS-88/SDP-3A/75Al 25Cr/8YSZ
GC-7	ChS-88/SDP-3A/60Al 40Cr/8YSZ

Fig. 1. Microstructure of the cross-section of thermal barrier coatings on the Ch-88 substrate in the condition prior to testing the standard coating SC STP 3A/AlCr/ZrO$_2$–8% Y$_2$O$_3$ (*a*) and the gradient coating (*b*).

investigated and microhardness of the standard coatings and gradient coatings determined on the specimens in the condition after heat treatment and thermal cycling.

Microhardness was measured on the cross sections of the coatings using attachment Micro-Duromat 4000E to the PolivarMet optical microscope by the standard Vickers indentor at a load of 50 N with a fixed loading rate and holding time under load.

The structure of the thermal barrier coatings was investigated in a Tescan Vega 3 scanning electron microscope, the chemical composition was determined by x-ray spectrum microanalysis using the energy-dispersing attachment INCA 200 to the CamScan 4D scanning electron microscope.

The thermocyclic tests were carried out in air with the holding time 1a/cycle 400 1100 °C, cycle duration 1 hour.

The thermal stability of the coatings was investigated in isothermal annealing of the specimens at a temperature of 1100 °C for 500 h and analysis of the microstructure at the interphase boundary every 100 hours.

Structure and properties of the specimens with the standard coating. The microstructure of the standard coating in the specimens in the as-received condition and after thermal cycling

to the shown in Fig. 1, 2. In the initial condition, the structure of the SDP-3A metallic creep-resisting layer consists of the oriented crystals, elongated in the direction of incidence of the vapour flow. A thin interlayer of TGO (less than 0.2 μm) forms at the boundary between the metallic and ceramic layers (Fig. 2*a*).

Table 1 shows the values of the thickness of the individual layers of the coating after heat treatment and microhardness, heat treatment and thermal cycling (in the ceramic layer). The ceramic layer YPSZ has a columnar structure with slight porosity.

The distribution of the main elements at the binding layer/ceramic layer interface in the specimens in the initial condition and after thermal cycling is shown in Fig. 2 *c*, *d*.

In the process of thermal cycling, the elements of the SDP-3A metallic layer (aluminium, nickel, cobalt) and also the elements of the protected substrate (tungsten, molybdenum, titanium) diffuse to the TGO/YPSZ interface (Fig. 2*d*), concentrate in the zone
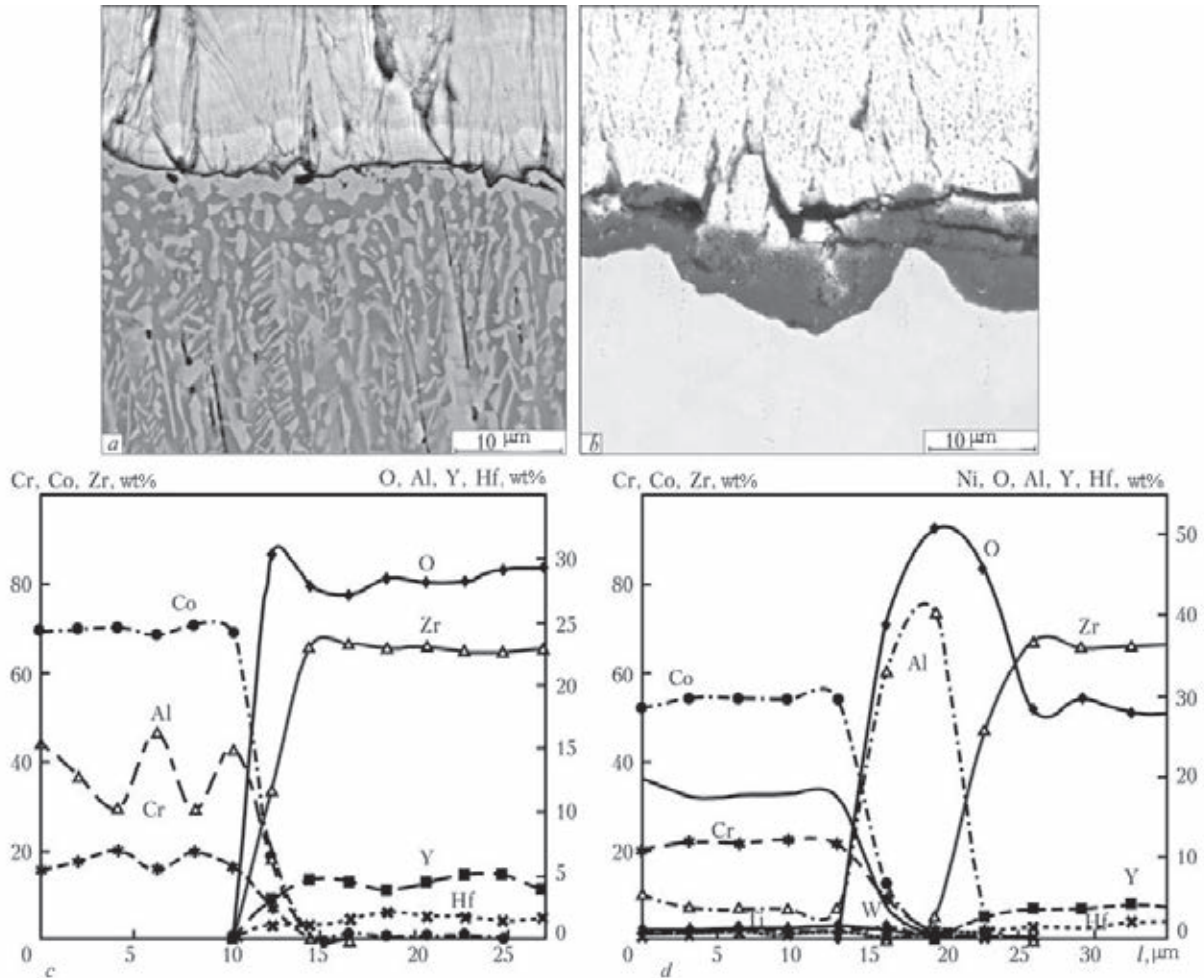
Fig. 2. Microstructure and the distribution of the main elements in the cross-section of the thermal barrier standard coating STP-3 in the initial condition (*a*, *c*) and after thermal cycling (*b*, *d*); *l* is the length of distribution of the main elements.

Table 1. Values of the thickness and microhardness of the individual layers of the coating after heat treatment and thermal cycling

Layer	SC		GC	
δ, μm	δ, μm	HV, MPa	δ, μm	HV, MPa
Binding SDP-3A, SDP-6	80...140	5	90...120	4.4
Intermediate	–	–	25...30	4.9
Ceramics (after thermal cycling)	70...110	2.8...3.2	70...130	3.5...3.8
		(4.5...5.4)		(5.6...7.2)

below the TGO layer causing premature failure of the coating is a result of propagation of cracks along this zone. The TGO layer is characterised by heterogeneity with simultaneous formation of large cracks throughout the entire thickness of the ceramics (Fig. 2*b*).

Structure and properties of specimens with the thermal barrier gradient coating. The typical microstructure of the cross-section

of the gradient coating on the Ch-88 in the heat-treated condition is shown in Fig. 1b. The structure of the layers, forming the coating, in the vicinity of the binding layer/ceramic coating interface in the specimens of different composition after vacuum heat treatment (prior to the test) and after thermal cycling is shown in Fig. 2.

Examples are shown of the curves of the
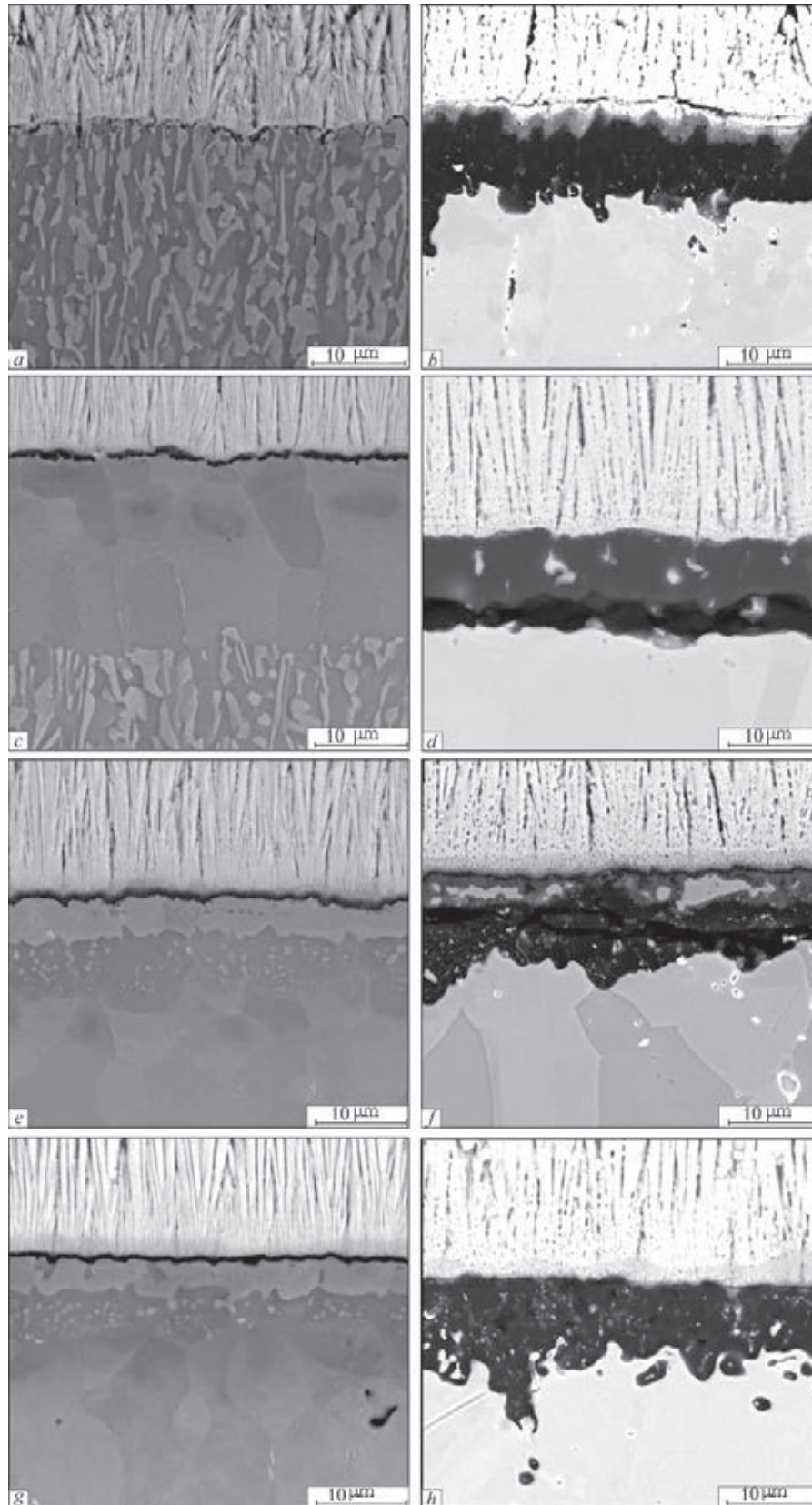
Fig. 3. Microstructures in the condition after heat treatment of the thermal barrier TC-1 (*a*), GC-2 (*c*), GC-4 (*e*), GC-7 (*g*) coatings and after thermal cycling of gradient coatings GC-1 (*b*) GC-2 (sD), GC-4 (*f*) and GC-7 (*h*).
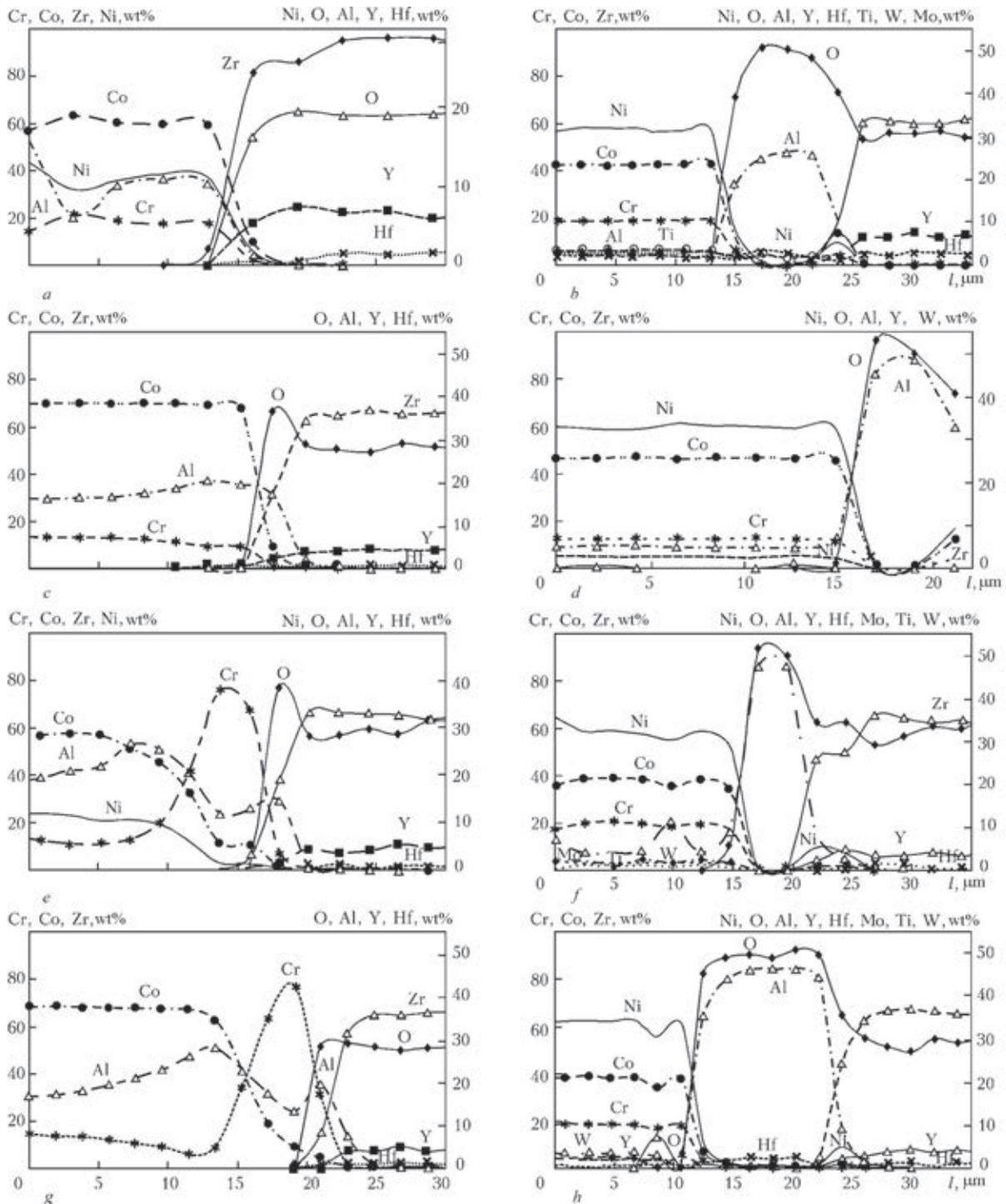
Fig. 4. Distribution of the main elements in the cross-section of the gradient thermal barrier coatings TC-1 (*a*), GC-2 (*c*), GC-4 (*e*), GC-7 (*g*) and after thermal cycling GC-1 (*b*), GC-2 (*d*), GC-4 (*f*) and GC-4 (*h*) in the condition after heat treatment.

distribution of the main elements after heat treatment and thermal cycling for the coating without the transition zone on the metallic creep resisting binding layer SDP-6, produced in the single-stage process (Fig. 4*a*, *b*) and the gradient coating with the metallic creep-resisting binding layer SDP-6 (Fig. 4*c*–*f*) and SDP-3 (Fig. 4*g*–*h*).

K.Yu. Yakovchuk, Yu.E. Rudoi, L.M. Nedorenko, A.V. Mikitchuk and V.A. Akrymov

Table 2. Chemical composition of the metal of the transition zone of the coating after vacuum heat treatment, wt.%

Coating variant	Coating composition	Al	Cr	Co	Ni
GC-1	SDP-6/8YSZ	11.4	17.8	58.9	11.0
TC-2	SDP-6/100Al/ 8YSZ	19.7	9.8	68.1	
GC-3	SDP-6/50Al50Cr/8YSZ	7.0	48.6	38.5	3.3
GC-4	SDP-6/60Al40Cr/8YSZ	11.7	75.9	11.0	1.4
TC-5	SDP-3A/8YSZ	5.0	18.9	76.1	–
GC-6	SDP-3A/75Al25Cr/8YSZ	25.7	35.4	38.8	–
GC-7	SDP-3A/60Al40Cr/8YSZ	13.2	77.8	9.0	–

The chemical composition of the transition zone of the coating (at the Me/TGO interface) after vacuum heat treatment is presented in Table 2.

The first metallic creep-resisting binding layer (SDP-3A or SDP-6) is characterised by the columnar directional structure with the size of the single crystal in the initial condition of approximately 4…6 μm, and approximately 8 μm after vacuum annealing. In some cases, after condensation, the upper zone of the SDP layer contained intercrystalline pores, removed after subsequent heat treatment.

The transition zone between the layer of the SDP and the ceramic has a multi-phase structure; the ceramic layer is characterised by the uniform columnar structure.

Analysis of the microstructure and the distribution of the chemical elements shows that the durability of the coating is strongly affected by the inter-related parameters – the composition of the transition zone and the deposition temperature of the ceramic layer.

Adhesion and heat resistance of the thermal barrier coating depend on the characteristics of the interfacial surface with which it is bonded. The interfacial surface for the outer ceramic layer is the thin-film of Al_2O_3 formed on the surface of the metallic creep-resisting binding layer (either prior to the position of the ceramic layer or in the process of subsequent heat treatment). The experimental results show that the phase transformation of Al_2O_3 (γ-Al_2O_3 to α-Al_2O_3) in the process of thermal cycling reduces the durability of the coating [10]. Therefore, the formation of the stable film of Al_2O_3 is very important.

In the specimens without the transition zone, produced by the single stage process SDP-3A/8YSZ (TC-5) and SDP-6/8YSZ (TC-1) the Al_2O_3 layer does not form in the initial condition; after vacuum heat treatment of the structure shows a thin (approximately 0.2 μm) intermittent layer of TGO (Fig. 3a). In the gradient coating with the transition layer of aluminium (GP-2) the layer of Al_2O_3 after heat treatment is more distinctive (Fig. 3c). The boundary with the SDP-6 is characterised by the formation of a transition zone with a higher aluminium content. In the presence of a thin intermittent layer of TGO the contact area between the metallic creep-resisting binding layer and the ceramic layer is considerably smaller than in the specimens with the relatively dense film of Al_2O_3 bordering with the ceramic layer [11]. In the presence in the transition zone of the gradient coating of aluminium in chromium vacuum heater treatment is accompanied by the formation of a relatively dense layer of Al_2O_3 with a thickness of approximately 1 μm. In the specimens with a thin film of TGO (or in the absence of the film) heat treatment results in the formation of the boundary with the ceramic layer of an interlayer enriched with chromium nickel which in the course of further thermal cycling may show cracking of the coating.

The deposition temperature of the ceramics is also important. If this temperature is higher than the optimum temperature, chromium and aluminium diffuse into the ceramic layer; the composition of the resultant TGO layer also
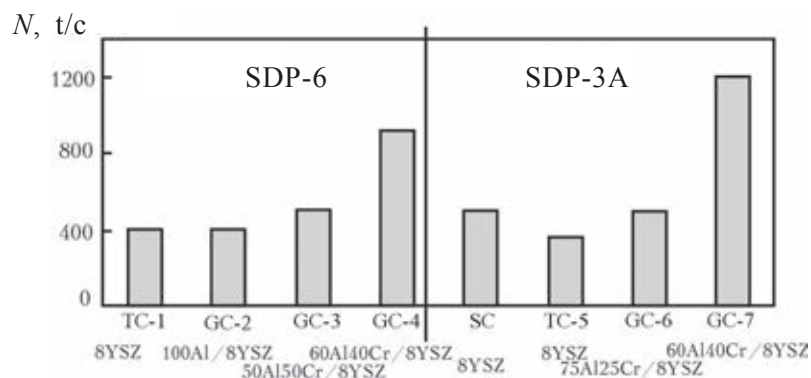
Fig. 5. GC = GP Thermocyclic durability of the specimens with the standard and gradient coatings; Nt/c is the number of thermal cycles.

contains cobalt, chromium and nickel accelerating the failure of the layer during thermal cycling. When the evaporation temperature is reduced by 50°C, the composition of TGO after failure (in accordance with the results of chemical analysis) shows that there is no diffusion of the chemical elements. The formation of metal oxides increases the thickness and disrupts the continuity of the Al_2O_3 film [12, 13]. Another important parameter is the presence in the transition zone of approximately 70 wt.% of chromium generating an effective barrier preventing the diffusion of the elements of the metallic creep resisting binding layer, the substrate material and also delaying the growth of the aluminium oxide layer.

The results of thermal cyclic tests of the thermal barrier standard and gradient coatings were generalised in the histogram (Fig. 5). The highest level of durability was recorded for the gradient thermal barrier coatings GP (GP-7 and GP-4) in which the composition of the transition zone is optimum.

Evaluation of the thermal stability of samples. The main changes in the structure are associated with the growth of the oxide layer of Al_2O_3 separating the outer ceramic binding layer's taking place as a result of the oxidation of the surface of the metallic binding layer.

In the specimens with the standard and gradient coatings in the initial condition the thickness of the Al_2O_3 was approximately 0.2 and 1.0 micrometres respectively (Fig. 2a; Fig. 3a, c, e, g). It is important to mention the high heterogeneity of the TGO layer of the standard specimens in the initial condition.

After annealing for 500 hours the TGO layer on the standard specimens was characterised by high heterogeneity in the thickness of the layer which in some areas exceeded 9 μm (Fig. 6a, c, d). In the specimens with the gradient coating, the layer of Al_2O_3 was relatively homogeneous and its mean thickness was approximately 5 μm (Fig. 6b, d, e, f).

The large difference was observed in the concentration of aluminium and the binding layer/aluminium oxide interface. In the specimens with the gradient coating the aluminium content in the metallic layer in the condition after vacuum annealing was approximately 11…15 wt.%, after holding for 500 hours approximately 11…12 wt.%. In the specimens with the standard coating the aluminium concentration in this zone decreased from approximately 15 wt.% in the condition after supply to approximately 4 wt.% after 500 hours of annealing, i.e. the amount of aluminium, required for ensuring the creep resistance of the metallic binding layer, was almost completely exhausted.

In the specimens with the standard coating after long-term annealing the thickness of the aluminium-depleted zone in the SDP layer, adjacent to the TGO layer, was approximately 15...20 μm (Fig. 6d). The thickness of this zone in the gradient coating with the metallic creep resisting binding layer SDP-3a did not exceed 5 μm (Fig. 6f).

Changes in the structure of the outer ceramic layer in the process of annealing the specimens with the standard and gradient coatings are
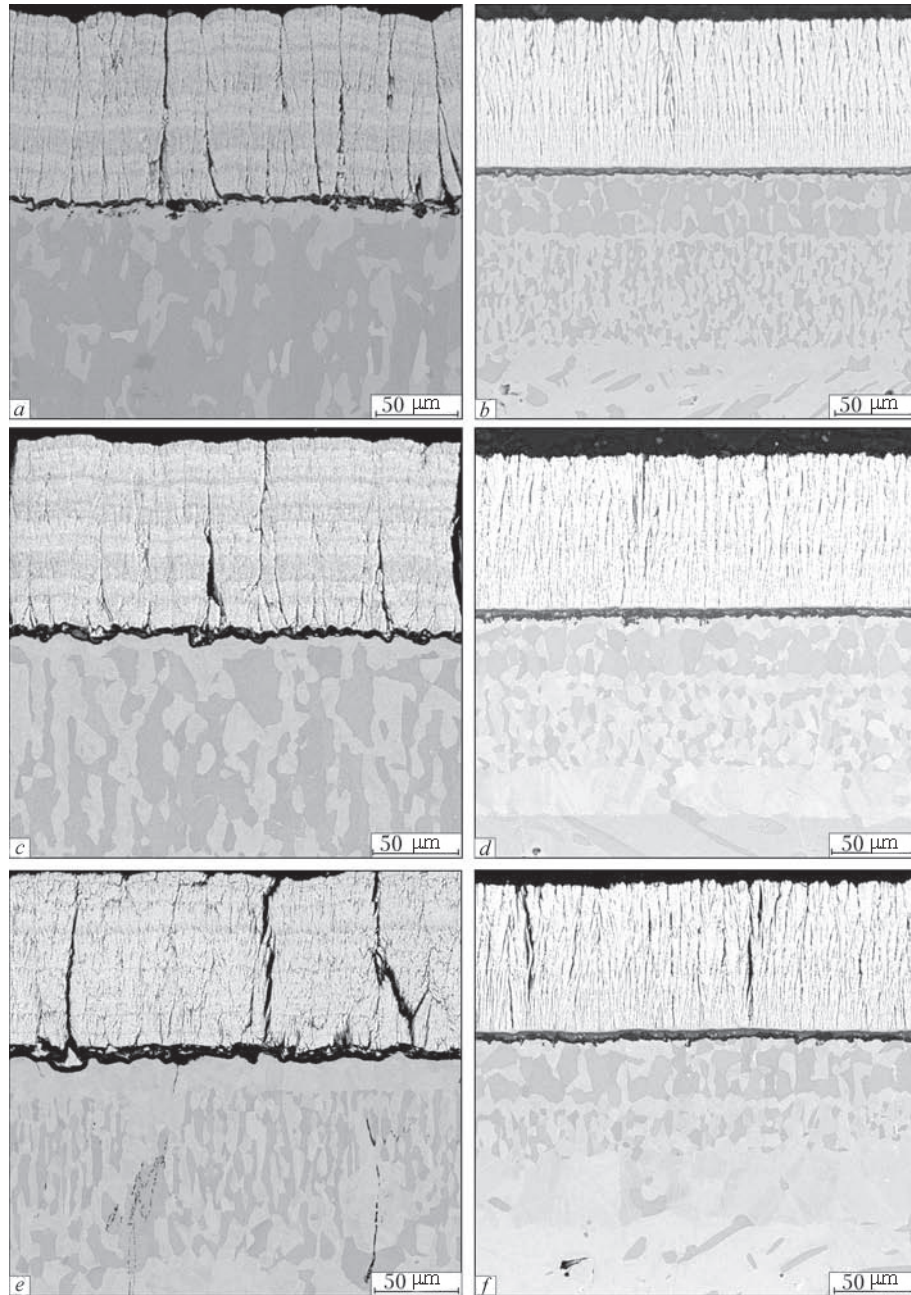
Fig. 6. Microstructures of the cross-section of the coating on the SDP-3A after annealing at 1100 °C for 100, 300 and 500 hours; *a*, *c*, *e*) standard coating; *b*, *d*, *f*) the gradient coating.

shown in Fig. 6. The results of measurements of the microhardness of the ceramic layer in the centre of the ceramic layer are presented in Fig. 7. The ceramic layer in the specimens with the standard layer is characterised by higher porosity in comparison with the gradient coating, and sintering and cracking of ceramics takes place after annealing for 400 hours. After annealing for 500 hours the level

of microhardness of the coatings of both types was approximately the same.

Sintering of the ceramic coating causes cracking and fragmentation of the coating. Figure 8 shows the microstructure of the surface of the ceramic layer of the standard and gradient coatings after annealing for 300 hours. Fragmentation of the ceramic layer of the standard coating is more extensive
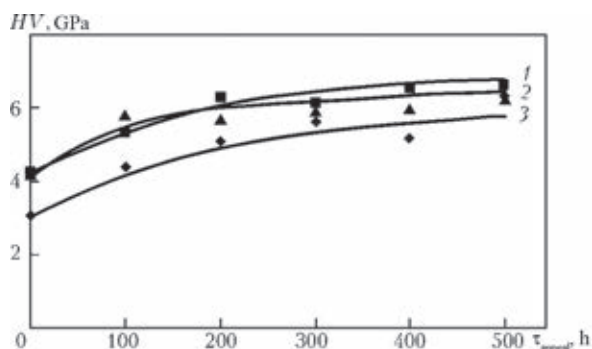
Fig. 7. Microhardness of the ceramic layer in the centre of the ceramic coating: *1*) the gradient coating with the binding layer SDP-6; *2*) the gradient coating with the SDP-3A binding layer; *3*) the standard layer with the binding layer SDP-3A.

and the mean size of the fragments reaches approximately 0.2×0.2 mm, and that of the gradient coating 0.5×1.0 mm.

Conclusions

1. The experimental results show that the durability of the thermal barrier gradient coatings SDP3A/AlCr/ZrO_2–8% Y_2O_3 and SDP6/AlCr/ZrO_2–8% Y_2O_3 on the creep-resisting alloy Ch88U-VI in air in cyclic oxidation in the conditions 400 ↔ 1100 °C is 900…1100 °C are cycles, which is 1.5–2.0 times greater than the mean value of the durability of the standard two-phase coatings TC SDP 3A/ZrO_2–8% Y_2O_3.

2. It has also been shown that in the thermal barrier gradient coatings SDP 3A/AlCr/ZrO_2–8% Y_2O_3 and SDP 6/AlCr/ZrO_2–8% Y_2O_3, produced by evaporation of the composite ingot, after heat treatment in vacuum at 1100 °C for one hour the interphase between the metallic creep resisting binding layer and the ceramic layer is characterised by the formation of the oxide film TGO based on Al_2O_3 with a thickness of approximately 1 μm. The thickness of the oxide layer in the standard coatings SDP 3A/ZrO_2–8% Y_2O_3 is approximately 0.2 μm.

3. It has also been established that after isothermal annealing in vacuum at 1100 °C for 500 hours, the thickness of the TGO layer based on –αAl_2O_3 in the thermal barrier coatings SDP 3A/AlCr/ZrO_2–8% Y_2O_3 and SDP 6/AlCr/ZrO_2–8% Y_2O_3 is homogeneous and equals approximately 5 μm, and in the standard coatings, the scale layer is characterised by a heterogeneity at a thickness of approximately 10 μm. The mass fraction of aluminium in the standard coating at the metallic creep resisting binding layer/Al_2O_3 interphase decreases to 4%, in the gradient coating it is retained on the initial level (approximately 12%) ensuring long-term service of the latter.

4. The degree of fragmentation of the

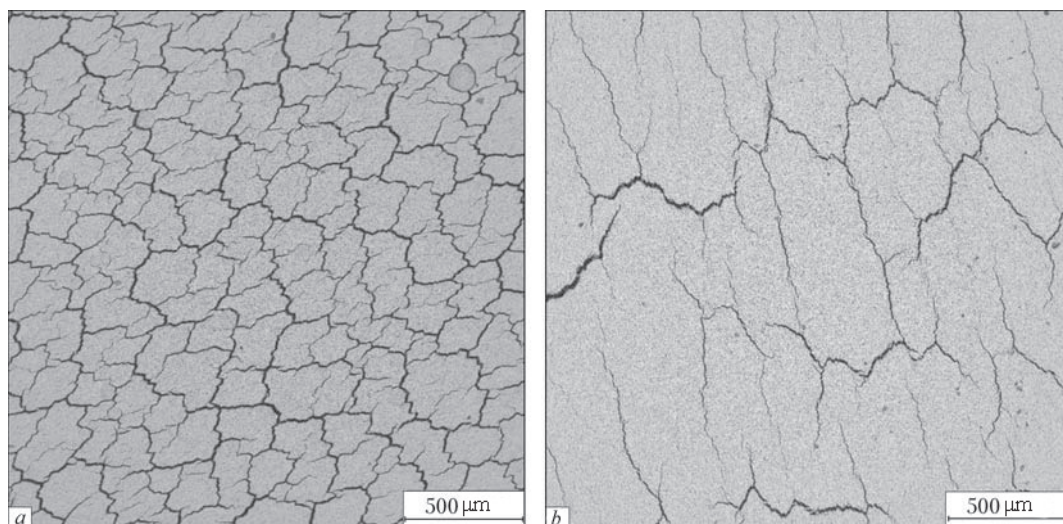**Fig. 8.** Microstructure of the ceramic surface of the coating after annealing for 300 hours at 1100 °C: *a*) SC standard coating with the SDP-3A binding layer; *b*) the gradient coating with the SDP-3A binding layer.

surface layer of the ceramics in the standard coating is quite high. The mean size of the fragments is 0.2×0.2 mm in comparison with 0.5×1.0 mm in the gradient coating.

References

1. Levi C. G. Emerging materials and processes for thermal barrier systems, Curr. Opin. Sol. State Mater. Sci, 2004, 8, P. 77–91.
2. Mechanisms controlling the durability of thermal barrier coatings, A. G. Evans, D. R. Mumm, J. W. Hutchinson et al., Prog. Mater. Sci, 2001, No. 46, P. 505–553.
3. Budinovskii S.A., et al., Aviats. Prom., 2008, No. 4, 33–37.
4. Cyclic oxidation behavior of an EB-PVD CoCrAlY coating influenced by substrate/coating interdiffusion, T. Liang, H. Guo, H. Peng, S. Gong, Chin. J. Aeronaut, 2012, 25, P. 796–803.
5. Liang T., Guo H., Peng H. Precipitation phases in the nickel-based superalloy DZ125 with YSZ/CoCrAlY thermal barrier coating, J. Alloy Comp, 2011, 509, P. 8542–8548.
6. Madashenko I.S., et al., Probl. SPets. Elektrometall., 2000, No. 1, 23–34.
7. Pat. 6.669.989 B2 USA, MPK C 23 C 16/00. Method for producing by evaporation a functionally graded coating with an a outer ceramic layer on a metal substrate, B.A. Movchan, L.M. Nerodenko, Yu.E. Rudoy, Publ. 30.12.2003.
8. Yakovchuk K. Yu., Rudoi Yu.E., Sovremen. Elektrometallurgiya, 2003, No. 2, 10–16.
9. Movchan B. A., Yakovchuk K. Yu. Graded thermal barrier coatings, deposited by EB-PVD, Surf. Coat. Technol, 2004, 188–189, P. 85–92.
10. Author's Cert. 1827397, MPK S 23 C 14/00, Rybnikov A. I., et al., 7.11.1993, Bull. No. 26.
11. Schaeffer J.S. The effect of alumina phase transformation of thermal barrier coating durability, Proc. of TBC Interagency Coordination Committee, 1997, P. 99–108.
12. Influence of electron beam physical vapor deposited thermal barrier coating microstructure on thermal cyclic oxidation conditions, C. Leyens, V. Schultz, B. A. Pint et al., Surf. Coat. Technol, 1992, 120–121, P. 68–76.
13. Influence of high-temperature creep stress on growth of thermally grown oxide in thermal barrier coatings / D. Seo, K. Ogawa, Y. Nakao et al., Surf. Coat. Technol, 2009, 203, P. 1979–1983.

Submitted 21.10.2013

Plasma-arc remelting of billets compacted from shavings of austenitic stainless steels

V.R. Burnashev, V.A. Shapovalov, D.M. Zhirov, V.G. Kozhemyakin and D.V. Botvinko

E.O. Paton Electric Welding Institute, Kiev

Technological peculiarities of plasma-arc remelting of billets, compacted from chips of austenitic stainless steels of Cr18Ni10Ti type, are determined. To remelt the 100 mm diameter billets, round moulds of 125 mm diameter and rectangular moulds with 125 mm wall were selected. Optimum conditions of remelting of billets were established under conditions of plasma-arc remelting in a UPP-3 furnace. It was found that to produce high-quality ingots, it is necessary to wash away the lubrication-cooling fluids from chips of austenitic stainless steels before compacting. Based on metallographic examination, it is necessary to protect the zone of compacting by argon to reduce the nitrogen content in finished metal. To decrease the amount of non-metallic inclusions and to improve the quality of the ingot surface, the remelting of billets should be performed at speeds of no more than 2...4 mm/min. Ref. 8, Tables 2, Figures 6.

The plasma heat source, characterised by a high energy potential, is used for remelting the granulated charge, melt separately the charge and shape the billet, refine liquid metal, produced at the atmospheric pressure, carry out nitriding, etc. The methods of plasma arc remelting and refining of liquid metal, used widely at the present time, can be divided into two groups, with the first group including the methods of remelting in copper or ceramic crucibles and discharge into the moulds or ingot moulds; the second group – the methods of remelting granulated or packed charges, droplet remelting of the billet in a water-cooled solidification mould or a crucible, which is an intermediate container, followed by crystallisation in a water-cooled solidification mould. In all the processes of the second group, one of the main elements of the technology, ensuring the production of high-quality metal, is the solidification of metal in the water-cooled solidification mould, i.e., these processes are secondary refining remelting processes [1–4].

It should be mentioned that the remelting of the loose charge (granules, shavings, powders) does not pass through the droplet transfer stage. Although in some variants of the process, in particular, the application of the intermediate container, this process fully corresponds to secondary refining remelting. However, all these measures increase the complexity of the design of the equipment and reduce the energy parameters of the remelting process, and also increase the degree of burnout of the metal. The E.O. Paton Electric Welding Institute, Kiev, have developed a method of compacting long billets from shavings and loose materials followed by remelting by electroslag (ESR) and plasma arc (PAR) remelting [5], where the billets are represented by the electrodes compacted under

Fig. 1. A billet, compacted from shavings of austenitic stainless steels.

current from shavings of EP609Sh steel [6].

This study is a continuation of the investigations carried out both in the area of expanding the composition range of the process materials and improvement of the technological conditions of the developed method. The investigations were carried out under blanks (billets) compacted under current from shavings of austenitic stainless steels of the Cr18Ni10Ti type (Fig. 1). A special feature of the produced billets is that the shavings of the austenitic steels were not washed prior to compacting to remove lubrication and cooling liquids. In the plasma arc remelting of the billets, the metal passes through the stage of refining in the liquid film on the melted end of the billet, from the surface of the separated droplet and the surface of the liquid pool in the solidification mould. Therefore, the main part of the lubrication and cooling liquids is removed in the process of compacting and current and it should be expected that the remaining part sublimates in the process of plasma-arc remelting.

Experiments with the remelting of the compacted billets were carried out in a UPP-3 plasma arc furnace consisting of a unit with a power of 160 kW, fitted with 4 plasma generators (plasmatrons) PDM-7, designed the Design Bureau of the E.O. Paton Electric Welding Institute, Kiev. The maximum length of the remelted billet was 700 mm, weight 50 kg.

The diagram of the furnace is shown in Fig. 2. An auxiliary head, suspended from the feed mechanism, was welded to the compacted blank with a diameter 100 mm. The furnace was evacuated to 0.3 kPa and filled with argon to a pressure of 0.1…0.2 MPa.

In [7] it was established that the increase of the total flow rate of the plasma forming gas (argon) from 50 to 90 l/min reduces the heat losses in the plasmatrons from 16 to
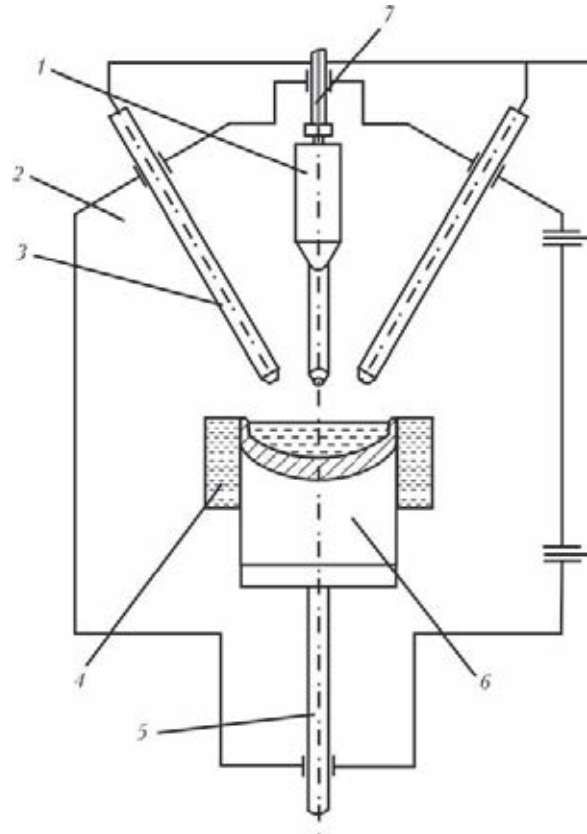
Fig. 2. Diagram of the UPP-3 plasma arc furnace: *1)* billet; *2)* chamber; *3)* plasma generator (plasmatron); *4)* solidification mould; *5)* the mechanism for withdrawal of the ingot; *6)* the ingot; *7)* the billet feed mechanism.

11%, and in the chamber of equipment from 40 to 35%, and increases the efficiency of the process from 43 to 52%. The increase of the flow rate of the plasma forming gas results in the contraction of the arcs as a result of cooling of the peripheral zone of the plasma column that reducing the magnetic interaction of the plasma arcs and the deflection of the arcs from the axis of the plasmatron. Consequently, the fraction of the heat, lost in the plasmatrons and the chamber of equipment decreases and the amount of heat, transferred to the metal increases. Thus, the flow rate of the plasma forming gas was maintained in the optimum range.

Subsequently, the plasmatrons were activated and the billet was supplied into the zone of the effect of the plasma arcs, the metal starts to drip into the solidification mould were it solidifies in the so-called dovetail

Fig. 3. Variation of the gas content C_{gas} in the furnace atmosphere in the plasma remelting of billets: 1) hydrogen; 2) oxygen.

form. After filling the solidification mould with a metal, the withdrawal mechanism is activated. The billet is withdrawn at a rate of 8…10 mm/min. The current during melting was maintained at 300…400 A, voltage was 40…50 V. During remelting of the blank, the gas phase of the furnace was inspected by c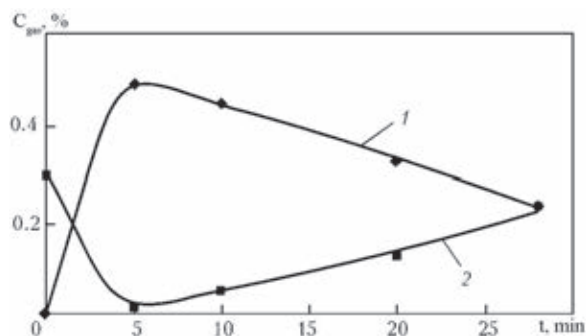hromatographic analysis using Gazokhrom 3101 equipment. Samples were taken from a nozzle in the upper part of the equipment [8].

As indicated by Fig. 3, in the first minutes of remelting the concentration of hydrogen rapidly increases and the mass fraction of oxygen decreases. Evidently, in operation of the plasmatron as a result of heating of the melting space, moisture is evaporated from the walls of the chamber and equipment. Falling into the combustion zone of the arcs and the heated metal, the moisture dissociates into hydrogen and oxygen. Consequently, hydrogen and builds up in the chamber, and oxygen oxidises part of the metal.

During further stages of remelting the oxygen content of the gas phase starts to increase. This may be explained by the dissociation of the metal oxides in the arc spot. The reduction of the mass fraction of hydrogen is caused by the washing of the chamber with argon used as the plasma forming gas.

In compaction of the consumable electrode and the current, the material was in the form of shavings from which the cooling and lubrication liquids were not removed. However, the composition of the gas phase did not show the presence of carbon monoxide

and dioxide and this indicates the removal of the carbon containing components of the lubrication cooling liquids during heating in the compacting process.

Solidification moulds of two types were used to obtain the final product in plasma arc remelting: with a circular cross-section with a diameter 120 mm, and with a square cross-section with the side 125 mm long. This size of the solidification mould was selected in accordance with the studies [1, 3] because the ratio of the diameters of the billet and the ingot should not exceed 0.7…0.8 at a remelting rate of 2.5…15.0 mm/min.

Two types of ingots with the circular and square cross-section were produced in the experiments (Fig. 4) and used to produce longitudinal and transverse templates. The samples were used for metallographic studies and the determination of the mechanical properties and chemical composition.

Determination of the chemical composition showed that in the process of plasma arc remelting all the alloying elements were in the range, permitted by the GOST 977–98 standards, including titanium and carbon (Table 1). Comparison of the results of chemical analysis of the metal, produced in plasma arc remelting, showed a higher content of nitrogen in metal (Table 1). Evidently, nitrogen saturation takes place in this stage of compacting of the billet in the open atmosphere. To reduce the nitrogen content in the metal of the billet, it is necessary to protect the zone of heating and compacting with argon.

The mechanical properties of the metal, produced by remelting the electrodes, compacted from the shavings, are presented in Table 2 which shows that the mechanical properties of the metal are not lower than the requirements of GOST 977–98 and in certain parameters they are even higher.

The transverse templates were machined to produce macrosections with a diameter of 125 mm and the square sections with the side 125 mm long, shown in Fig. 5a, b. The transverse templates show that the metal is dense, with no defects, but the longitudinal samples of the billet (Fig. 5c) shows single
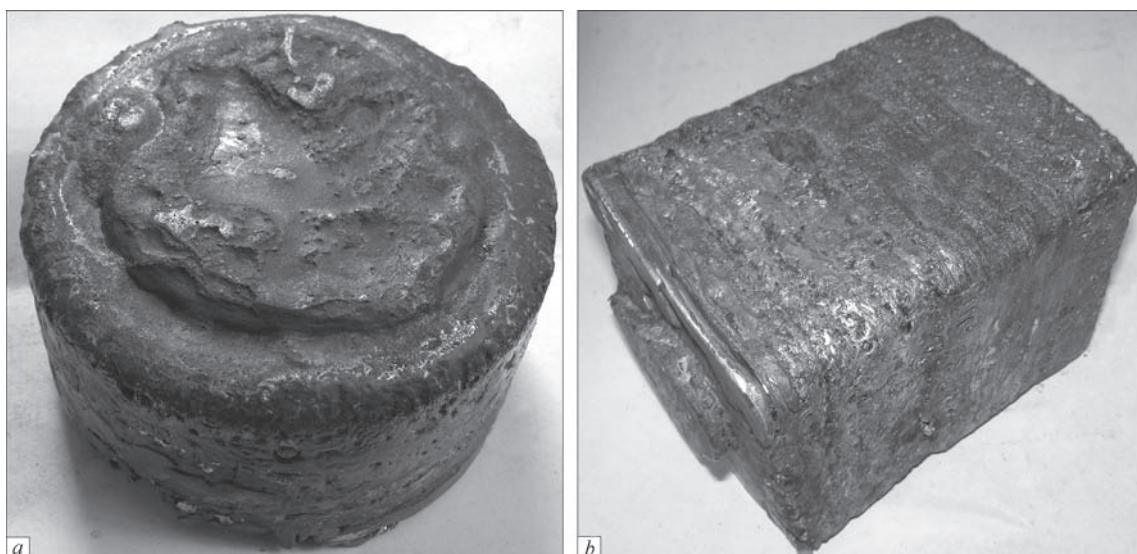
Fig. 4. Ingots with the circular (*a*) and square (*b*) sections, produced by plasma arc remelting.

Table 1. Chemical composition of austenitic steel melted by different methods

Melting method	Mass fraction of elements, %						Gas content, wt%		
	Ni	Cr	Ti	Si	Mn	C	[O]	[N]	[H]
ESR, Ø175 мм	10.0	17.0	0.3	0.67	1.3	0.11...0.13	0.016	0.049	0.0003
PAR, Ø125 мм	10.5	18.4	0.6	0.63	1.3	0.11	0.075	0.052	0.0005
PAR square 125 мм	10.5	18.4	0.6	0.63	1.3	0.12	0.022	0.055	0.0005
GOST 97798	8...11	17...20	≥5C	0.2...1.0	1.0...2.0	<0.12	–	–	–

Table 2. Mechanical properties of Cr18Ni10Ti steel, melted by different methods

Melting method	$\sigma_{0.2}$, MPa	$\sigma_{в}$, MPa	δ, %	KCV, J/cm^2	φ, %
ESR, Ø175 мм	220.0	468	50	173	60.5
PAE, Ø125 мм	242.0	475	48	245	76.0
PAR, square 125 мм	215.5	513	60	330	69.5
GOST 97798	196.0	441	25	59	32.0

large slag inclusions with a diameter of 5...7 mm. Evidently, this takes place as a result of compacting of the unwashed shavings resulting in the formation in the billet of the slag phase which does not rise to the surface at the high remelting rates and is trapped in the body of the billet. After remelting, a slag skin forms on the surface of the billet. The thickness of the skin on the side surfaces reaches 1 mm, and at the top and of the billet 10 mm (Fig. 6) which interferes with the formation of the flat surface of the billet. Consequently, to produce billets of higher quality by plasma arc remelting, the shavings of the austenitic stainless steels should be washed prior to compacting to remove the lubrication and cooling liquids and the rate of withdrawal of the billet in the remelting should be reduced to 2…4 mm/min.

In conclusion, it should be mentioned that in the remelting of the billets, compacted from the shavings of the austenitic steels, taking into account the results of chemical analysis and the mechanical properties, it is possible to produce billets for further application in the industry.

Taking into account the results of mechanical studies to improve the quality of the billets it is necessary to wash the shavings prior to compacting, protect the compacting zone with argon and reduce the remelting rate of the billets.

References

1. Lakomskii V.I., Plasma-arc remelting, edited by B Paton, Tekhnika, Kiev.
2. Erokhin A.A., Plasma arc remelting of metals and alloys. Physical and chemical processes, Nauka, Moscow, 1978.
3. Klyuev M.M., Plasma arc remelting, Metallurgiya, Moscow, 1980.
4. Dembovsky V., Plasma metallurgy (translated from Czech), Metallurgiya, Moscow, 1981.
5. Patent 7997, Ukraine MPK S 22 V 1/24, a method of compacting metallic charge, Paton B.E., et al., 10.8.2007, Bull. No. 12.
6. Shapovalov V.A., Sovremen. Elektrometallurgiya, 2011, No. 3, 21–23.
7. Granovskii V.K., Investigation of the physical-chemical processes and development of the technology of plasma arc skull melting of high nitrogen steels and alloys, dissertation, Kiev, 1982.
8. Shapovalov V.A., et al., Sovremen. Elektrometallurgiya, 2012, No. 2, 45–46.

Fig. 5. Macrosections of the transverse circular (*a*), square (*b*) and longitudinal (*c*) templates.

Fig. 6. Slag on the surface of the ingot.

Technological special features of a high-chromium nickel alloy,c omplek y alloyed with rhenium and tantalum

I.I. Maksyuta[1], O.V. Klyass[2], Yu.G. Kvasnitskaya[1], G.F. Myal'nitsa[2] and E.V. Mikhnyan[1]

[1]*Physical-Technological Institute of Metals and Alloys, National Academy of Sciences of Ukraine, Kiev*
[2]*Zorya-Mashproekt Company*

The correlation relations between the technological parameters of the crystallization process, the macro- and microstructure and also operation characteristics (short- and long-term strength, corrosion resistance) of a high-chromium cheat-resistant nickel alloy of type KhN58KVT-MYuBR alloyed with rhenium and tantalum are analysed. The results are used to optimize the technological process of the manufacture of blades of hydro-turbine installations of a certain type and size with an oriented structure, characterized, as compared to the applied grades, by increased high-temperature creep and corrosion fracture resistance in corrosive emissions of heavy fuel and sea water salts. Ref. 14, Tables 3, Figures 4.

Introduction. Scientific and practical developments of recent years in both domestic and foreign research centres, concerned with the materials science of creep-resisting alloys for gas turbine systems (GTS), have been concentrated mainly on the blade materials for aircraft construction with a low content of chromium and, consequently, it was necessary to increase the strength characteristics. In the case of the GTS for naval applications and energy systems, including gas-pumping stations, in addition to the mechanical characteristics, another important parameter is the resistance to high-temperature corrosion (HTC), caused by the high-speed gas flow both with the corrosive components of diesel and gas fuel and also seawater salts. To increase the high-temperature resistance to corrosion after erosion failure, the main alloying complex should also be alloyed with a large amount of chromium (16…20 wt.%) in comparison with the materials for aviation engines (3…10 wt.%) which may

cause during service the formation of corrosion damage in the surface of the turbine blades and also embrittling topologically closepacked (TCP) phases [1–4].

Recently, material scientists have been using extensively elements such as rhenium, tantalum and ruthenium for the alloying of creep-resisting alloys; these elements are highly promising for increasing the strength characteristics in resistance to high-temperature corrosion [1–6]. This alloying reduces to a certain degree the chromium content, lowers the risk of formation of corrosion-erosion damage during service. Because of the lack of data on the effect of this elements on the phase-structural stability of high chromium alloys, including the stability associated with the liquation phenomena, to form the oriented structure in the process of directional solidification (DS) and also on the main service (strength and corrosion) characteristics in both the equiaxed condition and in the condition

after directional solidification, it was necessary to carry out systematic investigations to improve the currently available alloy grades.

The current state of the problem, experimental tasks. The currently available creep-resisting alloys based on nickel and cobalt of 3…5 generations are complexly alloyed hetero phase systems in which three main thermodynamically possible types of hardening take place: solid solution austenitic (γ-phase), dispersion (primary and secondary γ'-phases based on the compound Ni_3 (Al, Ti), and carbide hardening (Table 1) [1–4].

At a high chromium content, the structural stability of the alloys containing rhenium and tantalum with respect to the formation of the TCP phases is determined by both the total content of the refractory elements and by the ratios of the content of these elements. Chromium, molybdenum, tungsten, niobium, rhenium and tantalum are the hardening agents of the solid solution, and chromium, tantalum and tungsten are active carbide-forming elements, distributed preferentially in the γ-solid solution. For example, the addition of rhenium and tantalum to the alloyed is useful for retaining the phase-thermal stability in the process of service of the engine only at a specific balance of tungsten, molybdenum and chromium [1–4].

In complex alloying with refractory metals, it is important to take intow account their liquation coefficients, especially in producing alloys with the oriented structure. The addition to the composition of the alloying elements which increase the difference of the densities of the main alloy and the liquate, which relates to the γ'-forming (aluminium, titanium, niobium, etc) and refractory elements (tungsten, rhenium, molybdenum, etc) may support during directional solidification the formation of surface defects of the liquation origin, especially at a relatively low solidification rate [1, 2].

It should be mentioned that it is not rational to reduce or completely eliminate the precipice tension of the TCP phases by elements such

Table 1. Main components of the chemical composition of high half in chromium corrosion-resisting cast creep-resisting alloys, wt.%, based on nickel (according to the SNG standard).

Alloy	Ni	C	Cr	Co	Mo	Fe	Al
TsNK-7P	60.2	0.10	14.8	8.7	0.6	1.0	3.9
TsNK-8MP (NK)	61.4	0.01	12.2	8.7	0.4	1.0	4.1
TsNK-21P	56.9	0.07	21.0	10.7	1.5	1.0	2.4
ZMI-3	64.5	0.08	13.2	5.5	1.2	1.0	2.9
ZMI-ZU	64.8	0.15	13.0	5.0	1.0	1.0	3.0
ChS88 (mono)	57.6	0.09	15.6	10.7	1.9	0.5	3.0
ChS88U	57.0	0.06	15.9	11.0	1.9	0.5	3.05
ChS104	57.9	0.10	20.9	10.2	0.6	0.5	2.5

	B	Ti	W	Zr	Nb	Y	Hf	Ce
TsNK-7P	0.008	4.0	6.7	–	–	–	–	–
TsNK-8MP (NK)	–	4.5	6.7	–	1.0	–	–	–
TsNK-21P	0.008	3.4	2.3	–	0.7	–	–	–
ZMI-3	0.015	4.9	6.0	0.01	0.7	–	–	–
ZMI-ZU	0.010	5.0	7.0	–	–	–	–	–
ChS88 (mono)	0.005	4.6	5.3	–	0.11	–	0.5	–
ChS88U	0.080	4.6	5.3	0.05	0.2	0.03	0.3	0.015
ChS104	0.007	3.5	3.5	0.05	0.25	–	–	–

as molybdenum, tungsten, niobium, because each element controls to a certain extent of the phase-structural processes. Molybdenum, being a hardening agent of the solid solution, provides a significant contribution to the variation of the parameter of the γ-solid solution and, consequently, the morphology of the hardening secondary γ′-phase, making this phase cubic, leading to the high values of the creep resistance of creep-resisting alloys. The presence of niobium, which has a positive effect on the fluidity of the alloying casting, can be completely eliminated only by complex changes of the ratio of the alloying elements, changing the parameters of the γ-solid solution and the hardening γ′-phase [1–4].

Of all the elements of the alloying complex, included in the creep-resisting alloys, the highest solubility in the γ -and the lower solubility in the γ′-phase is shown by rhenium, with the distribution coefficients Kc (in the axes of the dendrites and in the inter-dendritic space) of the alloying elements situated between γ′- and γ-phases, $K/K_c = 0.1$ [5, 6]. The preferential dissolution of rhenium in the austenitic matrix of the alloy reduces the rate of diffusion processes, controlling softening of the metal in the high-temperature creep conditions, thus also reducing the rate of coalescence and dissolution of the γ′-phase. This results in the retention of long-term strength as a result of the increase of the high-temperature stability of the solid solution.

Empirical studies show that the increase of the concentration of the alloying elements with large atomic radii has a stronger effect on the variation of the parameter of the lattice of the γ-phase than on the parameter of the γ′-phase. Since the atomic radius of rhenium and tantalum is greater than that of nickel (the ratio for rhenium is 1.063), they have a positive effect on the misfit of the periods of the crystal lattices of the γ- and γ′-phases (misfit $\Delta a\gamma - \gamma' = a\gamma - a\gamma')/a\gamma$), which is the controlling factor of the long-term strength of the poly crystalline and single crystal creep resisting alloys at high temperatures.

Having the lowest diffusion coefficient in nickel, rhenium also inhibits the processes of coalescence of the hardening of the γ′-phase and, consequently, increases the thermal stability of this phase. In addition to this, both rhenium and tantalum increase the temperature of dissolution of the γ′-phase and T_S, and this reduces the width of the solidification range and, in most cases, has a positive effect on creep strength, especially in the condition after directional solidification [1–4].

It should be mentioned that when rhenium and tantalum regarded to the alloy, the chromium content can be reduced, because these elements, special rhenium, increase the resistance to high-temperature corrosion taking into account these factors of the beneficial effect of alloying with a rhenium and tantalum on the service characteristics of the creep-resisting nickel alloys, the authors of the present article carried out experiments to investigate the methods of preventing the precipitation of embrittling phases during the addition of this elements to the optimised high half in chromium composition based on the Ch104 alloy [7] using the experimental-calculation methods of determination of the temperature and time ranges of the precipitation of the TCP phases after long-term high-temperature holding [5, 6]. The experimental results show that the guaranteed 'safe' complex addition as regards the precipitation of the embrittling TCP phases is the addition of 1.5% rhenium +1.5% tantalum at a total content of 24.4 wt.% of the refractory elements [5, 6, 8–10].

The aim of the present study is the analysis of the effect of the temperature-time parameters of the solidification process on the physical-mechanical properties at room and high temperatures, including long-term strength in the cast and heat-treated conditions, and also the corrosion resistance of the optimised high-chromium alloy, complexly alloyed with rhenium and tantalum in the equiaxed condition and after directional solidification.

Experimental procedure. The simulation alloys were melted at the Physical-Technological Institute of Metals and Alloys, National Academy of Sciences of Ukraine, Kiev, to produce cylindrical blanks from the primary

charge in the casting systems UPPF-2 and UPPF-3M (Russian Federation, Rzhev) using the technological chart developed for the alloys of this group (furnace pressure 1.2…2.5 Pa, the temperature of pouring the metal into the moulds 1560…1580°C, the temperature of the mould 950°C).

The temperature-rate parameters of the process of production of the castings with the reference specimens were determined in the conditions of combined (radiation and convective) cooling of the mould (liquid aluminium) with the variation of the solidification rate v_{cr} = 2; 5; 10 mm/min in UVNK-8P equipment for directional solidification together with Zorya-Mashproekt, Nikolaev..

The primary blanks were melted using the basic charge materials: electrolytic cobalt K0, K1 (GOST 123–98), electrolytic nickel N0, cathodic nickel N1 (GOST 849–80), refined electrolytic nickel ERZh or metallic chromium Kh0, molybdenum in the form of bars of commercial purity, aluminium of grade A99 (GOST 1405–83), tantalum (bar 99.9 wt.%), rhenium (alloy Re0, Re1).

The temperatures of the main phase transformations (T_S; T_L; $T_{c.d.}$ – The temperature of complete dissolution of the γ'-phase) were determined by high temperature differential thermal analysis (HDTA) in equipment VDTA-8M with the accuracy of ±5°C.

The amount of the main components of the alloys and impurities was determined by the chemical method using the standard procedures, the microalloying additions were inspected by the chemical spectral method with the error of ±0.001%. The phase analysis of the alloys was carried out by the electrochemical separation of the intermetallic and carbide phases in a methanol etching agent followed by x-ray diffraction and chemical analysis of anodic deposits. The distribution of the alloying elements between the phases was investigated in the microanalysers JXA8600, JEOL (Japan), and CAMECA-MS46, Cameca (France). The macro- and microstructure was studied using a Neophot-2 optical microscope and electron microscopes. The content of the gases (oxygen, nitrogen, hydrogen), carbon and sulphur

in the solid metal was analyse in the LECO analysers – RO-17, TN15, RH2, CS-144.

The volume fraction and size of the phase components were determined in the Quantimet-720 analysers, together with a JSM-840 scanning electron microscope. The relative error of determination of the values of these parameters was 5…10%. The coefficients of liquation of the alloying elements were determined by quantitative elemental analysis, carried out by x-ray diffraction microanalysis.

The mechanical terms of the short-term strength were carried out on standard cylindrical specimens with the gauge part 5 mm in diameter and 25 mm long in accordance with GOST 9651–84 at a temperature of 20–950°C in a UME-10TM tensile machine. Long-term strength was determined in accordance with GOST 10145–81 on an AIMA-5-2 tensile machine at the parameters, prescribed by the standard documents for the alloys.

The casting moulds were made of multilayer ceramic based on an electric corundum suspension with the modification agents increasing the thermal strength of the moulds [9]. The bars for the shaping of the internal cavity of the blade were in the form of bars based on corundum and zircon, modified with silicon and the Al + Si complex modification agent [11].

Experiments and results. The calculations [11, 12] and the experiment conditions (equipment UVNK=8P equipment, alloy ChS104, the working blades of high-pressure turbines) were used to determine the thermophysical parameters of the process of directional solidification. The local values of the parameters of the directional solidification process throughout the entire technological cycles were measured on the basis of the distribution of temperature in the solidifying casting, constructed on the basis of the experimentally measured values of temperature at six points along the axis of the casting using a thermocouple cover with six tungsten–rhenium thermocouples (type VR 5/20, electrode diameter 0.30 mm). All the thermophysical properties of the metal in the mould were assumed to be constant. The heat

I.I. Maksyuta, O.V. Klyass, Yu.G. Kvasnitskaya, G.F. Myal'nitsa and E.V. Mikhnyan

Table 2. Temperature-time parameters of the process of directional solidification (casting system UVNK-8P)

Delay of mould movement, min	Initial speed of movement of mould from heater, mm/min	Gradient at solidification front, K/cm
5...6	2.0...3.5	25...30
2...3	6.0...8.0	35...50

Commnent.M ould emp rature ₃ 0° C,m elt temp rature ℃ C

conductivity of the mould, the metal, the cooling agent, the temperature of the lower base were determined on the basis of the conditions of heat exchange through the bottom of the mould to the cooler of equipment (Table 2). The temperature of the outer surface of the mould for casting of the blades with the polycrystalline structure changed along the height in the range 950…1050°C and was assumed to be constant (975°C with the error of 2…3%).

Analysis of the directional solidification conditions in the UVNKI-8P equipment in the given conditions shows that the temperature of the cooler can be left constant. The resultant values of the temperature gradient G in the solidification rate vcr were used to calculate the ratio G/v_{cr} – the criterion of the stability of the flat solidification front, resulting in the formation of a regular dendritic structure along the longitudinal axis of the blade, including the thick closing section and the thin wall vane section. The drift of the solidification front can be controlled on the basis of the speed of displacement of the mould.

It should be mentioned that the rate of extraction of the mould from the heater, according to the main requirement on the directional solidification process, should not be greater than the minimum rate of natural growth of the solid phase, equal to 0.006 cm/s (3.6 mm/min), determined on the basis of the slope of the tangents to the kinetic curve. Thus, the initial speed of movement of the mould was 2.0…3.5 mm/min after preliminary holding for 5…6 min. Subsequently, the rate was changed to 5…7; 7…10; 10…15 mm/min.

The results of analysis of the main structural elements of the simulation alloys with rhenium and tantalum (specimens-satellites and blades of the gas turbine engines) show that the formation of the dendritic-cellular structure takes place in the expanding sections of the castings, and the side surfaces of the castings are characterised in some cases by the formation of new solidification centres outside the existing flat front of growth.

Metallographic analysis of the simulation alloys shows that in the examination of the macrostructure after the directional solidification process, there are several types of subgrains: the subgrains representing individual dendritic arms within the limits of the same colony, whose dimensions correlate with the dimensions of the arms, and the disorientation is 0.5…1.0°; the subgrains belonging to the groups with different orientation of the dendrite arms with the same direction with the dimensions comparable with the dimensions of the casting and with the disorientation between them of 1…3°; the finest subgrains with the size of 20–30 μm, the disorientation 20…30°.

Since the nickel-based alloys are characterised by the phase-centred cubic lattice, the formation of the dendrite arms of the first order takes place along the [001] crystallographic directions; this relates to the arms forming the minimum angle with the vector of the temperature gradient G in the process of directional solidification. The arms of the first order have the form of parallel rows along the [001] planes decorating at the same time the spatial position of these planes in the casting. The interdendritic space λ in the investigated case is the mean statistical distance between the dendritic arms of the first order, measured in the shortest direction, i.e. [001], and is determined graphically by the mean distance λ on the cross-section of the ingot with the arbitrary orientation $\lambda_a = e_a \cos \alpha$, where α is the angle between the [001] plane, forming a trace, and the axis of the ingot [1, 12].

The value $\bar{e}$ was calculated on the basis of the density of the dendrite rows, forming a

Table 3. Effect of the solidification rate on the characteristics of the micro- and macrostructure of the simulation alloy, complexly alloyed with tantalum and rhenium

Solidification rate, mm/min	Parameters of structural components, µm			
	Interdendritic space λ_p, µm	Mean size of the 'islands' of the γ'_{eut}-phase	Mean size of the particles of the secondary γ'-phase in interaxial spaces/dendrite arms	Mean size of particles of MeC type carbides
2	265	10.0	0.65/0.70	2.4
5	250	8.7	0.53/0.45	2.2
10	210	7.0	0.4/0.3	1.5

linear row on the micrographs in the direction perpendicular to the rows in accordance with the method proposed in [11]. For statistical reliability of the investigated at least three fields of view in fine grains, cos α was measured on the longitudinal section, dissecting the body of the grain on the cross-section.

The experimental results confirm that the form and size of the particles of the γ'-phase greatly differ in the axes and interaxial spaces (Table 3). It should also be noted that the dispersion of the primary γ'-phase in the volume fraction of the eutectic γ'-phase, distributed in the interaxial spaces in the form of 'islands' of irregular shape, also depend on the solidification rate (Table 3), and increase with the increase of the rate. This indicates the non-equilibrium nature of this phase. The exact quantitative determination of the volume fraction of the particles of the γ'-phase in the dendrite arms and interaxial spaces is difficult because of the very small particle size. The morphological changes in the structure during growth or a reduction of the solidification rate also change the level of liquation of the elements in the alloy and this leads to the formation of large areas of the eutectic-temperature γ'$_{eut}$-phase.

Since the main mass of the MeC carbides based on (Ti, Ta) C was distributed in the interaxial spaces, and precipitates from the melt in the vicinity of the solidus temperature (Fig. 1), the size of the carbides, like the size of the 'islands' of the eutectic γ'-phase decreases with increase of the solidification rate and this is matched with the size of the dendrite cell (Table 3).

In addition to this, the experimental results show that the addition of tantalum to the basic alloy of the type Ch104 leads to the formation of a large number of the complex carbide of the Me_6C type (Fig. 2), which according to the x-ray diffraction microanalysis results, container to 10 wt.% of chromium and tantalum.

Examination by the method of high-temperature DTA showed the displacement of the level of the values for the critical points T_L, T_c, d in the direction of increase both when adding 1.5...3.0 wt.% of rhenium [9] and in complex alloying with rhenium and tantalum with a total of up to 3 wt.% (Fig. 1). This confirms the possibility of increasing the temperature level of the efficiency of the proposed composition mostly as a result of increasing the temperature threshold of dissolution of the γ'-phase and a reduction of the size of the solidification temperature range.

The secondary disperse γ'-phase, localised in the interdendritic spaces, is also refined, retaining mostly the form close to the spherical, and changing the size from 0.4...0.6 to 0.2...0.3 µm. The increase of vcr is accompanied by the appearance in the structure of a large number of particles of the carbide phase of the rod-shaped morphology of the MeC type based on titanium characterised by lower thermal stability in comparison with the disperse faceted carbides MeC.

All the metallographically recorded quantitative and morphological changes in the structure of the elements when the solidification rate was higher than 10 mm/min are

Fig 1. Values of the temperature of the main phase transformations (T_S, T_L, $T_{c'd}$) of the simulation (1.5% rhenium and 1.5% tantalum) and basic alloys.
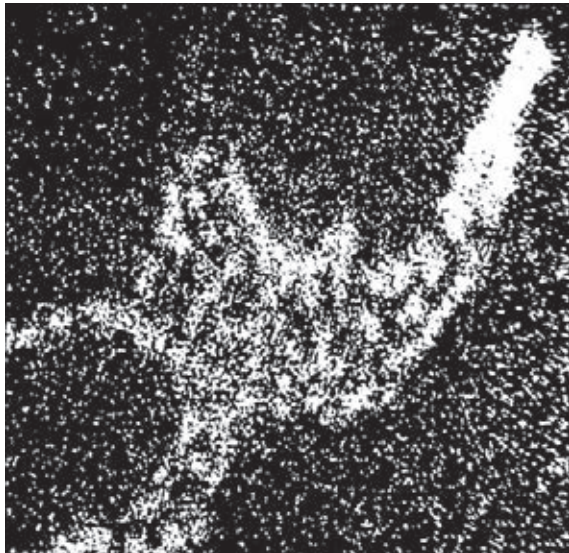

Fig. 2. Distribution of tantalum in the carbide phase (x-ray diffraction microanalysis, in the characteristic tantalum beams), ×3000.

the consequence of the increase of the degree of non-equilibrium of the alloys which, as shown by the mechanical tests, results in a reduction of the level and long-term strength and ductility.

In the region of controlled growth at $v_{cr} = 5$ and 10 mm/min, the degree of regularity of the dendritic structure is satisfactory, and the examination of the cross section shows that the dendrites are in the form of the 'Maltese cross' with the distance between the dendrite arms of λ 130…150 μm.

Analysis of the effect of the technological parameters of the process of directional solidification in the selection of the optimum solidification rate, ensuring the formation of the regular oriented structure of the simulation alloys of the type KhN6OKMYuVT were used for transition to the selection of the conditions of heat treatment of the alloys in order to increase the service characteristics of the alloys. The duration of heat treatment, required for dissolution of the γ/γ′ eutectics depends on the dendritic spaces in the alloy – as the value of λ and the volume 'islands' γ/γ′ decrease, the time required for

homogenising decreases. Homogenising results in a partial reduction of the level liquation heterogeneity of dendritic segregations. At λ = 150…180 µm and the mean cross-section of the 'islands' of the γ/γ'-eutectics of 18…25 µm in the initial state prior to heat treatment the optimum homogenising time was 3 hours at a temperature of (1220 ± 5)°C, in contrast to the heat treatment of Ch104 alloy. The selected heat treatment conditions supported the dissolution of a large amount of the γ/γ'-eutectic. For example, prior to heat treatment the volume fraction of the eutectic was 2.5…3.0%, and after heat treatment 1.5…2.0%, and the mean diameter of the 'islands' of the γ/γ'-phase decreased to 15…20 µm. This was also accompanied by an increase of the volume fraction of the disperse γ'-phase, together with the refining of the particles of the phase to 0.2…0.5 µm (Fig. 3).

It should be mentioned that since the cur-rently used blades of the gas turbine engines have the form of a curved ellipse, the thickness of the cross-section of the blade also changes in accordance with the parabolic law and decreases in the direction to the input and output blades. Naturally, the distribution of temperature in the cross-section of the vane is parabolic and this has a strong effect on the degree of dispersion and the start of the process of coalescence of the precipitated phases in the thick bands and at the edges, and determines the strength characteristics and corrosion resistance of the blade as a whole (Fig. 4, Table 4). This special feature of the design should be taken into account when selecting the heat treatment temperature.

The determination of the main service characteristics of the specimens of the simulation alloys showed that the strength characteristics after adding rhenium and tantalum to the basic alloy in the optimum amounts determined previously by the authors (a total up to 3 wt.%) [13] whilst retaining the phase and structural stability after long-term ageing improve the efficiency of the material, including long-term strength, probably as a result of the hardening of both the solid solution, increase of the temperature of complete dissolution of the γ'-phase and of the inter-axial sections of the matrix after directional solidification with a large volume amount of the stable dispersed precipitates of the MeC- and Me$_6$C-carbides with a higher content of chromium and tantalum. The appearance
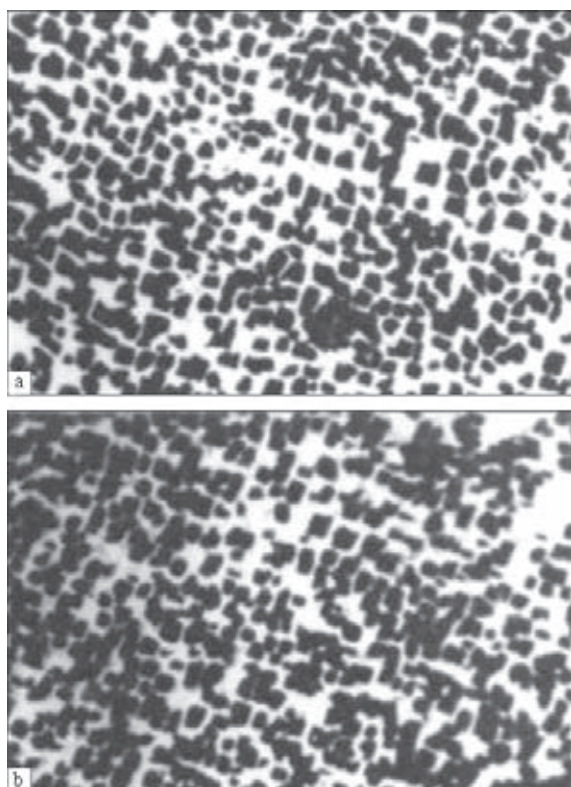

Fig. 3. Special features of the morphology of the hardening γ'-phase (??? blades, looking part): *a*) after casting (vacuum-induction melting, equiaxed state); *b*) after directional solidification; *a*, *b*) ×3000.
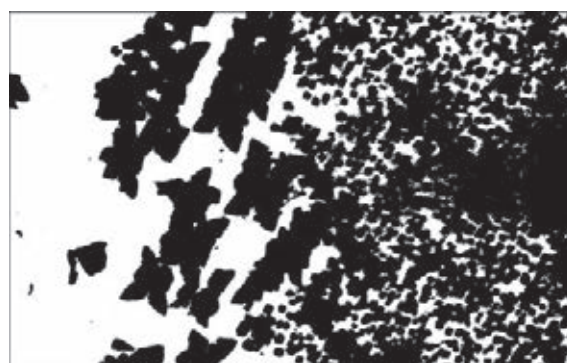

Fig. 4. Precipitates of the γ'-phase at the interface between the input *H* of the blade and the central part after long-term ageing (*T* = 900 °C, 1000 hours), carbon replicas with extraction.

I.I. Maksyuta, O.V. Klyass, Yu.G. Kvasnitskaya, G.F. Myal'nitsa and E.V. Mikhnyan

Table 4. Comparative strength characteristics and corrosion resistance of the investigated Ch104 alloy

Test temperature, °C	Yield limit, MPa	Tensile strength, MPa	Relative elongation, %	Relative reduction in area, %	Impact toughness, MJ/m^2	Endurance limit at 2..10 cycles, MPa	Creep strength, MPa, 100 h	Corrosion rate v_q, mg/(m^2 h) ... 10^4
20	790...870	920...1050	4...7	5...10	0.10...0.18	185	–	–
	820...840	900...980	2...3	4...5		160		
900	570...680	640...750	9...16	9...12	–	–	280	3.2
	440...460	610...690	2...8	7...13			310	3.3
950	–	–	–	–	–	–	–	4.2
	370...390	460...470	13...18	24...28				4.5

of these carbides may reduce the probability of precipitation in the solid solution in long-term high-temperature effect on the alloy of embrittling phases of the type σ and μ as a result of reducing the solubility of these refractory elements in the solid solution.

Investigation of the resistance of the simulation compositions to the high-temperature corrosion in salt melts in accordance with the procedure described in [14], the minimum (15.0 wt.%) and maximum (17.0 wt.%) content of chromium, according to the data in the certificate for the Ch104 alloy, indicates that the value of the corrosion rate in complex alloying with tantalum and rhenium at the minimum chromium content of the specimens was on average 0.25…0.30 wt.% higher than the maximum chromium content added to the Ch104 basic alloy. Thus, the level of corrosion resistance can be improved as a result of alloying with tantalum and rhenium at a lower chromium content of the alloy (up to 15.0 wt.%) which greatly reduces the risk of precipitation during service of the embrittling close-packed phases in both the equiaxed condition and the condition after directional solidification. Evidently, the formation of the majority of carbides of the type MeC based on tantalum and titanium during the addition of the active carbide-forming element, which includes tantalum, causes that a large part of chromium is not used for the formation of the Me$_{23}$C$_6$ By and remains in the austenitic matrix, increasing the corrosion resistance of the material.

Conclusions

Analysis of the effect of the temperature-time parameters of the processes of directional solidification of the structural special features, the mechanical properties at room and high temperatures, and also high-temperature corrosion resistance in the salt melts of the KhN58KVTMYuBR simulation alloy (ChS104 based grade), additionally alloyed with rhenium and tantalum (with a total up to 3 wt.%) show the positive effect of these elements on the service characteristics so that it was possible to reduce the chromium content of the alloy in order to increase the structural stability of the alloy during long-term service.

References

1. Kablov E.N., Cast blades of gas turbine engines, Moscow Institute of Steel and Alloys, Moscow, 2001.
2. Sims Ch.T., et al., Creep-resisting materials for aerospace and industrial energy systems, Metallurgiya, Moscow, 1995, volume 1.
3. Yatsyk S.I., Production of high-temperature cast aviation blades, Mashinostroenie, Moscow, 1995.
4. Toloraiya V.N., et al., Lit. Proiz., 2012, No. 6.
5. Myal'nitsa G.F., et al., Prots. Lit'ya, 2012, No. 6, 54–61.
6. Myal'nitsa G.F., et al., Metall i lit'e Uktainy, 2012, No. 11, 16–20.
7. Kablov E.N., et al., Metalloved. Term. Obrab. Met., 2002, No. 7, 2–5.
8. Kablov E.N., Vestn. Moskov. Un-ta, Ser. 2: Khimiya, 2005, **46**, No. 3, 155–157.
9. Toloraiya V.N., et al., Metalloved. Term. Obrab. Met., FGUP VIAM, Moscow, 2001, No. 1, 30–32.
10. Simanovskii V.M., et al., Prots. Lit'ya, 2010, No. 3, 69–75.

11. Simanovskii V.M., et al., ibid, 2010, No. 6, 8–13.
12. Maksyuta I.I., et al., Metall i lit'ye Ukrainy, 2012, No. 11, 16–20.
13. Myal'nitsya G.P., et al., Metaloznavstvo ta obroka metaliv, 2013, No. 2, 29–33.

14. 105.15–2001. Instructions I ZhAKI. Creep-resisting alloys for gas turbine blades (Certificate of Ch104 VI alloy), 2012.

Submitted 18.10.2013

Physical-chemical features of degassing of molten steel to remove hydrogen in ladle treatment in the electrostatic field

N.I. Zakharov, A.A. Troyanskii and D.A. Dyudkin

Donetsk National Technical University, ul. Arteme 58, 83000 Donetsk, Ukraine

The effect of intensification of the kinetic stage of the process of mass transfer in degassing of molten steel to remove hydrogen by the complex vacuum effect, blowing with argon and the electrostatic field ($0 \ll E \ll 3...18$ kV/cm) is studied. This field forms a region of the increased concentration of hydrogen ions at the vacuum–metal surface, localized in the vicinity of projection of the electrode boundary on this surface. The effect was theoretically studied using the conventional electric dynamics and tested under the laboratory conditions. The correlation of the Sieverts law by introduction of the intensity of the electrostatic field and the level of ionization of the hydrogen atoms in it is generalized. The correlation is qualitatively coordinated with the results of laboratory investigations. It can be used in the computer modelling of convective mass transfer of hydrogen in molten steel for a new type of the external effect on the metal. Ref. 8, Figures 6.

Scientific and research studies concerned with the application of the electrostatic fields in the technology of ladle refining of steel to remove hydrogen started in the previous century [1–4]. At the centre, the question of the degree of ionisation of the hydrogen atoms in molten metal has not as yet been completely answered. It may be assumed that with increasing liquid metal temperature, the parameters of this characteristic increase. The current views regarding the form in which hydrogen is found in the molten metal should include the historic concept of electrically neutral atoms of this gas as a partial variant relating to liquid (low-melting) metal with insufficiently high temperature.

In computer modelling of the mass transfer of hydrogen in the liquid metal in the conditions of the complex effect on the melt of vacuum, concentrated blowing with inert gas (for example, through a porous nozzle, placed in the bottom of the ladle) and the electro-static fields with the sub-critical strength, it is necessary to solve the problem of formulation of the boundary conditions for the equation of convective diffusion at the vacuum-metal interface. The classic form of writing the law of the square root of the Sieverts law does not take into account the effect of the electrostatic fields on the surface of the melt.

One of the possible forms of writing this law in the conditions of the investigated type of the complex effect on the liquid metal can be expressed by the relationship:

$$C_n = K_H \sqrt{P_{H_2}}[(1-i)+iK_E] \qquad (1)$$

where C_n is the concentration of the hydrogen atoms and ions on the surface of the melt; P_{H_2} is the partial pressure of hydrogen in the vacuum chamber; K_H is the Sieverts constant; i is the dimensionless degree of ionisation of the hydrogen atoms on the interfacial surface; K_E is the dimensionless function of
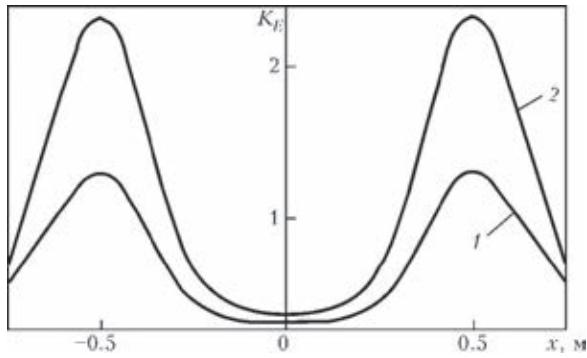
Fig. 1. Distribution of the concentration of the hydrogen ions at the interface of the strength of the electric field of 1 (*1*) and 2 kV/cm (*2*).
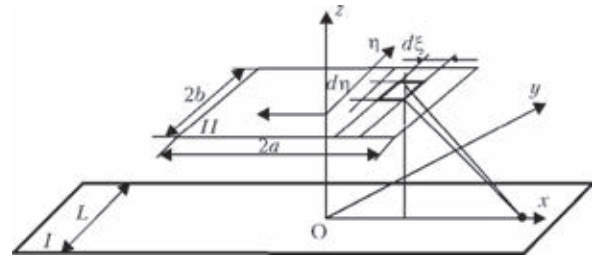

Fig. 2. Diagram of a flat liquid metal conductor and a source of the Coulomb field in the form of a charged particle: *I*) the flat liquid metal conductor and the source; *II*) the source of the external field; *xOy*, *ξOη*) the system of the coordinates, rigidly connected with the conductor and the source.

the coordinates, characterising the ratio of the concentration of completely ionised hydrogen atoms at the vacuum-metal interface ($i = 1$) to the identical characteristic at $i = 0$ (Fig. 1).

Theoretical analysis of the distribution of the hydrogen atoms on the vacuum-metal interfacial surface was carried out assuming that their complete ionisation. The relationship (1) generalises the results regarding the possibility of their partial ionisation. In addition to this, it is necessary to ensure the electrodynamic equilibrium of the system in which the distribution of the density of the charge of hydrogen ions on this surface at every moment of time for a moving melt is identical to the case of its stationary state. The required distribution of the density of the charge of the hydrogen ions on this surface is determined by the Maxwell equations [5]:

$$\operatorname{div} \vec{E}' = 4\pi\rho \qquad (2)$$

where $\vec{E}'$ is the strength of the intrinsic field of the investigated ions with the density ρ.

To calculate this equation, we consider a flat liquid metal conductor whose plane is parallel to the surface of the negatively charged particle – the source of the electrostatic field (Fig. 2).

It is assumed that in movement of the metal along the axis $\overrightarrow{Ox}\, \partial E'_x / \partial x >> \partial E'_y / \partial y$.

In addition to this, since the vertical component $\vec{E}$, i.e., E'_z, has no effect on the movement of the ionised part of the atoms

of the removed gas in the plane (*xOy*), equation (2) gives

$$\rho(x) = \frac{1}{4\pi}\frac{E'_x}{\partial l}$$

In this case, in the dynamically equilibrium state

$$E'_x = -E_x$$

We determine the value of E_x.

Let it be that Q is the modulus of the charge of the source. The value of the charge in the element $d\xi d\eta$ during its uniform distribution on the surface of the source is equal to $(Q/4ab)d\xi d\eta$, where *a*, *b* is the half length and half width of the plate, respectively.

The strength of the external field in the point of the metal surface with the coordinate *x* is as follows:

$$d^2 E_x = \frac{kQ}{4ab}\frac{d\xi d\eta}{[H^2 + (x+\xi)^2 + \eta^2]}$$

where *H* is the distance between the plane's;

$k = \dfrac{1}{4\pi\varepsilon_0\varepsilon}$ is the Coulomb constant.

After integration

$$E_x \frac{kQ d\xi}{4ab}\int_{-b}^{+b}\frac{d\eta}{[H^2 + (x^2 + \xi^2) + \eta^2]}$$

$$= -\left(\frac{kQ}{2ab}\right)\frac{\operatorname{arctg}\left(b/\sqrt{H^2 + (x^2 + \xi^2)}\right)}{\sqrt{H^2 + (x^2 + \xi^2)}}d\xi$$

After second integration

$$\rho(x) = \frac{1}{4\pi}\frac{dE_x}{dx} = -\frac{1}{4\pi}\left(\frac{kQ}{2ab}\right)\frac{d}{dx}\int \times$$

$$\frac{\text{arctg}\left(b/\sqrt{H^2+(x^2+\xi^2)}\right)}{\sqrt{H^2+(x^2+\xi^2)}}d\xi$$

$$= -\frac{kQ}{8\pi ab}\int_{-a}^{+a}F(x,\xi)d\xi$$

where

$$F(x,\xi) = \frac{d}{dx}\left[\frac{\text{arctg}\left(b/\sqrt{H^2+(x^2+\xi^2)}\right)}{\sqrt{H^2+(x^2+\xi^2)}}\right]$$

$$= \frac{(x+\xi)}{[H^2+(x^2+\xi^2)]^2} \times$$

$$\left[b+\sqrt{H^2+(x^2+\xi^2)}\,\text{arctg}\frac{b}{\sqrt{H^2+(x^2+\xi^2)}}\right]$$

In computer simulation of the process, the initial data in the SI system were represented by the following values of the parameters:

$$H = 0.1 \text{ м}; \rho_{me} = 7.0 \cdot 10^{+3} \text{ kg/m}^3;$$
$$A_{me} = 56 \text{ kg/mol}; \varepsilon = 1;$$
$$N_e = 2; a = 0.5 \text{ m}; b = 0.25 \text{ m}.$$

In addition to this, the following values of the constants were included in the computer module:

$$\varepsilon_0 = 8.85 \cdot 10^{-12} \text{ C}^2/\text{H} \cdot \text{m}^2;$$
$$N_A = 6.023 \cdot 10^{+26}\frac{1}{\text{m}^3};$$
$$e_H = +1.6 \cdot 10^{-19} \text{ C}$$

where N_A is the Avogadro number; e_H is the proton charge (hydrogen ion); ρ_{me}, A_{me} is the density and mass of 1 kg mole of iron, respectively; N_p is the number of the electrons on the outer orbit of this element; ε_0 is the dielectric constant; ε is the permittivity of the medium in the vacuum chamber.

The dimensionless function K_E (Fig. 1) is determined by the relationship

$$K_E = (M_H/e_H)(\rho K_H\sqrt{P_{H_2}})$$

where M_H is the mass of the hydrogen ion.

As indicated by the distribution of the concentration C_n on the vacuum-metal interfacial surface (Fig. 3), the region of projection of
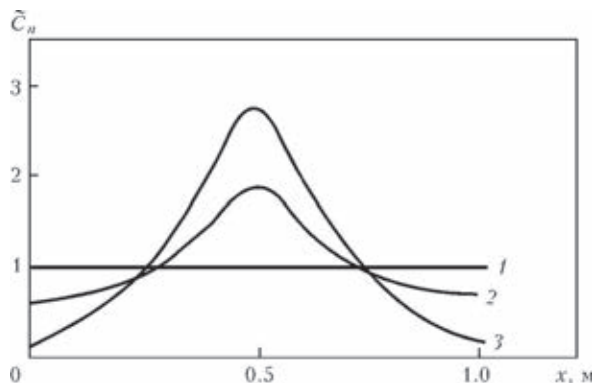

Fig. 3. Distribution of the dimensionless concentration $\tilde{C}_n$ of the atoms and ions of hydrogen at the metal-vacuum interfacial surface at the degree of ionisation of the atoms 0 (*1*); 0.5 (*2*); 1.0 (*3*); *E* = 2.0 kV/cm.
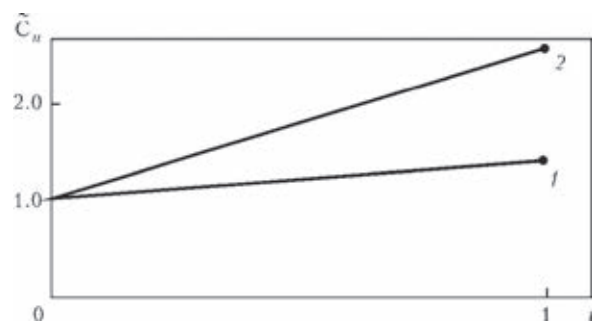

Fig. 4. The dependence of the maximum concentration $\tilde{C}_n$ of the hydrogen atoms and ions at the metal-vacuum interfacial surface on the degree of ionisation i of the atoms and the strength of the electric field of 1 (1) and 2 kV/cm (2).

the boundary of the electrode (the source of the external field) on this surface showed the maximum of the concentration (cluster) of the hydrogen ions whose size increases with increasing strength of this field (Fig. 1) and the degree of ionisation of the hydrogen atoms (Fig. 4).

The direct experimental modification of the relationship (1) is difficult because of problems in the experimental determination of *i*.

In the indirect determination of the validity of this analytical formula, it should be noted that at *E* = 0; K_E = 1, the relationship (1) acquires the classic form of the Sieverts law. The identical form is also observed at *i* = 0. The third criterion of the validity of the equation (1) is the qualitative experimental confirmation of the presence of the maximum

in the distribution of the concentration C_n on the surface of the metal, determined by calculations and experiments. The results of experimental studies confirmed the presence of a cluster of the free charges on the surface of the metal during its movement in the electrostatic fields of subcritical strength.

The experiments carried out using equipment for the generation of electric current during rotation of the current-conducting sphere in the electrostatic fields with subcritical strength. We will use the well-known fact of classic electrostatics. In introduction of a stationary current-conducting sphere into the electrostatic (Coulomb) field the conduction electrons of the sphere are redistributed, as a result of electrostatic induction, in such a manner that an electron cluster will be recorded in the vicinity of the positively charged electrode in the section of this spherical surface. According to the proposed theoretical model, if the sphere rotates, the presence and localisation of this cluster do not change, but this is possible only if the cluster moves in relation to the investigated conductor and in closure of the electric circuit is message possible to record the current. In this case, there is a continuous sequence of the redistribution of the conduction electrons, determined by the tendency of the particles to equilibrium with the external field, leading to the displacement of the electrons in relation to the surface of the metallic conductor. In the electrodynamic equilibrium conditions, the displacement of some electrons to the cluster is accompanied by the loss of other electrons.

Evidently, the maximum concentration of the conduction electrons in the cluster will increase with increase of the strength of the Coulomb field. Since the cluster is stationary in relation to the electrode, then in relation to the surface of the conducting sphere it will travel at the speed of rotation of the sphere in the opposite direction.

Thus, the value of the generated current, if its nature is determined by the presence, localisation and displacement of the cluster of the free charges of the metallic conductor, should be directly proportional to the
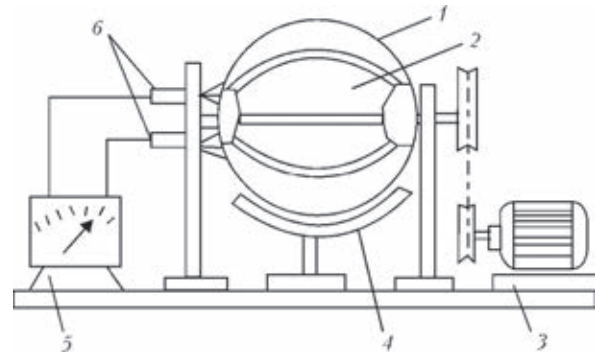

Fig. 5. Laboratory equipment for the determination of cluster of free charges of a metallic conductor during its movement in the electric field: *1*) the dielectric sphere; *2*) segments of aluminium foil; *3*) motor; *4*) electrode with a current conducting layer; *5*) galvanometer; *6*) current-collecting brushes.

speed of rotation of the sphere and should increase with the increase of the strength of the external field.

In the experiments shown in Fig. 5, a dielectric sphere with a diameter of 0.25 m was used. Segments of aluminium foil were bonded to the surface of the sphere to act as conductors. To record the electric current, the segments (8 segments) where separated from each other by gaps of 0.003 m. At the ends of the sphere on the insulators there were two current-collecting brushes correcting the adjacent segments with the M1032 galvanometer.

In the lower part of the sphere at a distance of 0.01 m there was a special support carrying an electrode whose outer side had a current-conducting layer which received the positive from the external source. The sphere was rotated with a motor. During rotation of the sphere, the c;uster of the conduction electrons was scattered at the boundaries of the segment in the direction of the ends. The electrons of the cluster were passed through the galvanometer, which recorded the direct current [6].

Figure 6 shows the dependence of the generated current on the speed of rotation of the sphere and the strength of the external field. Thus, the experiments fully confirmed the predictions.

The increase of the concentration of the chemically reacting particles increases the rate
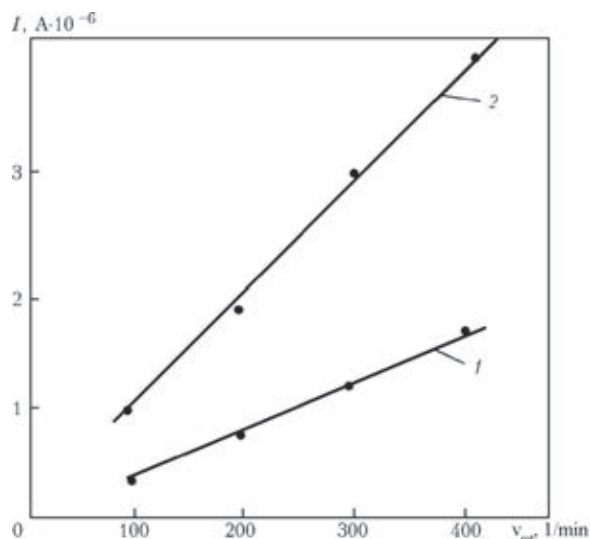
Fig. 6. Dependence of current *I* on the speed of rotation v_{rot} and the strength of the Coulomb field of 2(*1*) and 10 W/m (*2*).

of the chemical reaction [7]. For example, at *E* = 1 kV/cm, the increase of the rate of the molisation reaction 2 [H] = {H$_2$} is equal to a factor of 2.5 and at *E* = 2 kV/cm to a factor of 6.

The results of fundamental (theoretical and laboratory) investigations were used to determine the scientific assumptions for the intensification of this technology, if the molisation term takes part in the restriction of the mass exchange processes [8].

Conclusions

1. The results were used for the theoretical substantiation and experimental confirmation of the effect of intensification of the kinetic (molisation) term of the mass exchange processes of ladle degassing of liquid steel to remove hydrogen by the complex effect of vacuum, concentrated blowing with the inert gas and the electrostatic field of the moderate (subcritical) strength (according to the Muller data for steel E_{cr} ~3…18 kV/cm).

2. The mechanism of the effect is based on the formation, by this field, of the region of higher concentration (cluster) of the ionised part of the hydrogen atoms, situated in the state of the continuously distribution during mixing of the melt. The cluster is localised in the region of projection of the boundary of the electrode (the source of the Coulomb field) on the vacuum-metal interfacial surface.

3. The Sieverts square root law was generalised in order to widen the range of its effect.

References

1. Yavoiskii V.I. and Batalin G.I., Stal', 1954, No. 6, 5–6.
2. Muller E.V., Usp. Fiz. Nauk, 1962, No. 37, 481–552.
3. Kaibichev A.V. and Lepinskii B.M., Refining of liquid metal and alloys in the electric field, Nauka, Moscow, 1983.
4. Romanov A.N., Electrophysical methods and technologies of influencing the structure and properties of metallic materials, Nauka, Moscow, 1990.
5. Landau L.D. and Lifshits E.M., A short course of theoretical physics. Electrodynamics, Nauka, Moscow, 1969.
6. Dyudkin D.A. and Zakharov N.I., Electrodynamic induction and the problem of its application in the processes with movement of metal in the electrostatic fields, in: Metallurgy of the 21st century, International conference, Moscow Institute of Steel and Alloys, Moscow, 2001, 500–505.
7. Kharlashin P.S., Theoretical fundamentals of advanced steel melting processes, Vishch. shk., Kiev, 2008.
8. Zakharov N.I., et al., Protsessy lit'ya, 2009, No. 1, 8–11.

Submitted 22.08.2013

Effect of the dispersion of charge materials on aluminothermic processes in melting of ferrotitanium

D.A. Kazarin, N.P. Volkotrub and M.I. Prilutskii

Kiev Polytechnical Institute, National Technical University of Ukraine

The improvement of quality of basic structural material (steel) is attained by adding of alloying elements into the melt. Ferrotitanium is one of the most widely used and technologically effective alloying element. The quality of ferrotitanium depends on some factors (composition and mass of charge, process temperature, preheating of charge, shape and specific surface of powders, size of charge materials, density of charge, application of heating and fluxing additions, etc). The effect of the dispersion of charge materials on the process of aluminothermic production of ferrotitanium is shown. Melting was performed in a crucible 400 mm long, 200 mm diameter, lined with a mixture of magnesia powder (95%), water glass (0.7%) and fire-clay (4.3%). The lining thickness was 15...20 mm. It was found experimentally that the maximum yield of metal is attained at sizes of deoxidizer particles, close to those of recoverable oxide ($d_{Al}/d_{ox} \sim 1$). It is shown that additional refining of the charge materials does not lead to the expected increase in the metal yield due to increase of the reaction surface. In this case, due to reduction in gas permeability parts of the melt were ejected during melting and the ferrotitanium were porous. A large number of iron beads remained also in the slag. It was found that the size of charge materials should not exceed 2 mm, moreover, it is not necessary to refine them to the size of less than 0.1 mm. Ref. 9, Tables 2, Figures 3.

Keywords: *ferroalloys; ferrotitanium; flumothermy; dispersion; charge; ilmenite; reducing agent; metal thermal reduction*
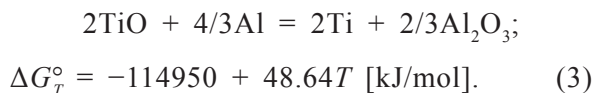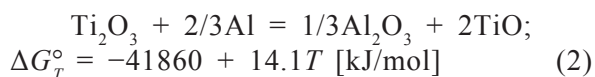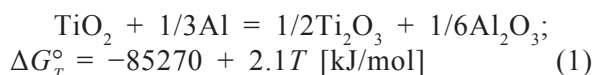
The main direction in the development of ferrous metallurgy at the present time is not associated with the increase of the volume of production of materials, as was the trend in the past, but it is associated with the increase of the quality of production at a relatively low rate of increase of the physical volume of production, i.e., it is required to produce structural materials with a low metal requirement but with a higher level of the mechanical properties as a result of introducing alloying elements into the melt. Sometimes, these elements are added in the your form but, usually, in the form of ferroalloys – the alloys of iron with alloying elements.

The application of ferroalloys as refining additions to the liquid steel melting pool aimed at the deoxidation and alloying of the melt increases the physical-mechanical properties and functional characteristics of metal products. Not a single tonne of steel is melted without the application of ferroalloy is [1]. One of the most widely and technological F ferroalloys is fellow titanium which is added to the melt for alloying, degassing in the oxidation of steel [2]. For example, in corrosion-resisting steels titanium reduces the degree of intercrystalline corrosion and improves weldability. In corrosion-resisting in creep-resisting steels, titanium is used as a stabilising element binding carbon and preventing the formation of chromium carbides.

The main amount of ferrotitanium is produced from ilmenite concentrators ($FeO \cdot TiO_2$), usually by the aluminothermic method [3–6].

The reduction of titanium from ilmenite by aluminium takes place by the following reactions:

$$TiO_2 + 1/3Al = 1/2Ti_2O_3 + 1/6Al_2O_3;$$
$$\Delta G_T^\circ = -85270 + 2.1T \text{ [kJ/mol]} \quad (1)$$

$$Ti_2O_3 + 2/3Al = 1/3Al_2O_3 + 2TiO;$$
$$\Delta G_T^\circ = -41860 + 14.1T \text{ [kJ/mol]} \quad (2)$$

$$2TiO + 4/3Al = 2Ti + 2/3Al_2O_3;$$

$$\Delta G_T^\circ = -114950 + 48.64T \text{ [kJ/mol]}. \quad (3)$$

At the temperatures of ferroalloy processes the probability and direction of the reactions are evaluated by the reaction:

$$\Delta G_T^\circ = \Delta H_T^\circ - \Delta ST$$

where ΔG_T°, ΔH_T°, ΔS is the variation of the Gibbs energy, enthalpy and entropy of the reaction; T is temperature.

In physical chemistry these assumed that if $\Delta G_T^\circ < 0$, the reaction in the given conditions (T, P) takes place in the direct direction (i.e., in the direction of formation of reaction products). The value ΔG_T° for the reactions (1)–(3) is considerably smaller than zero and, therefore, the reaction takes place in the direct direction with the formation of a reduction products.

The TiO oxide is characterised by the basic properties, eight is capable of entering into reaction with alumina, forming the $TiO \cdot Al_2O_3$ which reduces the activity of Ti ON complicates the reduction of titanium. To reduce the rate of the process of bonding of the titanium oxide with the alumina, freshly roasted limestone is added to the charge. Calcium oxides replaces TiO, forming $CaO \cdot Al_2O_3$.

The increase of the dispersion of the charge increases the size of the reaction surface, i.e., excess energy is associated with the dependence of the thermodynamics of the process on the size of the particles of the participants of the reaction [7]. This dependence is evident only at a relatively high dispersion of the particles (when the number of the elementary particles, forming the interface, ceases to be a relatively small in comparison with the total number of the particles distributed in the volume).

Let us assume that the solid substance A consists of the crystals of the regular cubic form with the length of the face L and the unit volume includes n elementary particles. Consequently, the number of the particles in a separately considered crystal will be nL^3.

A certain part of these particles forms the surface of the cube. At a relatively large size of the crystal this part becomes insignificant and the isobaric potential of the substance A is determined by the state of the particles, situated inside the crystal, the so-called volume particles. The chemical potential of the single volume particle is denoted by μ_{vol}.

The excess surface energy of the surface particles can be expressed by the surface tension δ. Consequently, the following equation can be written for the isobaric potential, calculated for the single crystal of the substance

$$\Delta G^{кр} = nL^3\mu_{об} + 6L^2\delta.$$

The mean potential of the single particle is as follows:

$$\mu = \frac{\Delta G^{kp}}{nL} = \mu_{ob} + \frac{6\delta}{nL}$$

Consequently, by conversion to 1 mole of the substance we obtain

$$G = M\mu_{ob} + N\frac{6\delta}{NL} = N\mu_{ob} + \frac{F}{L}\delta$$

where N is the number of elementary particles in 1 mole; F/L is the surface of the crystal per one mole, or

$$G = G_{vol} + G_{sur} \quad (4)$$

Equation (4) shows that the increase of the dispersion of the participants of the reaction will support the increase of the reaction surface and, consequently, the increase of the free Gibbs energy.

Thus, the increase of the reaction surface increases the thermodynamics of the process which in turn should increase the thermal productivity of the charge and increase the yield of the reaction products.

On the other and, it is evident that the excessive refining of the charge materials for the aluminothermic process will, firstly,

increased the amount of ejection of the charge in the melt during melting (as a result of reducing gas permeability) and, secondly, fine refining of the oxides and the formation of fine fractions of the aluminium powder is associated with the additional losses of materials. In addition to this, a thin oxide film forms on the very fine fraction of the aluminium powder. The oxide film impairs the reduction properties of aluminium.

The aim of the present work is the determination of the effect of the dispersion of the charge materials on the aluminothermic process of titanium and also the determination of the optimum size of the fractions of the charge.

The degree of refining of the charge materials is one of the most important factors determining the parameters of the aluminothermic process. The practice of production of aluminothermic alloys outside the furnace shows that for the elements with low reduction capacity (titanium, zirconium, etc.) the size of the oxide particles should not exceed 2 mm. The fraction of the aluminium powder is selected in dependence on the size of the oxides in the process conditions [8]. To ensure the maximum rate of the reduction reactions, the size of the reduction agent should be selected to ensure that after mixing the charge materials in each elementary part of the charge, engine the reaction the components are in the stoichiometric ratio (taking into account the reduction coefficients of the oxides).

In examination of the effect of the degree of refining of aluminium on the melting rate of the charge is fraction depended on the surface of 1 g of the powder calculated from the conventional diameter of the grain [9]. Evidently, to obtain the stoichiometric ratio of the reagents at every moment of melting of the charge it is necessary to ensure that the ratio of the grains of the oxide in the reduction agent corresponded to the ratio of their gram equivalent volumes (Table 1).

As indicated by Table 1, in the majority of the oxides, important for the processes of aluminothermic melting outside the ladle, the gram-equivalent volume exceeds the volume

of the gram-equivalent of aluminium 1.5...1.9 times. If it is assumed that the grains of the components are spherical, the diameter of the aluminium particles D_{Al} should be in the range $0.8...0.9\,d_{ox}$ (the diameter of the grain of the reduced oxide). This ratio approaches unity if it is taken into account that the degree of reduction of the oxides in the industrial aluminothermic processes reaches 70…90% (in aluminothermic melting off a titanium 70…80% TiO_2 is reduced to titanium, 90% of silica to silicon). Thus, at the given size of the oxide particles the ratio of the charge materials in the microvolumes approaches the stoichiometric ratio if the size of the particles of the aluminium powder and the oxides are relatively identical.

To ensure the maximum yield of the metal, the fraction of the particles of the reduction agent should be similar to that of the reduced oxide, and the yield of the metal increases with the reduction of the particle size of the charge components. However, the reduced oxide should not be refined to the size smaller than 0.1 mm.

Taking into account the accepted fraction of the particles of the oxide part of the charge, the size of the reduction agent is selected equal to the size of the oxide particles only if this ensures the required conditions for the normal melting rate of the charge. At a reduced rate of the process, the size of the particles of the reduction agent should be slightly reduced in comparison with the oxide. If the degree of refining of the oxide is very high, eight is also efficient to ensure the maintenance of the equality of the size of the oxide in the reduction agent because in this case the rate of the process may be higher than the rate required for the steady thermal mode of the process.

In addition to this factors, in selecting the degree of refining of the charge materials it should be remembered that the fraction of the grain of the reduction agent determines the rate of deposition of the reduced metal. The application of the fine fractions of the aluminium powder may be the reason for high losses in the form of beads, remaining in the slag [9].

D.A. Kazarin, N.P. Volkotrub and M.I. Prilutskii

Table 1. Ratio of the gram-equivalent volumes of the reduced oxides and aluminium

Reduced oxide	Volume of gram equivalent oxide V_{ox}	V_{ox}/V_{Al}	D_{Al}/d_{ox}	Reduced oxide	Volume of gram equivalent oxide V_{ox}	V_{ox}/V_{Al}	D_{Al}/d_{ox}
Ba_2O_3	6.3	1.91	0.81	TiO_2	5.2	1.57	0.86
Ga_2O_3	5.3	1.47	0.88	V_2O_5	5.4	1.63	0.85
Fe_2O_3	5.1	1.55	0.86	Nb_2O_5	5.7	1.73	0.83
Mn_2O_3	5.9	1.78	0.83	Ta_2O_5	5.1	1.53	0.86
Cr_2O_3	4.8	1.47	0.88	WO_3	5.4	1.63	0.85
Ge_2O_3	5.6	1.70	0.83	MoO_3	5.4	1.63	0.85
Si_2O_3	6.5	1.97	0.80	NiO	5.0	1.52	0.87
Zr_2O_3	5.6	1.70	0.83	CuO	6.2	1.68	0.84

Table 2. Chemical composition of the charge materials, wt.%

Material	TiO_2	FeO	Fe_2O_3	SiO_2	MgO	CaO	Al_2O_3	Cr_2O_3	MnO
Ilmenite concentrate	63.00	8.1	20.0	1.78	0.13	0.13	2.02	2.92	0.95
Iron ore	0.031	–	89.4	9.10	0.52	0.24	0.39	0.021	–
Freshly roasted limestone	–	–	–	5.00	–	90.00	2.00	–	–

The initial charge for the experimental melts was in the form of the materials of the chemical composition shown in Table 2.

The reduction agent was aluminium grit (93% of aluminium). The charge was calculated for 100 kg of titanium concentrate. Melting was carried out in a crucible 400 mm high, diameter 200 mm, lined with a mixture of magnesite powder (95%), water glass (0.7%) and refractory clay (4.3%). The thickness of the lining was 15…20 mm.

The normal course of the aluminothermic process was obtained at a specific heat of 2550…2600 kJ/kilogram of charge. The missing part of heat was compensated by heating the crucible and the charge. This was carried out taking into account the fact that every 100°C of heating increases the specific heat of the process by 125.6 kJ/kg.

1/3 of the charge was loaded into the crucible and ignited with a torch. After the start of the process, the charge was placed on the surface in such a manner that the surface of the melt was covered with the charge layer.

The powder of the ilmenite concentrate (Fig. 1) consisted of spherical grains with different particle size distributions (Fig. 2).

Taking into account the size of the fraction of the ilmenite powder, we selected the size of the particles of the reduction agent (by calculations $D_{Al} \sim d_{ox}$). The initial powder of the titanium concentrate was crushed to produce the fraction with the size of 50…60 μm. The mean chemical composition of fellow titanium with the particle size of the concentrate and the reduction agent of 50…60 μm was as follows, wt.%: 27.3 Ti, 51.8 Fe; 11.2 Al; 7.1 Si; 0.12 Ca; 0.96 Cr; 1.03 Mn; 0.11 Ni; 0.25 Cu; 0.13 Zr.

The melts were accompanied by the injection of the molten metal and the structure of the produce for the titanium was porous (Fig. 3).

In producing the melts with the ilmenite particle size and the reduction agent size of 200...240 μm, the process of aluminothermic reduction is steady, without injection of the melt.

The mean chemical composition of fellow titanium (dispersion 200…240 μm) was as follows, wt.%: 43.5 Ti; 34.9 Fe; 14.1 Al; 3.81 Si; 0.34 Ca; 1.04 Cr; 0.96 Mn; 0.101 Nb; 0.102 Cu; 0.3 Sn.

The phase composition of the specimens of ferrotitanium was represented mainly by
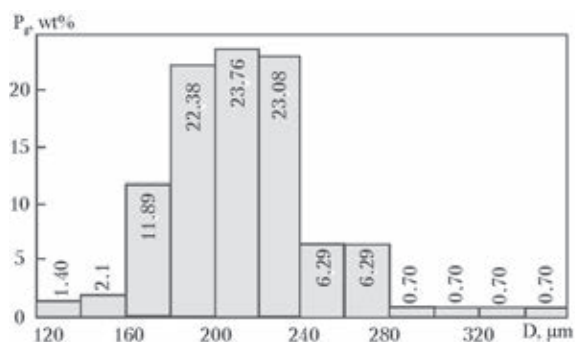
Fig. 1. Initial ilmenite powder.

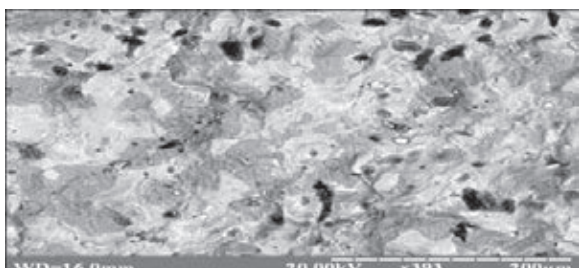**Fig. 2.** Size distribution of the particles *d* in the initial powder of ilmenite P_{il}.

Fig. 3. Microstructure of the ferrotitanium sample, produced by the aluminothermic method (dispersion of the charge 50…16 µm).

the titanites TiFe ($TiFe_2$), oxide inclusions $FeO \cdot TiO_2$ and TiO_2 and iron oxides. Dark spots are pores, formed as a result of reduction of the permeability of the charge (Fig. 3). X-ray spectrum microanalysis was carried out in a PEM 106i scanning electron microscope (SELMI, Ukraine). Phase composition was determined in the x-ray diffractometer with the horizontal position of the investigated specimen RIGAKU (Japan).

According to the analysis of the literature data it may be concluded that the dependence of the processes of aluminothermic reduction of the dispersion of the materials of the charge in melting ferrotitanium is non-linear. The experimental results show that the excessive increase of the dispersion of the charge (50…16 µm and smaller) results in a large reduction of the gas permeability of the charge and, correspondingly, the 'boiling' of the bulk charge. This is accompanied by the pyroeffect with ejection of the melt. The ferrotitanium casting contains pores.

As a result of the presence of the fine aluminium powder of the oxide film on the surface the yield of the reaction products decreases, i.e., the fraction of a reduction of titanium from the ilmenite concentrate decreases.

The high density of the ingot and the maximum yield of the reaction products in the reduction were obtained at the ratio $D_{Al}/d_{ox} \sim 1$. The dimensions of the other components of the charge should not exceed 2 mm.

The data obtained as a result of the laboratory studies confirmed the previously made the commendations for the selection of the dispersion of the charge in the aluminothermic production of ferrotitanium from the ilmenite concentrate and indicate that it is necessary in every specific case to carefully the grain size composition of the charge materials to obtain the best results.

References

1. Gasik M.I. and Lyakishev N.P., Physical chemistry and technology of ferroalloys, a handbook for higher technical schools, Dnepropetrovsk, 2005.
2. Kazarin D.A., et al., Naukovi visti Natsional. Tekh. Univ. Ukraini, KPI, 2013, No. 2, 90–93.
3. Gasik M.I., et al., Current problems and prospects of electrometallurgical production: Proc. Int. Conference, Dnepropetrovsk, 1999, 334–336.
4. Murty C., et al., Proc. INVACON XI, Delhi, 2007, 823–836.
5. Lyakishev N.P., et al., Aluminothermy, Metallurgiya, Moscow, 1978.
6. Murach N.N. and Mushenko V.T., Aluminothermy of titanium, GOSINTI, Moscow, 1958.
7. Pliner Yu.D. and Dubrovich A.S., Zh. Prikl. Khimii, 1964.
8. Bogoloyubov V.A., Physical-chemical fundamentals of metallurgical processes, Metallurgiya, Moscow, might in 1964.
9. Konovalov R.P., et al., Stal', 1984, No. 4, 29-30.